Understanding the metabolic processes and degradation of therapeutic proteins after subcutaneous administration

By

Ninad Varkhede
B. Pharmacy, MGV's Pharmacy College, 2010
M.S., Pharmaceutical Analysis, National Institute of Pharmaceutical Education & Research, 2012
M.S., Pharmaceutical Chemistry, The University of Kansas, 2016

Submitted to the graduate degree program in Pharmaceutical Chemistry and the Graduate Faculty of the University of Kansas in partial fulfillment of the requirements for the degree of Doctor of Philosophy.

_____

Chair: Dr. M. Laird Forrest

_____

Dr. Jeffrey Krise

_____

Dr. Christian Schöneich

_____

Dr. Michael Wang

_____

Dr. Prajnaparamita Dhar

Date Defended: August 23, 2018

The dissertation committee for Ninad Varkhede certifies that this is the approved version of the following dissertation:

Understanding the metabolic processes and degradation of therapeutic proteins after subcutaneous administration

Chair: Dr. M. Laird Forrest

Date Approved: August 23, 2018

Abstract

Subcutaneous (SC) route is important for administration of various therapeutic proteins (TPs) like monoclonal antibodies (mAbs), human growth hormone (hGH), insulin, and recombinant subunit vaccines. The SC route has advantages like shorter clinical visits for patients, the possibility of self-administration, and its less invasive nature compared to the intravenous (IV) route. However, SC route has a challenge of incomplete bioavailability for various TPs, especially mAbs (52-80%). After SC administration, the mAbs travel through the lymphatic vessels and lymph nodes (LNs) before reaching the systemic circulation. Proteolysis at the SC injection site and within the lymphatic system may be partially responsible for the reduced bioavailability of mAbs. Chapter 2 of this dissertation describes a top-down mAb physiologically based pharmacokinetic (PBPK) model which was used to estimate the lymphatic trunk-LN clearance using the human SC pharmacokinetic (PK) data from published clinical trials. Iron oxide nanoparticles (IONPs) may originate from equipment used in the manufacturing of TPs or from needles during the SC injection. The IONPs may alter the secondary structure and the degree of oxidation of TPs. Therefore, Chapter 3 of this dissertation looks at the effect of IONPs on the TP stability. In Chapter 4, midazolam (MDZ) metabolism and PK were reported in the healthy and inflammatory disease condition in mice. Finally, a bottom-up minimal PBPK model was used to predict MDZ PK in the disease state.

Acknowledgments

I bestow sincere gratitude towards my advisor Dr. Laird Forrest for encouragement and suggestions during the dissertation work. I am thankful for the opportunity to join his laboratory. I really appreciate his time and help during my graduate education. Laird's guidance was important for me to succeed in the research. I learnt several aspects of science during this tenure.

Drs. Christian Schöneich, Jeffrey Krise, Michael Wang, Prajnaparamita Dhar were members of the dissertation committee. It was my pleasure to interact with them during this work at several poster sessions and seminars. Thanks for their words of motivation and criticism. Thanks to Dr. Schöneich for his enthusiasm about my projects, suggestions, and critically reading one of the manuscripts. We had several discussions which were helpful. I would like to thank Dr. Middaugh for insightful guidance related to the dissertation project. I am thankful to Dr. Michael Hageman for suggestions and time to discuss one of the projects during the Fall Retreat Poster session and the seminar at the School of Pharmacy.

The time at the University of Kansas was enjoyable due to delightful company of Forrest group members. I would like to thank Ryan Moulder, Abby Petrulis, Peter Kleindl, Jordan Hunt, Ruolin Lu, Jay Zha, Sanjeewa Senadheera, Ti Zhang, Chad Groer, Shuang Cai, Allie Brachtenbach, and Jaden Jun, for their kindness, generous help, and questions during several group meetings and hall-way discussions.

I had many discussions with Bjoern Peters, Ruepsh Bommana, and Olivier Mozziconacci while working on the projects involving mass spectrometry analysis. I would like to thank them and everyone in the Schöneich group, especially Indira Prajapati, Huan Kang, Natalia Subelzu, and Hasitha Rathnayaka for their help. In addition, I would like to thank all the fellow graduate students from the department of Pharmaceutical Chemistry for their help and collaboration.

Sanjeev Agarwal, Yangjie Wei, and Nick Larson helped me with biophysical characterization of the protein. Thanks to Derek White, Ishan Shah, Khalid Al-Kinani, and Dr. Tom Tolbert for hall-way discussions, and mass spectrometry analysis. I would like to thank Dr. Philip Gao (Protein Production Group, The University of Kansas) for production of rat growth hormone protein.

I would like to thank Nita Patel and Dan Mudra for an internship opportunity at Eli Lilly (Indianapolis, IN) and for guidance. The internship project was recently published and is a part (Chapter 4) of this dissertation. I would like to thank William Chang (cytokine measurement), Kenneth Ruterbories (LC-MS analysis), and George Searfoss (mRNA measurement) for their help. Thanks to Michael Mohutsky for letting me use the facilities in his lab and for help with the *in vitro* metabolism work, Tom Kern for conducting *in vivo* pharmacokinetic studies, Bridget Morse and Stephen Hall for discussions related to the PBPK model.

Special thanks to Nancy Helm, Andre Faucher, Nicole Brooks, Anne Heptig, and Karen Hall. Thanks to several graduate students from the Pharm Chem. and other graduate programs at KU (Nishant Sawant, Vishal Toprani, Apurva More, Laura Dbrbohlav, Mei Feng, Iris Qiu, Melissa Pressnall, Jimmy Song, Nataila Subrlzu, Martin Hu, Matt Christopher, Khushboo Kapadia, and Kakasaheb Nandiwale) for many conversations which helped me to keep engaged in the department and focused on the studies.

Finally, I would like to thank my Mom and Dad for their love and encouragement to pursue scientific inquiry in every aspect of the life and for their continuing teachings and words of wisdom, which helped me to face difficult situations. I would also like to thank my brother Saurabh for constant motivation. Thanks to my wife and friend, Priyanka, for her support, encouragement, patience and pleasant company during this work. She also helped me to learn ‘R’ which I used for statistical analysis and plotting several graphs in this dissertation.

I would like to acknowledge National Institutes of Health (R01CA173292), Higuchi Fellowship (the Department of Pharmaceutical Chemistry) and the J.R. and Inez Jay funds by the Higuchi Biosciences Center at The University of Kansas for financial support.

This dissertation is dedicated to thousands of known and unknown scientists, engineers, doctors, architects, philosophers, and artists who lived since the dawn of humanity and whose work became the foundation for shaping today's world around us.

Table of Contents

List of Figures

List of Tables

Chapter 1 : Introduction

Monoclonal antibodies (mAbs), human growth hormone (hGH), insulin, recombinant subunit vaccines and various other proteins are important therapeutic proteins (TPs) (1). The TPs are mainly administered via intramuscular (IM), subcutaneous (SC) and intradermal (ID) routes due to convenience compared to the intravenous (IV) route (2). However, incomplete bioavailability is a major disadvantage for the TPs (3). Proteolysis at the SC injection site and in the lymphatic system is a major elimination pathway for the TPs and is responsible for reduction in their bioavailability (3-6). The needle penetration in the skin and SC tissue can promote secretion of proteolytic enzymes by various cells into the extracellular matrix (interstitial space). The SC injection site consists of cells like adipocytes, fibroblasts, T cells, lymphocytes, mast cells, dendritic cells (DCs) and macrophages, which contribute towards proteolysis of the TPs (Figure 1.1). The SC tissue has a low level of basal proteolytic activity; however, the penetration of an injection needle and the subsequent hydrostatic pressure due to the injection volume can alter the SC tissue leading to secretion of serine proteases, threonine proteases, and metalloproteases by the tissue matrix, DCs, and other SC tissue cells (7, 8). Finally, intracellular processes like proteasomal catabolism after ubiquitin binding and lysosomal degradation may also lead to reduced bioavailability of the TPs (7, 9, 10). In addition, immune reactions (e.g. generation of antibodies against the administered TP, allergy, anaphylactic reaction, accumulation of immune cells around the injection site) can enhance the proteolytic activity in SC tissue. These immune reactions are caused by the presence of non-self antigens, partially degraded (e.g. oxidized or deamidated) TP, manufacturing impurities, and aggregates of the TP.

Along with the SC injection site, the lymphatic system can also play a vital role in proteolysis of the TPs. Proteins with molecular weight greater than 16-20 kDa are usually absorbed at least partially via the lymphatic capillaries upon SC administration (3, 11, 12), from which they are trafficked through the lymphatic vasculature and lymph nodes before entering the systemic circulation at the junction of the left subclavian vein and internal jugular vein or at the beginning of left brachiocephalic vein. The lymph nodes (LNs) are predominant sites of antigen presentation, because the nodal sinuses are large populations of antigen presenting cells (APCs), naïve and mature B and T cells. The structure of LNs is responsible for a molecular sieving of passing materials, resulting in extensive interaction of proteins with the APCs (3, 13-15). Therefore, the endocytic uptake and lysosomal degradation may contribute towards the loss of TPs in the LNs. In addition, the immune cells in the lymphatic system may secrete protease enzymes (16) leading to increased proteolysis of the TPs. Hence, the lymphatic system plays a major role in proteolysis of the TPs and reduction in their bioavailability (3, 13-15).

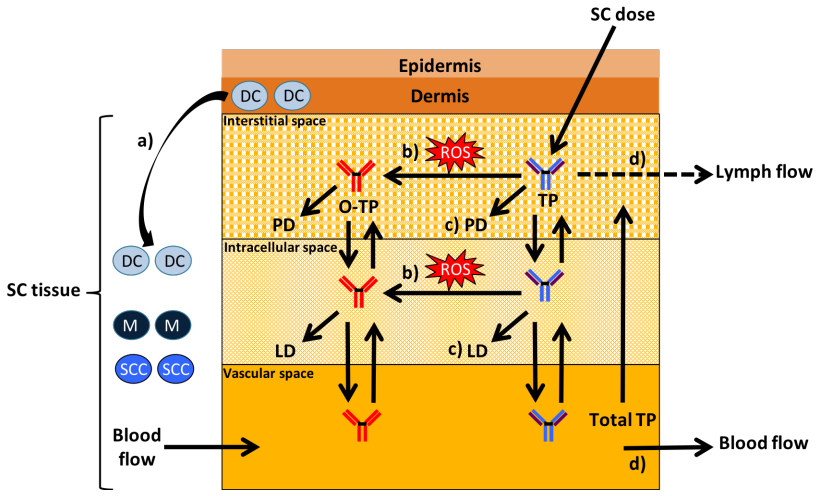

Figure 1.1: Physiological processes at the SC injection site
a) Migration of DCs from the dermis to SC tissue due to penetration of the SC injection needle. b) Potential oxidation of the TP by the ROS. c) Proteolytic and lysosomal degradation of the TP in the SC interstitial and intracellular compartments. d) Uptake of the TP by the lymphatic capillaries (lymph flow) and blood vessels (blood flow). (TP: Therapeutic protein, O-TP: Oxidized TP, DC: Dendritic cells, M: Macrophages, ROS: Reactive oxygen species, PD: Proteolytic degradation, LD: Lysosomal degradation, SCC: Subcutaneous cells).

The oxidation of TPs is another metabolic process responsible for their degradation in the skin, SC tissue and lymphatic system. The oxidation may lead to undesirable effects like altered biological activity, increased immunogenicity, modified secondary and tertiary structure of the TP, increased aggregation potential, altered pharmacokinetics (PK), and decreased neonatal Fc receptor (FcRn) binding affinity for the mAbs (17, 18). The amino acids like methionine, phenylalanine, tryptophan, tyrosine, histidine, cysteine are prone to oxidation by hydrogen peroxide and superoxide radicals produced by respiratory bursts of immune cells, especially the monocytes and neutrophils (19). Furthermore, cellular damage, e.g. physical rupture by the injection needle, osmotic and hydrostatic stress, can generate signals of wounding which include secretion of proinflammatory cytokines (IL-1β, TNF-α and IL-6). In addition, DCs and macrophages can initiate an innate immune response. The DCs and macrophages continuously ingest proteins within the tissue and display protein fragments as potential antigens. Localized irritation and immune reactions are frequently observed in the SC tissue after injection of the TPs. Mast cell population is approximately 7000/cm^3 and can be responsible for immune response against allergens possibly present in the TP formulation (7). A specialized subpopulation of DCs termed as the langerhans cells (LCs) reside in the epidemis. The LCs constitute around 1% of the total epidermal cell population; however, they occupy approximately 20-25% of the surface area. Various cells in the SC tissue are also involved in the adaptive immune response and antigen presentation to naïve T cells in the LNs (20-22). The innate and adaptive immune response against the TPs is usually disadvantageous, as it may result in increased proteolysis and generation of reactive oxygen species (ROS) leading to oxidation of the TPs (Figure 1.1). However, in the case of proteins derived from pathogenic agents, this process is used successfully for recombinant

protein and sub-unit based vaccines to enhance the immune response and pharmacological action (20).

1.1 Proteolytic enzymes in the skin, SC tissue and lymphatic system

1.1.1 Introduction and classification of proteolytic enzymes

The proteolytic enzymes (peptidases) are broadly categorized as endo-peptidases and exo-peptidases based on whether they preferentially cleave the peptide backbone distant from the termini (Figure 1.2) or at penultimate or terminal peptides, respectively. In addition, the proteolytic enzymes can be classified based on the amino acid present at the catalytic site of the enzyme. The serine proteases, cysteine proteases, aspartic proteases, metallo-proteases are major categories having different catalytic sites (Figure 1.2). Detailed classification of proteolytic enzymes was reported elsewhere (23-26).

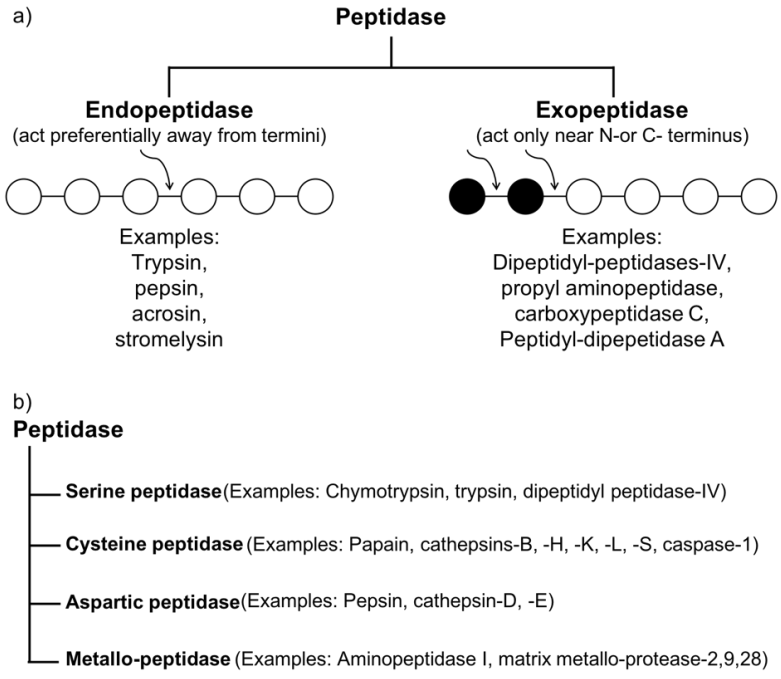

Figure 1.2: Classification of the proteolytic enzymes or peptidases. a) Classification based on the site of their action on the target protein b) Classification based on the catalytic site

1.1.2 Proteolytic enzymes in the skin and lymphatic system

More than 30 proteolytic enzymes are present in the skin and SC tissue. Skin has 2 major layers, the epidermis and dermis. In the epidermis, cysteine and serine proteases form the major fraction of the total proteolytic enzymes, followed by aspartic and metalloproteases (Figure 1.3) (27). The rat epidermis has approximately 10 times more proteolytic activity compared to the dermis and proteolytic enzymes are found in the epidermal cells. However, in the case of dermis, proteolytic enzymes were present in the infiltrating immune cells, sebaceous glands, and follicular cells (28).

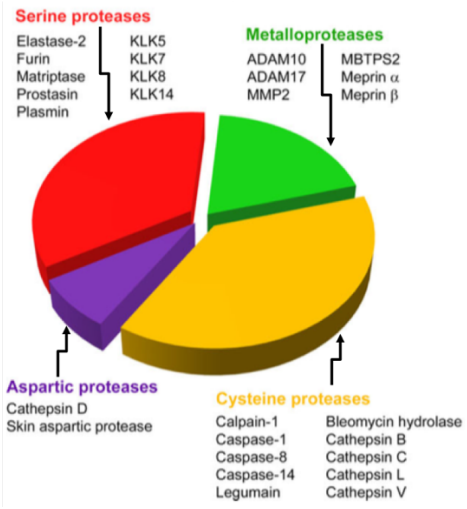

Figure 1.3: Proteolytic enzymes present in the epidermal layer of human skin
KLK: Kallikrein-related peptidases, ADAM: A disintegrin and metalloprotease, MBTPS2: Membrane bound transcription factor peptidase site 2 (reproduced with permission from Veer et al (27)

The skin is densely packed with various immune cells and is an immune organ itself (21). The cutaneous surface of normal adult humans has around 20 billion T cells, which can secrete proteolytic enzymes leading to degradation of the administered TPs (27, 29). The proteolytic enzymes such as tryptase, cathepsin G, neutrophil elastase originate from the T cells and other infiltrating immune cells (27). Caspase-14 is a major cysteine protease, expressed in the human epidermal keratinocytes. Serine protease HtrA1 is found ubiquitously in many organs; however,

increased amounts were found in the mature layers of the epidermis (30). Cathepsin D and E are found in various other organs like LNs, spleen, kidney, lung, and liver (31, 32). Cathepsin G has been identified in the rat spleen and LNs (33). Dipeptidyl peptidase IV (DPP-IV) was expressed more in the cultured human dermal lymphatic cells compared to the blood vascular endothelial cells (34).

1.1.3 Effect of species and age on proteolytic enzymes

Preclinical safety testing of the TPs is typically conducted in rodents, one or more large animals like the dog, and possibly non-human primates although these preclinical models have been found to poorly represent human bioavailability and PK of numerous TPs (35). Kageyama et al. reported that the expression of cathepsin D and E in spleen and LNs is variable across the species like rat, monkey and humans. The monkey spleen tissue had around 2 times higher levels of cathepsin D compared to the rats. In the case of monkey LNs, cathepsin D was 4-fold higher than the rat LNs. In contrast, the rat spleen had around 40-fold higher expression of cathepsin E compared to the monkey spleen. The rat LNs had around 11-fold higher cathepsin E expression than the monkey LNs (32). These differences in protease expression may contribute towards variations in overall clearance of the TPs leading to different values of bioavailability across the species. Further, age dependent increase in elastase like endopeptidase activity was seen in the mouse skin. This increase in peptidase activity is important during 6 to 15 months of the lifetime and can be attributed to the metallo-endopeptidases (36).

1.1.4 Altered expression and role of proteolytic enzymes in the pathological conditions

Table 1.1: Proteolytic enzymes altered due to various pathological conditions
(Adapted/modified from Veer at al (27) with permission)

Pathological condition	**Proteolytic enzyme**	**mRNA or protein content or activity of the peptidase(s) compared to the healthy condition**	**Organ or tissue or cell population**	**Reference**
Papillon-Lefèvre syndrome	Cathepsin C	Approximately 85% reduction in the enzyme activity, possibly due to genetic modifications	Leucocytes	Romero-Quintana et al. (37)
Morbus Hodgkin's lymphoma	Cathepsin B, H, L, S (cysteine proteases)	Increased expression	Lymph nodes	Kirschke et al. (38)
Ichthyosis hypotrichosis syndrome	Matriptase (a serine protease)	Mutation leading to loss of function	Skin	Basel-Vanagaite et al. (39)
Inflammatory skin and bowel disease	Metalloprotease 17	Mutation leading to loss of function	Skin and bowel	Blaydon et al. (40)
Skin injury	Matrix metalloprotease 28 (epilysin)	Induction after skin injury	Skin (epidermis)	Saarialho-Kere et al. (41)
Recessive dystrophic epidermolysis bullosa	Matrixmetallprotease (MMP) 1	Elevated expression	Skin (epidermis)	Titeux et al. (42)
Lymphadenopathy	*DPP-IV (a serine protease)	Increased expression in enlarged lymph nodes	Lymph nodes (aberrant T cells without CD4 or CD8)	Kubota et al. (43)
Psoriasis and rheumatoid arthritis	Arg-, Ala-, and Leu-N-aminopeptidases and DPP-IV	Increased expression	Fibroblast	Raynaud et al. (44)
Psoriasis and seborrheic dermatitis patients	Caspase-14	Inactive procaspase-14 along with the active caspase-14	Immature pakeratotic skin	Fischer et al. (45)
Allergic contact dermatitis and bullous pemphigoid	[#]Tryptase (a serine protease)	Higher levels in the skin blister fluid	Mast cells in the skin	Brockow et al. (46)

**Increased DPP-IV levels in serum were correlated with enlargement of the LNs. MRL-lpr mice were used as a disease model for lymphadenopathy*
[#]Higher tryptase levels compared to the blister fluids obtained from insect bite reactions, erysipelas, burns, toxic epidermal necrolysis
(DPP-IV: Dipeptidyl peptidase-IV, LNs: Lymph nodes)

Expression of proteolytic enzymes in the skin and SC tissue is altered during various diseases (Table 1.1) (27, 47). Papillon-Lefèvre syndrome (PLS) is associated with periodontitis and thickening of epidermis (27). Lysosomal cysteine proteases such as cathepsins-B, -H, -L and -S are overexpressed in the tumor cells of Morbus Hodgkin's lymphoma. Expression of the cysteine proteases is increased with increasing malignancy of the lymphoma (38). Ichthyosis hypotrichosis syndrome of skin leads to loss of function of matriptase (a serine protease) (39). In the case of inflammatory skin and bowel disease, metalloprotease 17 was not expressed (40). In another example, epilysin or matrix metalloprotease-28, which is expressed in the skin keratinocytes, was induced after injury to the epidermis, because it is involved in the wound healing process. It degrades the adhesive proteins like cadherins or collagen to release new cells and thus inducing the repair mechanism (41). Epilysin expression was also increased in the cartilage and synovium of the patients with osteoarthritis (48). Furthermore, expression of matrixmetallprotease 1 was increased in the recessive dystrophic epidermolysis bullosa (42).

The LNs were abnormally enlarged in the mouse model of lymphadenopathy. In addition, the serum DPP-IV levels increased in the enlarged LNs, and the levels were directly proportional to the weight of the LNs (43). Arg-, Ala-, and Leu-N-aminopeptidases and DPP-IV were found on the surface of human dermal fibroblasts. These enzymes were elevated in the human fibroblasts obtained from the psoriasis and rheumatoid arthritis patients. Leu-N-aminopeptidases and Arg-N-aminopeptidases were elevated up to 1.5- to 6.6-fold, respectively compared to the healthy fibroblasts. While, DPP-IV was elevated by 4.5-fold compared to the healthy fibroblasts (44).

Caspase-14 is a predominant caspase in the human stratum corneum. The immature pakeratotic skin from psoriasis and seborrheic dermatitis patients contained inactive procaspase-14 along with the active caspase-14 form. In contrast, the healthy skin contained only the active

form, i.e. caspase-14. This study shows that proteolytic activity and expression can be significantly different for the healthy and diseased skin (45). Tryptase is a serine protease abundantly present in the mast cells of the skin. The skin blister fluid from the allergic contact dermatitis and bullous pemphigoid patients contained higher levels of tryptase compared to the other skin conditions like insect bite reactions, erysipelas, burns, and toxic epidermal necrolysis. The higher level of tryptase denotes that the mast cell degranulation was the pathophysiological mechanism of allergic contact dermatitis and bullous pemphigoid (46, 49). In addition, the UVA exposure to the mouse skin showed greater increase (+90 to 122%) in peptidase activity compared to the UVB exposure (+72%). The serine endopeptidases and metalloprotease enzymes were affected by the UVA radiation (36). In another study, it was found that UVB exposure increased secretion of matrix metalloprotease-2 by human dermal fibroblasts (50).

1.1.5 Targeting disease using the protease enzymes

Protease enzymes present in the skin, SC and lymphatic tissues may be important for targeting specific cell population or tumors. For example, the protease enzyme tryptase is abundant only in the mast cells and not in the other white blood cells like peripheral blood leukocytes and basophils, which have either none or very small amount of tryptase (49, 51). The solid tumors of epithelial origin are known to express various peptidases like urokinase, matriptase, and legumain. This physiological phenomenon was used to engineer a pro-mAb, which was masked with a peptide attached to the light chain of the mAb via a linker peptide. The linker peptide was a substrate of the tumor specific protease. The masked pro-mAb was inactive and the masking peptide was cleaved by the specific protease expressed abundantly in the cancerous cells. This approach of using pro-mAb was proposed to reduce toxicity and improve therapeutic index of

EGFR targeting mAbs used to treat head and neck squamous cell cancer, non-small cell lung cancer, and breast cancer (52).

Key points and unknowns

Protease enzymes play a crucial role in clearance of the TPs and they are altered in various animal species, with different age and disease conditions. The increased or decreased protease activity in the skin, SC tissue and lymphatic system may lead to differences in PK of the TPs. However, impact of the altered expression of protease enzymes on PK of TPs is not clearly known. It is important to identify the proteolytic enzymes responsible for the reduced bioavailability of TPs because the reduced SC bioavailability of TPs may be mitigated by co-administration of peptidase inhibitors. For example, an ointment of peptidase inhibitors (nafamostat or gabexate) was applied before the SC administration. The peptidase inhibitors penetrated the injection site and decreased the TP degradation in the SC tissue (53). This strategy was also used for oral and pulmonary delivery of proteins and peptides (54, 55).

1.2. *In vitro* methods to study proteolysis of TPs

Various *in vitro* systems (whole blood, serum, plasma, liver and kidney homogenates), have been used to study proteolysis of the TPs (56). The tissue homogenates and recombinant enzymes are most commonly used tool to evaluate stability of the TPs. The metabolism of small molecule drugs (SMDs) in the liver and other organs has been extensively studied using *in vitro* systems to obtain quantitative data (e.g. Chapter 4) (57). Similar information about metabolic processes of the TPs in the SC injection site and lymphatic system is necessary and remains to be generated (2, 58-61). In this section, examples and applications of the *in vitro* methods used to study degradation of TPs are discussed.

1.2.1 Bioavailability of TPs after SC administration

The recombinant peptidase enzymes (e.g. DPP-IV and neutral endopeptidase), tissue homogenates and tissue fractions like human liver S9 fraction were used to study proteolysis of the TPs (62). Higher rate of the *in vitro* proteolysis generally indicates that the TP has lower bioavailability. For example, leuprolide acetate had low bioavailability of around 32% after SC administration. The *in vitro* incubation of leuprolide acetate with a rat skin homogenate lead to around 90% degradation of the peptide within 120 min. This may indicate that the skin is mainly responsible for the proteolysis (63).

Erythropoietin is a TP with about 20-30% SC bioavailability in humans and 30-38% in rats (13, 64). Wang et al. used rat SC tissue homogenate and LN cell suspension to study degradation of erythropoietin. The incubation of erythropoietin with the SC tissue homogenate and LN cell suspension resulted in appearance of smaller fragments of the TP and decreased intensity of the parent erythropoietin after 24 h as shown by the SDS-PAGE analysis. This indicated that the reduced bioavailability of erythropoietin was probably due to proteolysis in the SC tissue and LNs (13). In another study, after SC injection to a lymph duct cannulated sheep, 61% of the hGH was collected in the peripheral lymph, while around 8% was collected in the central lymph. This shows that the hGH degraded significantly in the lymphatic system after SC administration to sheep. Total recovery of hGH by the lymphatic system was around 93%, indicating minimal contribution of SC injection site in the proteolysis (65).

The *in vitro* tools composed of various cellular fractions were used to study proteolysis of the TPs. Microsomal, nuclear and mitochondrial fractions were prepared using rat LNs and incubated with the peptidase substrates- benzoyl-L-arginamide (BAA) and glycyl-L-tyrosinamide acetate (GTAA). The mitochondrial fraction showed highest proteolytic activity (66). Detailed

information about mitochondrial proteases and their classification based on function and location can be found elsewhere (67).

Kinnunen et al. reported a novel *in vitro* platform simulating the SC injection site. The platform consists of a dialysis based SC injection chamber, which can be filled with multiple non-cellular SC tissue components like hyaluronic acid. The physiological buffers were used to simulate the SC tissue pH conditions. Another chamber with a physiological buffer served as an infinite sink representing rest of the body. However, this system did not utilize proteolytic enzymes or cellular components responsible for proteolysis of the TPs. The platform may be used to predict behavior of the TP formulations, and to measure rate of release of the TPs from the SC injection site (68).

1.2.2 Use of in vitro methods in TP engineering

Wroblewski et al. used *in vitro* methodology to demonstrate that, decoy receptor 3 was proteolytically cleaved between amino acids 218 and 219. This information was used to improve the TP stability, by replacing Arg-218 with a glutamine. The modification resulted in reduced proteolytic degradation and increased stability of the TP (69). In another report, DPP-IV and neutral endopeptidase were used to find degradation products of human glucagon like peptide-1 (GLP-1) and its modified analogue, liraglutide. Liraglutide degraded into a single metabolite in the presence of DPP-IV, while multiple peptides were formed after incubation with neutral peptidase. Rate of liraglutide degradation was slower compared to GLP-1, while, the cleavage site for liraglutide was similar to that of GLP-1. This study helped to understand comparative stability of various peptide analogues and to find cleavage sites for the peptides (62).

1.2.3 Proteolysis for release of small molecule drugs from ADCs

Proteolysis of the TPs usually results in reduced bioavailability after SC administration; however, proteolysis is occasionally important for TPs like antibody-drug conjugates (ADCs). ADCs are proteolyzed and the conjugated SMD is released. The human liver S9 fraction was used to monitor release of the SMD and proteolysis of the TP (70). Anti-cancer drug, monomethylauristatin E (MMAE) was attached to cAC10 mAb via novel valine-citrulline *p*-aminobenzylcarbamate (val-cit-PABC) linker. The linker was cleaved by the protease enzyme cathepsin B, to release MMAE (Figure 1.4). However, even without the cleavable linker, anti-cancer drugs can be released by the non-selective proteolysis and lysosomal degradation (70, 71). Ado-trastuzumab (Kadcyla) is an ADC approved by the FDA that uses noncleavable linker (72). In addition, an ADC conjugated with monomethylauristatin F (MMAF) using a noncleavable maleimidocaproyl linker was equally potent compared to an ADC linked with the cleavable val-cit-PABC linker (73). The *in vitro* assays can be useful to monitor release of SMDs from both the cleavable and non-cleavable linkers.

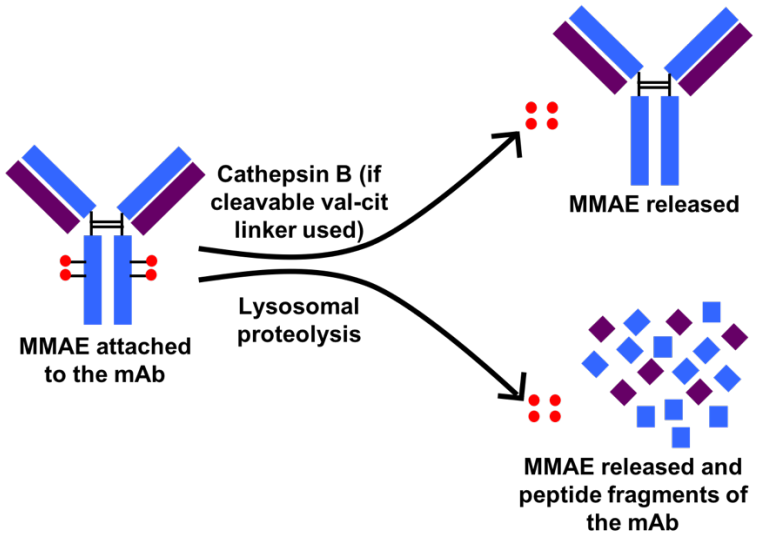

Figure 1.4: Release of MMAE from the ADC by cathepsin B or lysosomal proteolysis

Key points and unknowns

The *in vitro* methods are used effectively to study proteolysis of the TPs, but rare to date provide quantitative proteolysis information. Therefore, bioavailability cannot be mechanistically estimated using the available *in vitro* systems (61). The quantitative data can be used to define the rate of metabolism from the SC injection sites and the lymphatic system. In addition, the data may be used to develop a PBPK model for PK predictions.

1.3 Factors affecting PK of TPs after SC administration and PBPK modeling

1.3.1 Effect of molecular weight on lymphatic uptake of TPs

After SC administration the TP usually travels through the lymphatic vessels and LNs before it reaches the systemic circulation (74). The uptake of TPs via lymphatic capillaries after SC administration is dependent on its molecular weight. The TPs greater than 16 kDa molecular weight are generally absorbed via lymph vessels (15). Supersaxo et al. reported correlation of molecular weight and percent dose recovered in the lymph fluid of sheep after SC administration. A linear relationship was observed between percent dose recovered in the lymph and the molecular weight (Figure 1.5). rIFN alpha-2a (19 kDa) had percent lymphatic recovery of approximately 60% (11). In another study, hGH (22 kDa) had lymphatic recovery of around 62% in a sheep model (65). Both of these studies indicate that molecular weight is important factor for the lymphatic transport and to understand disposition of the TPs after SC administration.

1.3.2 Effect of animal species on PK of TPs

The PK of TPs may be variable in different animal species (75). A minipig animal model may be a suitable preclinical species for the human PK predictions, because minipig and humans have

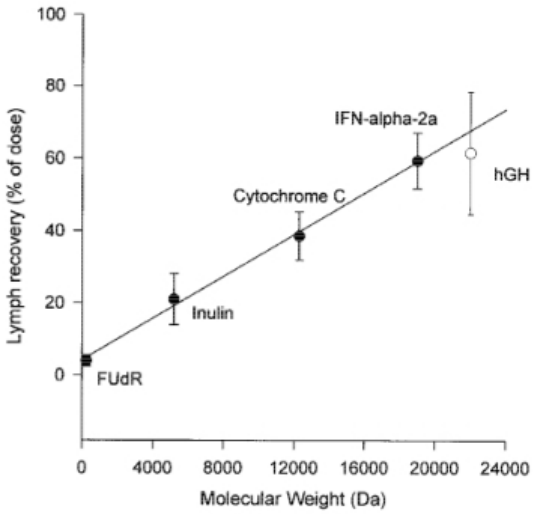

Figure 1.5: Effect of molecular weight on % lymphatic recovery of various proteins after SC administration to sheep.
These data were originally reported by Supersaxo et al. (11) and Charman et al. (65) The lymph was collected from the right popliteal lymph node of a sheep after SC administration of the protein on lower side of the right hind leg. (Reproduced with permission from a review article by Porter et al. (3))

similar skin structure and lymphatic plexus. Thicknesses of the epidermis and stratus corneum, and lipid contents of the stratum corneum are similar in humans and minipigs. In addition, the thickness of the SC tissue is also similar. However, the absorption rate of TPs from the SC injection site was 2 to 5-fold higher in minipigs compared to humans. In addition, the bioavailability of adalimumab was different in minipig and humans (Table 1.2) (2, 76). Hence, mechanistic understanding of proteolysis and absorption processes in the SC tissue of each species is important.

1.3.3 Effect of the injection site on PK of TPs

The SC injection site may be partially responsible for the proteolysis of TPs by secreting proteolytic enzymes in the extracellular matrix as well as by intracellular proteolysis. According to the published studies, hGH and insulin were degraded at the injection site (77, 78). Further, the bioavailability of hGH in humans was higher when injected in the abdomen compared to the thigh

(79). The bioavailability of insulin was different after SC injection at various injection sites (abdomen, thigh, and arms) (Table 1.2). The rate of absorption (indicated by T_{max}) was higher for abdominal injection (63 min) compared to the arm (76 min) and thigh (92 min) (80). In another study, bioavailability of mepolizumab was 64, 75, 71 and 81% after SC abdomen, SC arm, SC thigh and intramuscular (IM) administration, respectively (81). The bioavailability of rituximab (10 mg/kg) in rats was greater after abdominal SC injection (44%), while it was lower (31%) after SC injection in the back. The higher SC dose (40 mg/kg) of rituximab in the back lead to bioavailability of 18%. This indicates saturation of FcRn-mediated protection from proteolysis (5).

Table 1.2: Bioavailability, T_{max}, and C_{max} of various TPs and their relationship with the injection site, population, species or external conditions

TP	PK Parameter	Route	Injection site (Condition/Species)	Reference
	Bioavailability (%)			
Mepolizumab	64	SC	Abdomen (Human)	Ortega et al. (81)
Mepolizumab	75	SC	Arm (Human)	
Mepolizumab	71	SC	Thigh (Human)	
Mepolizumab	81	IM	NA (Human)	
Rituximab	44	SC	Abdomen (Rat-10 mg/kg)	Kagan et al. (5)
Rituximab	31	SC	Back (Rat-10 mg/kg)	
Rituximab	18	SC	Back (Rat-40 mg/kg)	
Adalimumab	64	SC	NA (Human)	Zheng et al. (76)
Adalimumab	83	SC	Inguinal (Minipig)	
Darbepoetin alpha	106	SC	Interdigital (Sheep)	Kota et al. (12)
Darbepoetin alpha	85	SC	Abdomen (Sheep)	
Darbepoetin alpha	92	SC	Shoulder (Sheep)	
	T_{max} (min)			
Insulin	92	SC	Thigh (Human)	Berger et al. (80)
Insulin	76	SC	Arm (Human)	
Insulin	63	SC	Abdomen (Human)	
Insulin	30	SC	Thigh (Hot water bath- Human)	
Insulin	135	SC	Thigh (Cold bath- Human)	
Insulin	38	SC	Thigh (Local massage)	
Insulin lispro	60	SC	Abdomen (Normal weight-Human)	de la Peña et al. (82)
Insulin lispro	90	SC	Abdomen (Obese Human)	
	T_{max} (h)			
Darbepoetin alpha	6-8	SC	Interdigital (Sheep)	Kota et al. (12)
Darbepoetin alpha	18-72	SC	Abdomen (Sheep)	
Darbepoetin alpha	6-12	SC	Shoulder (Sheep)	

	C_{max} (pmol/L)			
Insulin lispro	822	SC	Abdomen (Healthy normal weight-Human)	de la Peña et al. (82)
Insulin lispro	560	SC	Abdomen (Obese Human)	

The rate of absorption of darbepoetin alpha was different for various SC injection sites like interdigital space, abdomen and shoulder. T_{max} for interdigital space, abdomen and shoulder was 6-8, 18-72, and 6-12 h., respectively. These differences may be attributed to alterations in the lymphatic vasculature and characteristics of the SC tissue at various injection sites. In addition, the authors reported that for the SC injection via interdigital space, the lymphatic pathway was a major absorption route (around 90%). While in the case of abdominal SC injection, the lymphatic absorption was around 67% (12).

The studies described above indicate that injection site is an important factor governing bioavailability of the TPs. Change in the bioavailability with different injection sites may be due to differences in the proteolytic degradation in the SC tissue and lymphatic system or variation in the uptake of the TP by lymphatic plexus. A few reports showed that bioavailability, and PK profile of the TP was similar when various injection sites such as abdomen, arm and thigh were compared (83, 84). Nonetheless, SC injection site and the lymphatic system are important for proteolysis of the TPs and can impact their bioavailability and other PK parameters.

1.3.4 Physiological factors responsible for absorption and proteolysis of TPs

The physiological factors related to the SC injection site are important to govern the transport of TPs. For example, obese rats had a bioavailability of around 19%, while normal rats had a bioavailability of around 45% after SC administration of PEGylated erythropoietin. The lymphatic uptake in the fatty/adipose tissue may be reduced leading to low bioavailability. The

proteolytic activity may also change due to the fat content; however, this remains to be investigated further. Higher body weight was associated with lower SC bioavailability in humans (13) and the SC tissue thickness was correlated with the body mass index (BMI). In general, the thickness increased with increasing BMI, and females had higher thickness as compared to males (Figure 1.6) (85). These differences in the SC tissue thickness may lead to altered rate and extent of the absorption. Injection depth relative to the underlying muscle layer will vary with the SC tissue thickness, but it has been shown that the PK of insulin lispro was independent of the injection depth in normal and obese patients (82). In addition, it can be speculated that the body weight and SC tissue thickness are positively correlated with each other. Therefore, it needs to be examined further if reduced bioavailability due to increased body weight was in fact due to increased SC tissue thickness. In another study, it was reported that obese mice had significantly lower lymphatic fluid transport (86). This alteration in the lymph flow may also change transit of the TPs via the lymphatic system and affect overall PK. The TPs would generally first travel through the initial lymphatics (lymphatic capillaries), next through the pre-collecting lymphatics and finally through the collecting lymphatics (lymphatic trunks) and lymphatic ducts (Chapter 2, Figure 2.2). Therefore, lymph flow rates and dimensions of the lymphatic vessels are important physiological factors responsible for lymphatic transport of the TPs (74).

The flow rates and physiology of the lymphatic system play an important role in determining the PK of TPs. In a recent report by Varkhede and Forrest, lymph flows and physiological data related to the lymphatic system were used in a minimal PBPK model to understand the clinical PK of several mAbs (74). Lymphatic capillaries have diameters of around 10 to 60 μm (human) and are connected to the lymphatic trunks via pre-collecting lymphatics (87). The pre-collecting lymphatics have diameters ranging from 35 to 150 μm or sometimes 300 μm

(measured in human thigh) (88). The lymphatic trunks have diameters of around 1-2 mm in the lower limbs. Lymphatic trunks originating from the right-hand side of the head, thorax and right arm; join the right lymphatic duct, which meets the systemic circulation in the right subclavian vein. The lymphatic vessels from the rest of the body (left-hand side of the head, left arm, and lower limbs) are connected to the thoracic duct, which meets systemic circulation at the junction of jugular and left subclavian veins (87).

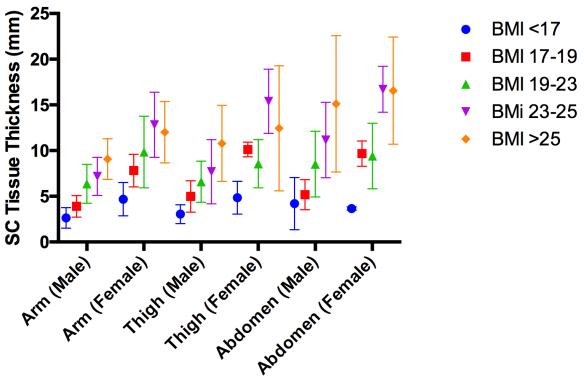

Figure 1.6: SC tissue (insulin injection site) thicknesses in type-2 diabetes adult patients.
Each data point represents mean and standard deviation. BMI: Body mass index (kg/m^2), Male BMI <17 (n=8), female BMI<17 (n=4), male BMI 17-19 (n=11), female BMI 17-19 (n=3), male BMI 19-23 (n=29), female BMI 19-23 (n=14), male BMI 23-25 (n=11), female BMI 23-25 (n=5), male BMI >25 (n=9), female BMI >25 (n=7).
These data were originally reported by Jain et al. (85) (Reproduced with permission).

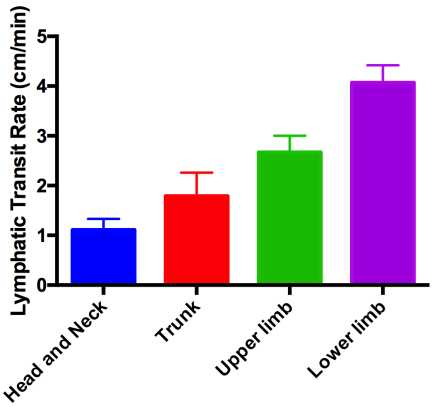

Figure 1.7: Cutaneous lymph flow rates in various regions of the human body
These data were originally published by Fujiwara et al. (89) (Reproduced with permission)

Cutaneous lymph flow rates in melanoma patients were different in various regions of the body as shown in Table 1.3. Hence, absorption of TPs may differ when administered at different injection sites. Skin lymph flow rate in the leg and foot region were approximately 7-fold greater than the head and neck region (90). In another publication, mean cutaneous lymphatic transport rate was reported as highest in the lower limbs (4.07 ± 0.35 cm/min), followed by upper limb (2.67 ± 0.33 cm/min), trunk (1.79 ± 0.47 cm/min), and, head and neck region (1.11 ± 0.22 cm/min) (Figure 1.7) (89).

Table 1.3: Cutaneous lymph flow rates in various body regions in humans

Site	Average flow (cm/min)
Head and neck	1.5
Anterior trunk	2.8
Posterior trunk	3.9
Arm and shoulder	2.0
Forearm and hand	5.5
Thigh	4.2
Leg and foot	10.2

These data were originally published by Uren RF (90) (Reproduced with permission).

The pre-nodal lymph flow measured in the healthy human leg joint was 13.2 ± 1.1 mL/24 h (91). In another study, average afferent lymph flow rate was 10.4 cm/min (human) (92). In the case of sheep, popliteal efferent lymph flow rate was 2 to 10 mL/h (93). Quin et al. also reported afferent (4.58 ± 0.6 mL/h) and efferent (3.87 ± 0.58 mL/h) lymph flow rate for the popliteal lymph node in a sheep (94). Efferent lymph flow for the iliac lymph node in rats was 66 ± 6 μL/h while efferent lymph flow rate from the mesenteric lymph node in rats was 132 ± 41 μL/h (95). The afferent lymph flow rate in dogs was 19.1 ± 0.3 μL/min (96).

In addition, the thoracic lymph duct and right lymphatic ducts are important because most of the lymph generated in the body is transported through either of the two lymph ducts. The thoracic duct lymph flow rate is variable across various species (sheep-5.4 ± 3.1 ml/min, rat-0.038

ml/min) (97, 98). The thoracic duct diameter was of 3.6 ± 0.1 mm in healthy humans (99). In another report, the diameter was reported as a range of 2 to 5 mm. The length of the thoracic lymph duct is around 45 cm (100). Thoracic duct lymph flow was 0.7 to 1.6 mL/kg/h in humans (92). Thoracic duct lymph flow in mouse was 0.83 to 1.66 mL/h, while it was 1 to 10 mL/h (101) or 2.3 mL/h (97) in rats. Various literature values of the thoracic lymph duct flow rates were mentioned by Giragossian et al. (102). Length of the thoracic lymph duct in rats is 3 to 7 cm (101). While, internal diameter of the rat thoracic duct was 405.5 ± 10.1 μm (103) or 0.4 to 1 mm (101). This variation may lead to differences in the PK across and within the species.

It is possible that the number of LNs to which the TP is exposed, would differ after SC injections at various injection sites. For example, if the SC injection site was lower limb or thigh, the TP would travel through the inguinal and iliac LNs. If the TP was administered on the arm, it would pass through the axillary and bronchomediastinal trunk LNs. In both of the cases, number of LNs through which the TP has to pass before reaching the systemic circulation would be different. Due to this differential lymphatic exposure, extent of the lymphatic proteolysis would differ after SC injection at various injection sites (74).

The cutaneous blood flow rates may be important for the absorption of the smaller molecular weight (< 22 kDa) TPs, although they have minimal effect on the larger TPs (e.g. mAbs). Differences in the skin blood flow may result in altered degree of TP absorption and proteolysis (75, 90, 104). Dermal blood flows were different in various animal species and in specific regions of the body such as buttocks, ear, humeroscapular joint, thoracolumbar area, and abdomen (Table 1.4) (105, 106).

Table 1.4: Dermal blood flow (milliliters/minute per 100 gm) in various animal species and in specific regions of the body

Site	Mouse	Rat	Dog	Pig	Monkey
Buttocks	3.88±0.92	4.20±1.05	2.21±0.67	3.08±0.48	3.12±0.58
Ear	1.41±0.48	9.13±4.97	5.21±1.53	11.7±3.02	20.93±5.37
Humeroscapular area	10.10±3.51	6.22±1.47	5.52±1.31	6.75±2.09	8.49±3.28
Thoracolumbar area	20.56±4.69	9.56±2.17	1.94±0.27	2.97±0.56	2.40±0.82
Ventral abdomen	36.85±8.14	11.35±5.53	8.78±1.40	10.68±2.14	3.58±0.41

Each value represents mean and standard error.
These data were originally reported by Monteiro-Riviere et al. (105) (Reproduced with permission).

1.3.5 Effect of the disease and exercise on the physiological parameters related to the lymphatic system

The thoracic lymph flow rate was 1 mL/min in the case of patients without cirrhosis, while, it was 3 to 6 times higher in the cirrhosis patients (107). The thoracic lymph duct flow rate was also measured in pigs, and the impact of lipopolysaccharide (LPS)-induced sepsis was studied. Normal thoracic lymph duct flow in pigs was around 1.5 mL/min; however, the lymph flow rate was doubled after IV LPS administration. This increase in lymph flow was attributed to increased intra-abdominal pressure. LPS sepsis can also increase permeability of the lymphatic capillaries (108). Another study reported that the nodal lymph flow in cancer cell injected nodes was reduced compared to the normal nodes in rats. In the case of normal LNs, lymph flow was 1.49 ± 0.64 ml/gm/min, while it was 0.5 ± 0.24 ml/gm/min for cancer cell injected nodes (109). The pre-nodal lymph flow was 13.2 ± 1.1 mL/24 h for healthy humans (measured in leg joint). However, this lymph flow increased to 22.6 ± 3.2 mL/24 h for rheumatoid arthritis patients (91). Thoracic duct has diameter of 3.6 ± 0.1 mm in healthy humans. The diameter increased (4.8 ± 0.4 mm) in the case of patients with portal hypertension (99). In addition, physical activity or exercise, heat, massage, increase in hydrostatic pressure in the lymph vessels may result in elevated lymph flow.

In contrast, cold, lack of movement and external pressure may lead to reduced lymph flow (75, 90, 104). In addition, the thoracic lymph duct flow in dogs increased while they were exercising. Normal thoracic duct lymph flow was 1.7 mL/min, while, during the exercise (1.5 miles/h on a treadmill), the lymph flow increased by 121% (3.9 mL/min). Further increase in the treadmill speed (10 miles/h) increased the lymph flow by 419% (9 mL/min) (110). In a PK evaluation, the hot water bath and massage elevated the serum insulin levels, while, the cold water bath delayed the absorption (Table 1.2) (80). Overall, the disease states and exercise can alter various lymph flows, which may lead to changes in the PK.

1.3.6 PBPK model for TPs after SC administration

The PBPK models are useful for PK prediction and estimation of the first in human dose for the new chemical entities (TPs and SMDs). The *in vitro* clearance data (e.g. liver microsomes) is used extensively in the PBPK models of SMDs (Chapter 4) (111). However, this strategy has not been used extensively for the TPs. Hence, the *in vitro* proteolysis data generated using SC tissue and lymphatic system may be important for prediction of PK of the TPs using the PBPK model. Giragossian et al. used the serum *in vitro* stability data of the TP in a PBPK model for PK prediction (102). In the Chapter 2 of this dissertation, the minimal PBPK model (Figure 2.1) was used to understand mAb transport in the lymphatic system and to identify physiological and physicochemical factors governing the absorption after SC administration (74). The model described a step-by-step transfer of TPs from the SC interstitial space towards the systemic circulation via lymphatic capillaries, lymphatic trunks, LNs and thoracic duct. We hypothesized that, the TPs are proteolyzed during the lymphatic transit, especially in the LNs. Unfortunately,

the *in vitro* data to describe rate of clearance from the LNs was not available, hence a top-down approach was used with parameter estimation using clinical SC PK data.

Key points and unknowns

The physiological parameters related to the lymphatic system are important for transport of TPs from the SC injection site towards the systemic circulation. These parameters may be altered due to the disease conditions. In addition, the physiological parameters are different across various species, which can lead to differences in the PK and bioavailability. The *in vitro* systems representing the SC and lymphatic tissues can be utilized to generate quantitative proteolysis information. The LN cell suspension may be an appropriate system to account for the proteolysis in the LNs. Finally, the PBPK model can be constructed using the physiological parameters and *in vitro* proteolysis data to understand and predict PK of the TPs.

1.4 Conclusions and Specific Aims

Incomplete bioavailability is a major disadvantage for the TPs administered via SC route. However, mechanism of proteolysis of the TPs in the SC tissue and lymphatic system is not completely known. In the case of SMDs, a bottom up approach is commonly used for PK prediction (Chapter 4). However, this approach has not been utilized widely for TPs. The PBPK model proposed in this dissertation (Chapter 2) can be applied to include the *in vitro* clearance data for the bottom up PK prediction of mAbs. In addition, oxidation is another metabolic process which can potentially alter PK of the TPs. The ROS present in the SC tissue and lymphatic system can oxidize the TP. Furthermore, the iron shredded by the injection needle may oxidize the administered protein. Therefore, following specific aims were designed for this work.

Specific Aim of the Chapter 2: a) To understand the absorption of mAbs via lymphatic system after SC administration using the minimal PBPK model, and b) to demonstrate application of the model for prediction of SC PK of mAbs

Specific Aim of the Chapter 3: a) To evaluate the impact of iron oxide nanoparticles (IONPs) on hydrogen peroxide (H_2O_2)- and 2, 2′-azobis (2-methylpropionamidine) dihydrochloride (AAPH)-mediated oxidation of a model protein, rat growth hormone (rGH), and b) To measure the effect of IONPs on the secondary structure of rGH

Specific Aim of the Chapter 4: To investigate influence of inflammation on the metabolism and PK of midazolam (MDZ) and construct a minimal PBPK model to predict its PK in mice with inflammatory disease

1.5 References

1. Leader B, Baca QJ, Golan DE. Protein therapeutics: a summary and pharmacological classification. Nat Rev Drug Discov. 2008;7(1):21-39
2. Kagan L. Pharmacokinetic Modeling of the Subcutaneous Absorption of Therapeutic Proteins. Drug Metab Dispos. 2014;42(11):1890-1905
3. Porter CJ, Charman SA. Lymphatic transport of proteins after subcutaneous administration. J Pharm Sci. 2000;89(3):297-310
4. Deng R, Meng YG, Hoyte K, Lutman J, Lu Y, Iyer S, DeForge LE, Theil F-P, Fielder PJ, Prabhu S. Subcutaneous bioavailability of therapeutic antibodies as a function of FcRn binding affinity in mice. MAbs. 2012;4(1):101-109
5. Kagan L, Turner MR, Balu-Iyer SV, Mager DE. Subcutaneous absorption of monoclonal antibodies: role of dose, site of injection, and injection volume on rituximab pharmacokinetics in rats. Pharm Res. 2012;29(2):490-499
6. Murakami T, Misaki M, Kojima Y, Yamada M, Yuki M, Higashi Y, Amagase H, Fuwa T, Yata N. Effect of absorption promoters on subcutaneous absorption of human epidermal growth factor in rats. J Pharm Sci. 1993;82(3):236-239

7. Mrsny RJ. Metabolic Processes at Injection Sites Affecting Pharmacokinetics, Pharmacodynamics, and Metabolism of Protein and Peptide Therapeutics. In: Mrsny RJ, Daugherty A, editors. Proteins and Peptides: Pharmacokinetic, Pharmacodynamic, and Metabolic Outcomes. New York, London: Informa Healthcare; 2009. p. 80-105.
8. Dai H, Korthuis RJ. Mast cell proteases and inflammation. Drug Discov Today Dis Models. 2011;8(1):47-55
9. Schellekens H. Factors influencing the immunogenicity of therapeutic proteins. Nephrol Dial Transplant. 2005;20(suppl 6):vi3-vi9
10. Ferl GZ, Theil FP, Wong H. Physiologically-based pharmacokinetic models of small molecules and therapeutic antibodies: mini-review on fundamental concepts and applications. Biopharm Drug Dispos. 2016;37(2):75-92
11. Supersaxo A, Hein WR, Steffen H. Effect of molecular weight on the lymphatic absorption of water-soluble compounds following subcutaneous administration. Pharm Res. 1990;7(2):167-169
12. Kota J, Machavaram KK, McLennan DN, Edwards GA, Porter CJ, Charman SA. Lymphatic absorption of subcutaneously administered proteins: influence of different injection sites on the absorption of darbepoetin alfa using a sheep model. Drug Metab Dispos. 2007;35(12):2211-2217
13. Wang W, Chen N, Shen X, Cunningham P, Fauty S, Michel K, Wang B, Hong X, Adreani C, Nunes CN. Lymphatic transport and catabolism of therapeutic proteins after subcutaneous administration to rats and dogs. Drug Metab Dispos. 2012;40(5):952-962
14. Fraser JR, Kimpton WG, Laurent TC, Cahill RN, Vakakis N. Uptake and degradation of hyaluronan in lymphatic tissue. Biochem J. 1988;256(1):153-158
15. Porter C, Edwards G, Charman S. Lymphatic transport of proteins after sc injection: implications of animal model selection. Adv Drug Del Rev. 2001;50(1):157-171
16. Jenne DE, Tschopp J. Granzymes, a family of serine proteases released from granules of cytolytic T lymphocytes upon T cell receptor stimulation. Immunol Rev. 1988;103(1):53-71
17. van Beers MM, Sauerborn M, Gilli F, Brinks V, Schellekens H, Jiskoot W. Oxidized and aggregated recombinant human interferon beta is immunogenic in human interferon beta transgenic mice. Pharm Res. 2011;28(10):2393-2402
18. Torosantucci R, Schöneich C, Jiskoot W. Oxidation of therapeutic proteins and peptides: structural and biological consequences. Pharm Res. 2014;31(3):541-553
19. Yang Y, Bazhin AV, Werner J, Karakhanova S. Reactive oxygen species in the immune system. Int Rev Immunol. 2013;32(3):249-270
20. Donnelly RF, Singh TRR, Morrow DI, Woolfson AD. Microneedle-Mediated Intradermal Delivery. In. Microneedle-mediated Transdermal and Intradermal Drug Delivery. Chichester, UK: John Wiley & Sons, Ltd.; 2012. p. 113-151.
21. Salmon J, Armstrong C, Ansel J. The skin as an immune organ. West J Med. 1994;160(2):146
22. Heath WR, Carbone FR. The skin-resident and migratory immune system in steady state and memory: innate lymphocytes, dendritic cells and T cells. Nat Immunol. 2013;14(10):978-985
23. Rawlings N, Barrett A. Classification of peptidases by comparison of primary and tertiary structures. Biomed Health Res. 1997;13:13-21
24. Bond JS, Butler PE. Intracellular proteases. Annu Rev Biochem. 1987;56(1):333-364

25. Barrett AJ. Classification of peptidases. Methods Enzymol. 1994;244:1-15
26. Barrett AJ. Peptidases: a view of classification and nomenclature. In: Turk V, editor. Proteases New Perspectives. Basel, Switzerland: Birkhäuser; 1999. p. 1-12.
27. Veer SJ, Furio L, Harris JM, Hovnanian A. Proteases and proteomics: Cutting to the core of human skin pathologies. Proteomics Clin Appl. 2014;8(5-6):389-402
28. Suga Y, Takamori K, Ogawa H. Skin proteasomes (high-molecular-weight protease): purification, enzymologic properties, gross structure, and tissue distribution. J Invest Dermatol. 1993;101(3):346-351
29. Clark RA. Skin-resident T cells: the ups and downs of on site immunity. J Invest Dermatol. 2010;130(2):362-370
30. De Luca A, De Falco M, Severino A, Campioni M, Santini D, Baldi F, Paggi MG, Baldi A. Distribution of the serine protease HtrA1 in normal human tissues. J Histochem Cytochem. 2003;51(10):1279-1284
31. Kambara T, Hiraoka T, Kukita I. Neutral proteases in lymph node cells of rabbits immunized with heat-killed tubercle bacilli. Kumamoto Med J. 1985;38(3-4):153-163
32. Kageyama T, Moriyama A, Kato T, Sano M, Yonezawa S. Determination of Cathepsins D and E in Various Tissues and Cells of Rat, Monkey, and Man by the Assay with β-Endorphin and Substance P as Substrates. Zoolog Sci. 1996;13(5):693-698
33. Björk P, Luts A, Sundler F, Ohlsson K. Turnover and distribution of cathepsin G in the rat. Scand J Clin Lab Invest. 1993;53(6):539-546
34. Shin JW, Jurisic G, Detmar M. Lymphatic-specific expression of dipeptidyl peptidase IV and its dual role in lymphatic endothelial function. Exp Cell Res. 2008;314(16):3048-3056
35. Richter WF, Bhansali SG, Morris ME. Mechanistic determinants of biotherapeutics absorption following SC administration. AAPS J. 2012;14(3):559-570
36. Labat-Robert J, Fourtanier A, Boyer-Lafargue B, Robert L. Age dependent increase of elastase type protease activity in mouse skin: Effect of UV-irradiation. J Photochem Photobiol B: Biol. 2000;57(2):113-118
37. Romero-Quintana JG, Frías-Castro LO, Arámbula-Meraz E, Aguilar-Medina M, Dueñas-Arias JE, Melchor-Soto JD, Romero-Navarro JG, Ramos-Payán R. Identification of novel mutation in cathepsin C gene causing Papillon-Lefèvre Syndrome in Mexican patients. BMC Med Genet. 2013;14(1):1
38. Kirschke H, Joronen I, Rinne A, Järvinen M, Hopsu-Havu VK. Overexpression of Cathepsins B, H, L and S in Malignant Tumors of the Lymph Node. In: Hopsu-Havu VK, Järvinen M, Krischke H, editors. Proteolysis in Cell Functions. Amsterdam, Netherlands: IOS Press; 1997. p. 479-484.
39. Basel-Vanagaite L, Attia R, Ishida-Yamamoto A, Rainshtein L, Amitai DB, Lurie R, Pasmanik-Chor M, Indelman M, Zvulunov A, Saban S. Autosomal recessive ichthyosis with hypotrichosis caused by a mutation in ST14, encoding type II transmembrane serine protease matriptase. Am J Hum Genet. 2007;80(3):467-477
40. Blaydon DC, Biancheri P, Di W-L, Plagnol V, Cabral RM, Brooke MA, van Heel DA, Ruschendorf F, Toynbee M, Walne A. Inflammatory skin and bowel disease linked to ADAM17 deletion. N Engl J Med. 2011;365(16):1502-1508
41. Saarialho-Kere U, Kerkelä E, Jahkola T, Suomela S, Keski-Oja J, Lohi J. Epilysin (MMP-28) expression is associated with cell proliferation during epithelial repair. J Invest Dermatol. 2002;119(1):14-21

42. Titeux M, Pendaries V, Tonasso L, Décha A, Bodemer C, Hovnanian A. A frequent functional SNP in the MMP1 promoter is associated with higher disease severity in recessive dystrophic epidermolysis bullosa. Hum Mutat. 2008;29(2):267-276
43. Kubota T, Iizuka H, Bachovchin W, Stollar B. Dipeptidyl peptidase IV (DP IV) activity in serum and on lymphocytes of MRL/Mp-lpr/lpr mice correlates with disease onset. Clin Exp Immunol. 1994;96(2):292-296
44. Raynaud F, Bauvois B, Gerbaud P, Evain-Brion D. Characterization of specific proteases associated with the surface of human skin fibroblasts, and their modulation in pathology. J Cell Physiol. 1992;151(2):378-385
45. Fischer H, Stichenwirth M, Dockal M, Ghannadan M, Buchberger M, Bach J, Kapetanopoulos A, Declercq W, Tschachler E, Eckhart L. Stratum corneum-derived caspase-14 is catalytically active. FEBS Lett. 2004;577(3):446-450
46. Brockow K, Abeck D, Hermann K, Ring J. Tryptase concentration in skin blister fluid from patients with bullous skin conditions. Arch Dermatol Res. 1996;288(12):771-773
47. De Veer SJ, Furio L, Harris JM, Hovnanian A. Proteases: common culprits in human skin disorders. Trends Mol Med. 2014;20(3):166-178
48. Rodgers UR, Kevorkian L, Surridge AK, Waters JG, Swingler TE, Culley K, Illman S, Lohi J, Parker AE, Clark IM. Expression and function of matrix metalloproteinase (MMP)-28. Matrix Biol. 2009;28(5):263-272
49. Payne V, Kam P. Mast cell tryptase: a review of its physiology and clinical significance. Anaesthesia. 2004;59(7):695-703
50. Ham SA, Yoo T, Hwang JS, Kang ES, Paek KS, Park C, Kim J-H, Do JT, Seo HG. Peroxisome proliferator-activated receptor δ modulates MMP-2 secretion and elastin expression in human dermal fibroblasts exposed to ultraviolet B radiation. J Dermatol Sci. 2014;76(1):44-50
51. Harvima IT, Schechter NM, Harvima RJ, Fräki JE. Human skin tryptase: purification, partial characterization and comparison with human lung tryptase. Biochim Biophys Acta, Protein Struct Mol Enzymol. 1988;957(1):71-80
52. Desnoyers LR, Vasiljeva O, Richardson JH, Yang A, Menendez EE, Liang TW, Wong C, Bessette PH, Kamath K, Moore SJ. Tumor-specific activation of an EGFR-targeting probody enhances therapeutic index. Sci Transl Med. 2013;5(207):207ra144-207ra144
53. Takeyama M, Ishida T, Kokubu N, Komada F, Iwakawa S, Okumura K, Hori R. Enhanced bioavailability of subcutaneously injected insulin by pretreatment with ointment containing protease inhibitors. Pharm Res. 1991;8(1):60-64
54. Bruno BJ, Miller GD, Lim CS. Basics and recent advances in peptide and protein drug delivery. Ther Deliv. 2013;4(11):1443-1467
55. Amancha KP, Hussain A. Effect of protease inhibitors on pulmonary bioavailability of therapeutic proteins and peptides in the rat. Eur J Pharm Sci. 2015;68:1-10
56. Hall MP. Biotransformation and in vivo stability of protein biotherapeutics: impact on candidate selection and pharmacokinetic profiling. Drug Metab Dispos. 2014;42(11):1873-1880
57. Varkhede N, Patel N, Chang W, Ruterbories K, Forrest ML. A Semi-Physiologically Based Pharmacokinetic Model Describing the Altered Metabolism of Midazolam Due to Inflammation in Mice. Pharm Res. 2018;35(8):162
58. Kagan L, Mager DE. Mechanisms of subcutaneous absorption of rituximab in rats. Drug Metab Dispos. 2013;41(1):248-255

59. Fathallah AM, Turner MR, Mager DE, Balu-Iyer SV. Effects of hypertonic buffer composition on lymph node uptake and bioavailability of rituximab, after subcutaneous administration. Biopharm Drug Dispos. 2015;36(2):115-125
60. Boswell CA, Deng R, Lin K, Putnam WS, Lei C, Theil F-P, Joshi A, Fielder PJ, Khawli LA, Mrsny R. In vitro-in vivo correlations of pharmacokinetics, pharmacodynamics and metabolism for antibody therapeutics. In: Mrsny RJ, Daugherty A, editors. Proteins and Peptides: Pharmacokinetic, Pharmacodynamic, and Metabolic Outcomes. New York, London: Informa Healthcare; 2009. p. 15-52.
61. Gill KL, Gardner I, Li L, Jamei M. A bottom-up whole-body physiologically based pharmacokinetic model to mechanistically predict tissue distribution and the rate of subcutaneous absorption of therapeutic proteins. AAPS J. 2016;18(1):156-170
62. Malm-Erjefält M, Bjørnsdottir I, Vanggaard J, Helleberg H, Larsen U, Oosterhuis B, van Lier JJ, Zdravkovic M, Olsen AK. Metabolism and excretion of the once-daily human glucagon-like peptide-1 analog liraglutide in healthy male subjects and its in vitro degradation by dipeptidyl peptidase IV and neutral endopeptidase. Drug Metab Dispos. 2010;38(11):1944-1953
63. Ito Y, Murano H, Hamasaki N, Fukushima K, Takada K. Incidence of low bioavailability of leuprolide acetate after percutaneous administration to rats by dissolving microneedles. Int J Pharm. 2011;407(1):126-131
64. Macdougall IC, Roberts DE, Coles GA, Williams JD. Clinical pharmacokinetics of epoetin (recombinant human erythropoietin). Clin Pharmacokinet. 1991;20(2):99-113
65. Charman SA, Segrave AM, Edwards GA, Porter CJ. Systemic availability and lymphatic transport of human growth hormone administered by subcutaneous injection. J Pharm Sci. 2000;89(2):168-177
66. Stein O, Fruton JS. Proteinase activity of rat lymph nodes. Yale J Biol Med. 1960;33(1):71
67. Quirós PM, Langer T, López-Otín C. New roles for mitochondrial proteases in health, ageing and disease. Nat Rev Mol Cell Biol. 2015;16(6):345
68. Kinnunen HM, Sharma V, Contreras-Rojas LR, Yu Y, Alleman C, Sreedhara A, Fischer S, Khawli L, Yohe ST, Bumbaca D. A novel in vitro method to model the fate of subcutaneously administered biopharmaceuticals and associated formulation components. J Control Release. 2015;214:94-102
69. Wroblewski VJ, Witcher DR, Becker GW, Davis KA, Dou S, Micanovic R, Newton CM, Noblitt TW, Richardson JM, Song HY. Decoy receptor 3 (DcR3) is proteolytically processed to a metabolic fragment having differential activities against Fas ligand and LIGHT. Biochem Pharmacol. 2003;65(4):657-667
70. Bessire AJ, Ballard TE, Charati M, Cohen JD, Green ME, Lam M-H, Loganzo F, Nolting B, Pierce B, Puthenveetil S. Determination of Antibody-Drug Conjugate Released Payload Species Using Directed in Vitro Assays and Mass Spectrometric Interrogation. Bioconjug Chem. 2016
71. Doronina SO, Bovee TD, Meyer DW, Miyamoto JB, Anderson ME, Morris-Tilden CA, Senter PD. Novel Peptide Linkers for Highly Potent Antibody− Auristatin Conjugate. Bioconjug Chem. 2008;19(10):1960-1963
72. Kamath AV, Iyer S. Preclinical pharmacokinetic considerations for the development of antibody drug conjugates. Pharm Res. 2015;32(11):3470-3479

73. Doronina SO, Mendelsohn BA, Bovee TD, Cerveny CG, Alley SC, Meyer DL, Oflazoglu E, Toki BE, Sanderson RJ, Zabinski RF. Enhanced activity of monomethylauristatin F through monoclonal antibody delivery: effects of linker technology on efficacy and toxicity. Bioconjug Chem. 2006;17(1):114-124
74. Varkhede N, Forrest L. Understanding the monoclonal antibody disposition after subcutaneous administration using a minimal physiologically based pharmacokinetic model. J Pharm Pharm Sci. 2018;21(1s):130-148s
75. McDonald TA, Zepeda ML, Tomlinson MJ, Bee WH, Ivens IA. Subcutaneous administration of biotherapeutics: current experience in animal models. Curr Opin Mol Ther. 2010;12(4):461-470
76. Zheng Y, Tesar DB, Benincosa L, Birnböck H, Boswell CA, Bumbaca D, Cowan KJ, Danilenko DM, Daugherty AL, Fielder PJ. Minipig as a potential translatable model for monoclonal antibody pharmacokinetics after intravenous and subcutaneous administration. MAbs. 2012;4(2):243-255
77. Jørgensen J, Flyvbjerg A, Lauritzen T, Ørskov H, Christiansen J. Subcutaneous degradation of biosynthetic human growth hormone in growth hormone deficient patients. Acta Endocrinol (Copenh). 1988;118(1):154-158
78. Okumura K, Komada F, Hori R. Fate of porcine and human insulin at the subcutaneous injection site. I. degradation and absorption of insulins in the rat. J Pharmacobiodyn. 1985;8(1):25-32
79. Beshyah SA, Anyaoku V, Niththyananthan R, Sharp P, Johnston DG. The effect of subcutaneous injection site on absorption of human growth hormone: abdomen versus thigh. Clin Endocrinol (Oxf). 1991;35(5):409-412
80. Berger M, Cüppers H, Hegner H, Jörgens V, Berchtold P. Absorption kinetics and biologic effects of subcutaneously injected insulin preparations. Diabetes Care. 1982;5(2):77-91
81. Ortega H, Yancey S, Cozens S. Pharmacokinetics and absolute bioavailability of mepolizumab following administration at subcutaneous and intramuscular sites. Clin Pharmacol Drug Dev. 2014;3(1):57-62
82. de la Peña A, Yeo KP, Linnebjerg H, Catton E, Reddy S, Brown-Augsburger P, Morrow L, Ignaut DA. Subcutaneous injection depth does not affect the pharmacokinetics or glucodynamics of insulin lispro in normal weight or healthy obese subjects. J Diabetes Sci Technol. 2015;9(4):824-830
83. Xu Z, Wang Q, Zhuang Y, Frederick B, Yan H, Bouman-Thio E, Marini JC, Keen M, Snead D, Davis HM. Subcutaneous bioavailability of golimumab at 3 different injection sites in healthy subjects. J Clin Pharmacol. 2010;50(3):276-284
84. Calara F, Taylor K, Han J, Zabala E, Carr EM, Wintle M, Fineman M. A randomized, open-label, crossover study examiningthe effect of injection site on bioavailability of exenatide (synthetic exendin-4). Clin Ther. 2005;27(2):210-215
85. Jain SM, Pandey K, Lahoti A, Rao PK. Evaluation of skin and subcutaneous tissue thickness at insulin injection sites in Indian, insulin naïve, type-2 diabetic adult population. Indian J Endocrinol Metab. 2013;17(5):864
86. Weitman ES, Aschen SZ, Farias-Eisner G, Albano N, Cuzzone DA, Ghanta S, Zampell JC, Thorek D, Mehrara BJ. Obesity impairs lymphatic fluid transport and dendritic cell migration to lymph nodes. PLoS One. 2013;8(8):e70703

87. Margaris K, Black RA. Modelling the lymphatic system: challenges and opportunities. J R Soc Interface. 2012;9(69):601-612
88. Sacchi G, Weber E, Agliano M, Raffaelli N, Comparini L. The structure of superficial lymphatics in the human thigh: precollectors. Anat Rec. 1997;247(1):53-62
89. Fujiwara M, Sawada M, Kasuya A, Matsushita Y, Yamada M, Fukamizu H, Magata Y, Tokura Y, Sakahara H. Measurement of cutaneous lymphatic flow rates in patients with skin cancer: area extraction method. J Dermatol. 2014;41(6):498-504
90. Uren RF. Lymphatic drainage of the skin. Ann Surg Oncol. 2004;11(3):179S-185S
91. Olszewski WL, Pazdur J, Kubasiewicz E, Zaleska M, Cooke CJ, Miller NE. Lymph draining from foot joints in rheumatoid arthritis provides insight into local cytokine and chemokine production and transport to lymph nodes. Arthritis Rheumatol. 2001;44(3):541-549
92. Nathanson SD, Nelson L, Karvelis KC. Rates of flow of technetium 99m-labeled human serum albumin from peripheral injection sites to sentinel lymph nodes. Ann Surg Oncol. 1996;3(4):329-335
93. Hall JG, Morris B. The output of cells in lymph from the popliteal node of sheep. Exp Physiol. 1962;47(4):360-369
94. Quin J, Shannon A. The influence of the lymph node on the protein concentration of efferent lymph leaving the node. J Physiol. 1977;264(2):307-321
95. Suzuki S, Mizuno R, Ikomi F, Ohhashi T. Head-down tilt posture elicits transient lymphocyte mobilization from the iliac, but not mesenteric, lymph nodes of rats. J Appl Physiol. 2008;105(5):1595-1601
96. Adair TH, Guyton AC. Modification of lymph by lymph nodes. II. Effect of increased lymph node venous blood pressure. Am J Physiol Heart Circ Physiol. 1983;245(4):H616-H622
97. Ionac M. One technique, two approaches, and results: thoracic duct cannulation in small laboratory animals. Microsurgery. 2003;23(3):239-245
98. Onizuka M, FlatebØ T, Nicolaysen G. Lymph flow pattern in the intact thoracic duct in sheep. J Physiol. 1997;503(1):223-234
99. De-xin Y, Xiang-xing M, Xiao-ming Z, Qing W, Chuan-fu L. Morphological features and clinical feasibility of thoracic duct: detection with nonenhanced magnetic resonance imaging at 3.0 T. J Magn Reson Imaging. 2010;32(1):94-100
100. Skandalakis JE, Skandalakis LJ, Skandalakis PN. Anatomy of the lymphatics. Surg Oncol Clin N Am. 2007;16(1):1-16
101. Ganusov VV, Auerbach J. Mathematical modeling reveals kinetics of lymphocyte recirculation in the whole organism. PLoS Comput Biol. 2014;10(5):e1003586
102. Giragossian C, Vage C, Li J, Pelletier K, Piché-Nicholas N, Rajadhyaksha M, Liras J, Logan A, Calle RA, Weng Y. Mechanistic Investigation of the Preclinical Pharmacokinetics and Interspecies Scaling of PF-05231023, a Fibroblast Growth Factor 21–Antibody Protein Conjugate. Drug Metab Dispos. 2015;43(6):803-811
103. Gashev AA, Zhang R-Z, Muthuchamy M, Zawieja DC, Davis MJ. Regional heterogeneity of length–tension relationships in rat lymph vessels. Lymphat Res Biol. 2012;10(1):14-19
104. Jensen J, Jensen L, Madsen J. The pharmacokinetics of recombinant human erythropoietin after subcutaneous injection at different sites. Eur J Clin Pharmacol. 1994;46(4):333-337

105. Monteiro-Riviere NA, Bristol DG, Manning TO, Rogers RA, Riviere JE. Interspecies and interregional analysis of the comparative histologic thickness and laser Doppler blood flow measurements at five cutaneous sites in nine species. J Invest Dermatol. 1990;95(5):582-586
106. Brown R, Delp M, Lindstedt S, Rhomberg L, Beliles R. Physiological parameter values for physiologically based pharmacokinetic models. Toxicol Ind Health. 1997;13407:484
107. Dumont AE, Mulholland JH. Flow rate and composition of thoracic-duct lymph in patients with cirrhosis. N Engl J Med. 1960;263(10):471-474
108. Malbrain M, Pelosi P, De Laet I, Lattuada M, Hedenstierna G. Lymphatic drainage between thorax and abdomen: please take good care of this well-performing machinery…. Acta Clin Belg. 2007;62(sup1):152-161
109. DSouza AV, Elliott JT, Gunn JR, Barth RJ, Samkoe KS, Tichauer KM, Pogue BW. Nodal lymph flow quantified with afferent vessel input function allows differentiation between normal and cancer-bearing nodes. Biomed Opt Express. 2015;6(4):1304-1317
110. Desai P, Williams Jr AG, Prajapati P, Downey HF. Lymph flow in instrumented dogs varies with exercise intensity. Lymphat Res Biol. 2010;8(3):143-148
111. Zhuang X, Lu C. PBPK modeling and simulation in drug research and development. Acta Pharm Sin B. 2016;6(5):430-440

Chapter 2 : Understanding the monoclonal antibody disposition after subcutaneous administration using a minimal physiologically based pharmacokinetic model

2.1 Introduction

Monoclonal antibodies (mAbs) are an important class of therapeutic proteins (TPs) administered mainly via the subcutaneous (SC) route due to shorter clinical visits for patients, the possibility of self-administration, and its less invasive nature. However, when compared to the intravenous (IV) route, SC injection has challenges associated with the incomplete bioavailability and pain-free administration of larger fluid volumes (1). The SC tissue and lymphatic system are important barriers for the absorption of mAbs. After SC administration, the mAbs travel through the lymphatic vessels and lymph nodes before reaching the systemic circulation. The SC bioavailability of mAbs is typically in the range of 52 to 80% (2, 3). Proteolysis within the lymphatic system and the SC injection site may be partially responsible for the reduced bioavailability of mAbs. The rate of neonatal Fc receptor (FcRn) binding and recycling exceeds the rate of lysosomal/endosomal trafficking of mAbs; therefore, endosomal proteolysis may contribute only minimally to low mAb bioavailability (3, 4). In addition, the target mediated drug disposition (TMDD) is often saturated due to limited receptors. Thus, mAbs are cleared slowly from the systemic circulation. The TPs like IgG1, IgG2 and IgG4 have a long half-life of around 23 days (3), which is substantially longer than other proteins of similar molecular weights. Further, the appearance rate of mAbs in the plasma is slow (T_{max} generally 2-14 days) (3). The low bioavailability of mAbs may result from efficient pre-systemic clearance mechanisms or irreversible retention (and subsequent elimination) of significant dose at the injection site or in the surrounding tissues.

Charman et al. investigated the causes of reduced bioavailability of human growth hormone (hGH) protein using a sheep model. The SC injection site degradation was minimal for hGH, while the lymphatic proteolysis was mainly responsible for its reduced bioavailability after SC administration (5). We hypothesize that the interstitial proteolysis in the lymphatic system may be responsible for lower bioavailability of mAbs after SC administration. In this study, a minimal physiologically based pharmacokinetic (PBPK) model was used to understand the sequential transit of mAbs and to estimate lymphatic clearance using the SC pharmacokinetics (PK). The model was constructed using physiological parameters related to the SC injection site, lymphatic system and the reported clinical IV PK data. This study had the following major objectives: a) construction of the minimal PBPK model focusing on the lymphatic transit of mAbs after SC administration using physiologically relevant lymph flows and compartment volumes, b) estimation of the lymphatic clearance using literature SC PK data, and c) identification of the parameters governing the absorption of mAbs via the SC and lymphatic system.

Various PBPK models for TPs have been reported recently and as early as 1995 (Gill et al., Abbuqayyas and Balthasar, Garg and Balthasar, Baxter et al., Shah and Betts) (6-9). Some of the authors (Zhao et al., Chen et al., Elmeliegy et al., Li et al.) proposed the minimal PBPK approach to eliminate complexity associated with the models (3, 10-12). Although, these models may be useful for a mechanistic understanding of the clearance and absorption processes at the SC injection site and in the lymphatic system, use of PBPK modeling for TP PK prediction is limited (13). After SC injection, the mAb travels through the lymphatic capillary network, lymph nodes, lymphatic trunks and thoracic lymph duct before joining the systemic circulation. Hence, in this study, the lymphatic organs were incorporated in the minimal PBPK model, and the lymphatic trunk-lymph node (LN) clearance was estimated using the SC PK. Interestingly, it appears that the

estimated lymphatic trunk-LN clearance was directly proportional to the isoelectric point (*pI*) of the mAb. In addition, the model must be combined in the future with *in vitro* proteolysis data obtained from the lymphatic system to predict SC PK and bioavailability of mAbs. Further, the variability in the PK due to different populations, disease conditions, formulations, novel delivery technologies, and biophysical properties of the TP may be addressed using the minimal PBPK model (14). Overall, the proposed minimal PBPK model can be used for mechanistic understanding of mAb absorption and prediction of PK after SC administration.

2.2 Methods

2.2.1 Digitization of literature IV and SC PK data

The IV (35 profiles) and SC (37 profiles) PK of 10 mAbs were obtained from literature and digitized using WebPlotDigitizer (version 4.1) (15). This web-based tool has been extensively used in other reports (16). The IV PK profiles were used to estimate 2-compartment model parameters, while the SC PK profiles were used to estimate the lymphatic trunk-LN clearance.

2.2.2 Construction of the minimal PBPK model

The minimal PBPK model was constructed using SimBiology (Matlab R2017a). The physiologically based model and simple compartmental model were combined to describe absorption of mAbs after SC administration (Figure 2.1). The model equations describing FcRn binding and transfer across interstitial, endosomal and vascular space were adopted from previously reported studies (3, 9, 17). However, additional physiological parameters related to the lymphatic system were either calculated or obtained from the literature (Table 2.1) and used to construct the model. The model parameters specific to mAbs are listed in Table 2.2. Furthermore,

additional compartments were included to describe the sequential transfer of mAbs through the lymphatic system. It was assumed that the SC dose of mAb distributes equally in the SC interstitial space after the injection.

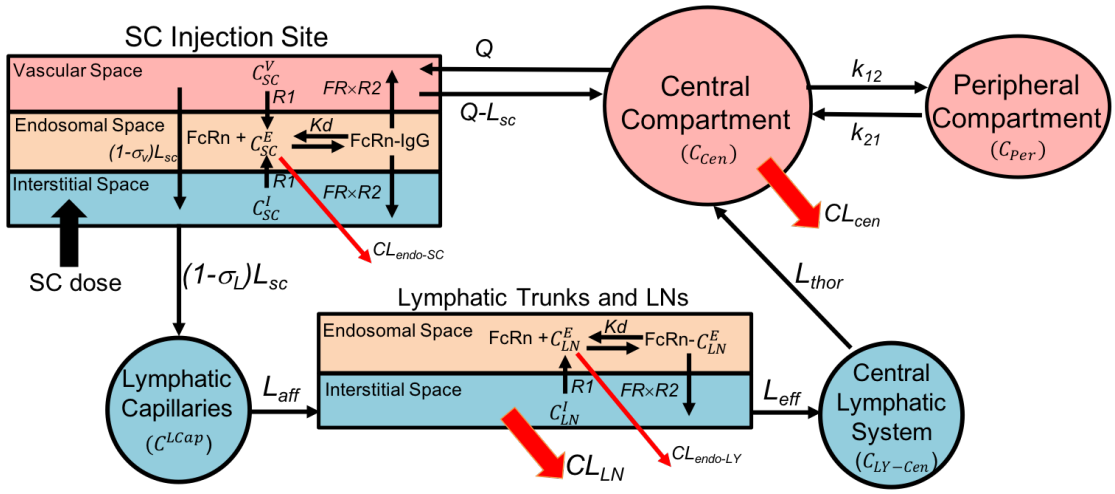

Figure 2.1: Schematic representation of the minimal PBPK model for mAb absorption after SC injection

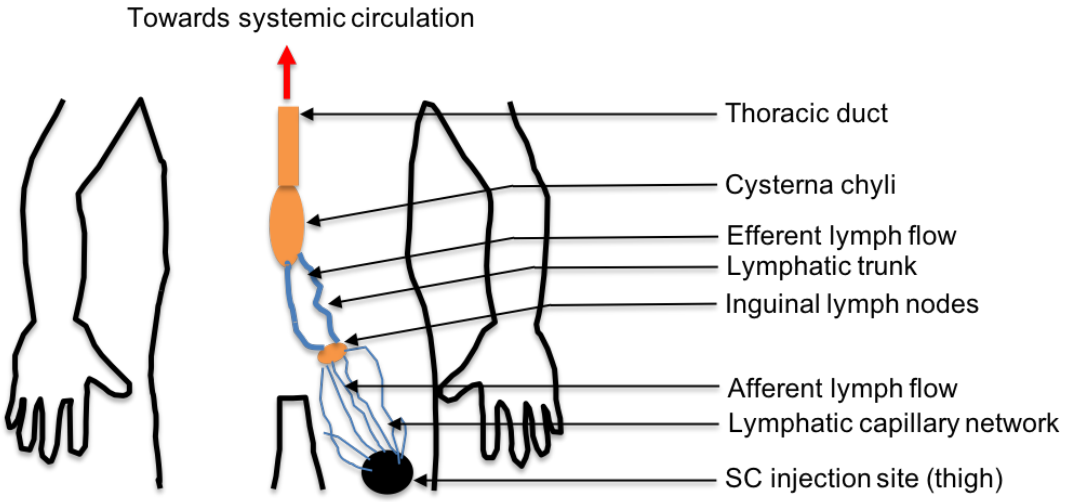

Figure 2.2: Schematic representation of flow of mAbs or TPs after SC injection in thigh

2.2.3 Physiological parameters related to the SC injection site and lymphatic system

The physiological parameters related to the SC injection site and lymphatic system were either obtained or calculated from the literature (Table 2.1). The SC injection site volume was calculated by Gill et al. (9) using the diameter of the SC injection depot of radiolabeled IgG. While, the SC site lymph flow was measured using the rate of radiolabeled IgG loss from a SC administration site (9). Lymphatic capillary volume was calculated using the average distance between the injection site and sentinel LN (30 cm), the lymphatic network density per 1 cm annulus of arm skin (385 cm), and the average radius of lymphatic capillaries (0.0274 mm) (18-20). Afferent lymph flow was calculated using the reported lymphatic flow rate (40 mm/min) and radius (0.0274 mm) of the lymphatic capillaries in humans (21, 22). The efferent lymph flow rate in sheep was used in the model (23). The volume of the lymphatic trunk was calculated based on an approximate length of 30 cm and a radius of 1 mm (20).

The total LN volume was calculated based on the number of LNs (45 to 50) to which the mAb is exposed after SC injection in thigh (24-26). The average volume of cervical LNs (0.292 mL) reported in humans was used to calculate the total LN volume after SC injection in the upper arm, abdomen, and thigh (27). The SC injection of a TP in thigh would lead to its travel through the inguinal, iliac and lumbar LNs (Figure 2.2). Upon SC injection in the upper arm, the TP would travel through the cubital and axillary LNs followed by the subclavian trunk. After passing through the LNs and lymphatic trunks, TPs would join the central lymphatic system (thoracic duct and cysterna chyli), which are lymphatic vessels with greater diameters. The TP would join the systemic circulation via the thoracic duct if the SC injection site were left upper arm, whereas injections into the right upper arm, would enter either via the right thoracic duct or thoracic lymph

duct (Figure 2.3). After abdominal SC injection, the TP would generally travel via inguinal, iliac, and lumbar LNs towards the cisterna chyli and thoracic duct, to enter the systemic blood circulation via the subclavian vein. The known anatomical structure of lymphatic system was utilized to define the sequential transfer of mAbs (24-27).

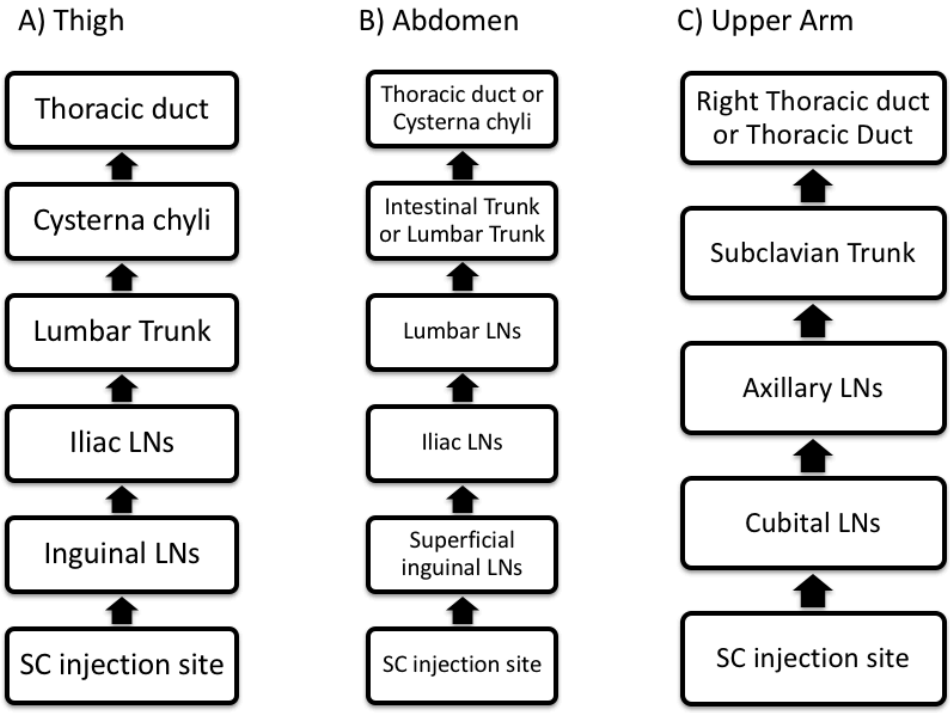

Figure 2.3: Sequential transfer of mAbs towards the systemic circulation after SC injection in, A) Thigh, B) Abdomen, and C) Upper Arm

The lymphatic trunk and LN volumes were combined to calculate the interstitial lymphatic trunk-LN volume. The total endosomal volume of LNs was calculated based on the endosomal volume in a peripheral mononuclear cell (28) and the number of lymphocytes in a LN (29). The endosomal LN volume and the combined lymphatic trunk-LN interstitial volume for various SC injection sites (thigh, abdomen, and upper arm) were approximately similar (Table 2.1).

The central lymphatic system's volume was dependent on the site of SC injection. In the case of SC injection to the thigh, abdomen or left upper arm, the TP would travel through the

thoracic lymph duct. In the case of thigh and abdominal injections, volume of the cisterna chyli should be included in the central lymphatic volume. For this model, it was assumed that the SC injection site was either thigh or abdomen, therefore, the volume of the thoracic duct and cisterna chyli were included in the central lymphatic volume. However, the volume of the central lymphatic system after injection in an upper arm or thigh was found to be similar, because the volume of the cisterna chyli was negligible as compared to the thoracic duct volume (Table 2.1). Volumes of the thoracic lymph duct and cisterna chyli were calculated based on literature values of length and diameter. In the case of the thoracic lymph duct, the length and diameter were 45 and 5 cm, respectively. While, in the case of cisterna chyli, the length and diameter were 2-5 mm and 1 cm, respectively (30).

Table 2.1: Human physiological parameters related to the SC injection site and lymphatic system

Parameter	Value	Reference
V_{SC}^{I} (SC injection site interstitial volume)	0.003115 L	(9)
V_{SC}^{E} (SC injection site endosomal volume)	0.000025 L	(9)
V_{SC}^{V} (SC injection site vascular volume)	0.00025 L	(9)
V^{LCap} (Volume of the lymphatic capillaries)	0.00033 L	Calculated (18-20)
V_{LY-UA}^{I} (Combined interstitial volume of lymphatic trunk and LNs after SC injection in upper arm)[a]	0.01408 L	Calculated (24-27)
V_{LY}^{I} (Combined interstitial volume of lymphatic trunk and LNs after SC injection in thigh)	0.01349 L	Calculated (25-27, 31)
V_{LY-Ab}^{I} (Combined interstitial volume of lymphatic trunk and LNs after SC injection in abdomen)[a]	0.01758 L	Calculated (25-27, 32)
V_{LY-UA}^{E} (Combined endosomal volume of all LNs to which the mAb is exposed after SC injection in upper arm)[a]	0.000014 mL	Calculated (24-29)
V_{LY}^{E} (Combined endosomal volume of all LNs to which the mAb is exposed after SC injection in thigh)	0.0000126 mL	Calculated (28, 29, 31)
V_{LY-Ab}^{E} (Combined endosomal volume of all LNs to which the mAb is exposed after SC injection in abdomen)	0.00001596 mL	Calculated (25-29, 32)
V_{LY-Cen} (Volume of central lymphatic system)	0.00888 L	Calculated (30)
V_{Thor} (Volume of thoracic lymph duct)[b]	0.00884 L	Calculated (30)
V_{CC} (Volume of cisterna chyli)[b]	0.000039 L	Calculated (30)
L_{SC} (Lymph flow at the SC injection site)	0.0001356 L/h	(9)
L_{Aff} (Lymph flow afferent to LNs in human)	0.00000564 L/h	Calculated (21, 22)

L_{Eff} (Lymph flow efferent to LNs in sheep)	0.00387 L/h	(23)
L_{Thor} (Thoracic duct lymph flow rate)	0.06 L/h	(33, 34)
Q_{SC} (Blood flow at the SC injection site)	0.04992 L/h	(9)
C_{Endo} (Concentration of endogenous mAb in endosomal compartment)	10000 mg/L	(3)
Kd (Dissociation constant for antibody FcRn binding)	45.36 mg/L	(35)
nPt (FcRn concentration in SC tissue or LNs)	2880 mg/L	(36)

[a]*Not used in the model (SC injection site was assumed as thigh)*
[b]*Used to calculate total central lymphatic volume*

Table 2.2: mAb related parameters used in the minimal PBPK model

Parameter	Value	Reference
σ_V (Vascular reflection coefficient)	0.95	(3, 17)
σ_L (Lymphatic reflection coefficient)	0.2	(3, 17)
$R1$ (Endosomal uptake rate of antibody)	0.00000926 /h	(3, 4)
$R2$ (Endosomal return rate of antibody)	0.26 /h	(3, 4)
FR (Recycling fraction of FcRn bound mAb)	0.715	(3)
$CL_{Endo-SC}$ (Endosomal clearance of mAb in SC injection site)[a]	0.003675 L/h	(17)
$CL_{Endo-LY}$ (Endosomal clearance of antibody in LNs)[b]	0.0001254 L/h	(17)

[a]*Endosomal clearance in skin assumed to be similar to SC injection site*
[b]*Endosomal clearance in spleen assumed to be similar to lymphatic trunk-LN*

2.2.4 Parameter estimation and sensitivity analysis

A nonlinear mixed-effects model with stochastic EM algorithm was used for estimation of the 2-compatmental IV PK parameters. The lymphatic trunk-LN clearance was estimated using either the nonlinear mixed-effects model with stochastic EM algorithm or a nonlinear least squares solver. Sensitivity analysis was performed on the physiological, mAb related and estimated parameters (Figure 2.9 S1 and Figure 2.10 S2). The parameters were altered by 0.1-, 0.3-, 0.5-, 0.7-, 1-, 3-, 5-, 7-, 10-, 50- and 100-fold of the original values as mentioned in Table 2.1. The lymphatic reflection coefficient was altered by 0.1-, 0.3-, 0.5-, 0.7-, 1-, 1.5-, 2-, 2.5-, 3-, 3.5-, 4-, 4.5-, 5- folds of the original parameter value and its impact on the PK of mAbs was determined.

2.2.5 Model validation

The model was validated by comparing observed and predicted PK profiles after SC administration. In addition, accuracy of the predictions was assessed by plotting ratios of $T_{max\text{-}observed}/T_{max\text{-}predicted}$, $C_{max\text{-}observed}/C_{max\text{-}predicted}$ with the *pI*, lymphatic trunk-LN clearance, and bioavailability (Figure 2.11 S3, Figure 2.12 S4 and Figure 2.13 S5). The bioavailability and *pI* values for mAbs were obtained from the literature (37-50). In the case of anifrolumab, the *pI* value was estimated using the amino acid sequence (51) and ProtParam, a web-based tool (52).

2.3 Results

2.3.1 Estimation of the 2-compartment IV parameters

The 2-compartment model was used to estimate the parameters using the literature PK data after IV bolus or infusion (Table 2.3). These parameters were different for each mAb, and they were fixed in the minimal PBPK model. The mAbs had average volume of 3.5571 L (standard deviation, ± 1.1081) for the central compartment and 1.8069 L (standard deviation, ± 1.0308) for the peripheral compartment. Mean values for CL_{cen}, K_{12} and K_{21} were 0.01531 L/h, 0.0992 /h and 0.3448 /h, respectively.

Table 2.3: The 2-compartmental model parameters for various mAbs after IV administration

mAb	**V_{cen} (L)**	**V_{per} (L)**	**CL_{cen} (L/h)**	**K_{12} (/h)**	**K_{21} (/h)**	**Reference**
Adalimumab	3.2131	2.2382	0.01023	0.01162	0.01669	(53)
Anifrolumab	2.1732	3.7869	0.0111	0.02024	0.01161	(54)
Belimumab	3.0486	2.3877	0.009602	0.01635	0.0208	(43, 44)
Canakinumab	3.2897	2.3638	0.007541	0.009417	0.0131	(40)
Daclizumab	5.5255	1.762	0.01104	0.00257	0.00805	(55)
Golimumab	2.3293	2.3279	0.01467	0.01302	0.01302	(42, 56)
Guselkumab	4.9381	0.4131	0.0233	0.000871	0.0104	(46)
Infliximab	4.5782	1.2645	0.0169	0.8914	3.2276	(57)
Tocilizumab	3.5145	1.0064	0.03585	0.01084	0.0378	(58)
Trastuzumab	2.9608	0.5186	0.01291	0.0157	0.0896	(59, 60)
Mean	3.5571	1.8069	0.01531	0.0992	0.3448	
Standard deviation	1.1081	1.0308	0.00849	0.2784	1.0131	

2.3.2 Estimation of the lymphatic trunk-LN clearance

A single parameter (lymphatic trunk-LN clearance) was estimated and the rest of the model was fixed using literature values as described in the methods section. The clearance represents proteolysis of mAbs in the interstitial space of the lymphatic trunks and LNs (Figure 2.4). The model predicted a total of 37 SC PK profiles (10 mAbs with 26 different doses), which were compared with the mean observed published data (Figure 2.5 and Figure 2.6). However, in the case of belimumab, the patient-PK profile was a geometric mean. The estimated lymphatic trunk-LN clearance was in the range of 0.0001495 to 0.007776 L/h with a mean of 0.00213 L/h (0.001332 to 0.002928, lower and upper 95% confidence intervals of the mean) for a total of 37 SC PK profiles. Average lymphatic trunk-LN clearance values for each mAb are shown in Table 2.4.

Table 2.4: Estimation of lymphatic trunk-LN clearance after SC administration of mAbs

mAb (SC injection site)	**SC Dose and (F)**	**Population**	**Ref.**	**Model estimated average CL_{LN}**
Adalimumab (Lower abdomen)	40 mg (64%)	Healthy volunteers	(39)	0.00192 L/h
Anifrolumab (Abdomen)	300, 600 mg (73%)	Healthy volunteers	(45)	0.00005105 L/h
Belimumab* (Abdomen or thigh)	200, 2*120, 240 mg (76%)	Lupus erythromatosus patients	(43)	0.0002564 L/h
Belimumab (Abdomen or thigh)	200, 2*120, 240 mg (76%)	Healthy volunteers	(44)	0.00000024 L/h
Canakinumab (NA)	150, 300 mg (70 %)	Healthy volunteers	(40)	0.001116 L/h
Daclizumab** (NA)	50, 150, 300 mg	Healthy volunteers	(55)	0.0005207 L/h
Golimumab (Abdomen/Thigh/Upper Arm)	50, 100 mg (50 %)	Healthy volunteers	(41, 42)	0.00651L/h
Guselkumab (NA)	10, 30, 100, 300 mg (49%)	Healthy volunteers	(46, 47)	0.002389 L/h

Infliximab (NA)	100 mg (on day 0, 28 and 56) (71%)	Rheumatoid arthritis patients	(61, 62)	0.0006855 L/h[a]
Tocilizumab (Abdomen)	162 mg (49%)	Healthy volunteers	(58)	0.002085 L/h[a]
Tocilizumab (Thigh)	162 mg (with hyaluronidase)	Healthy volunteers	(63)	0.0006258 L/h[a,b]
Trastuzumab (Thigh)	482, 645, and 776 mg (with hyaluronidase)	Healthy volunteers	(64)	0.001621 L/ h[a,c]
Trastuzumab (Thigh)	895 mg (with hyaluronidase)	HER2-positive breast cancer patients	(64)	0.0004889 L/h[a,d]
Trastuzumab (Thigh)	600 mg (with hyaluronidase)	Healthy volunteers	(65)	0.001839 L/h[a,e]

Mean CL_{LN}: 0.00213 L/h (Standard deviation: 0.002359, lower 95% confidence interval of the mean: 0.001332, upper 95% confidence interval of the mean: 0.002928 L/h)
Nonlinear mixed-effects model with stochastic EM algorithm used for estimation of the parameters unless indicated. All observed SC PK data were mean values unless indicated.
[a]*Nonlinear least squares solver*
[b]*SC Site lymph flow (0.04474 L/h) and CL_{LN} estimated simultaneously*
[c]*SC Site lymph flow (0.002798 L/h) and CL_{LN} estimated simultaneously*
[d]*SC Site lymph flow (0.003112 L/h) and CL_{LN} estimated simultaneously*
[e]*SC Site lymph flow (0.01307 L/h) and CL_{LN} estimated simultaneously*
F: Bioavailability after SC administration
**Geometric mean of the observed pharmacokinetic data*
***The model simulated median pharmacokinetic data*
CL_{LN}: Clearance of mAb in the lymphatic trunk-LN interstitial compartment
NA: Not available

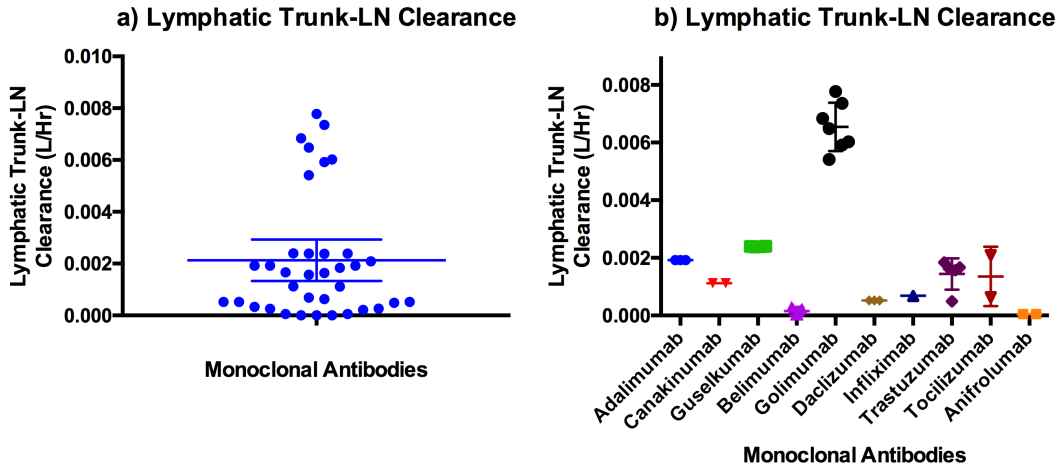

Figure 2.4: Estimated lymphatic trunk-LN clearance for a) all mAbs used in this study, b) individual mAbs (Mean with 95% confidence interval)

2.3.3 Applications of the minimal PBPK model to evaluate impact of hyaluronidase in the mAb formulation

The mAbs for the SC administration are formulated as highly concentrated solutions in order to deliver higher doses (typically 500-900 mg). The injection volume cannot be increased more than 1-2 mL due to injection discomfort (66). However, hyaluronidase has been used in several studies to allow higher injection volumes by disrupting the complex network of the SC extracellular matrix formed by hyaluronic acid. In addition, the hyaluronidase enzyme can increase the rate of TP absorption leading to decreased T_{max}, increased C_{max}, increased area under the curve (AUC), and enhanced bioavailability of the TPs (66, 67). In this study, the SC PK data obtained after co-formulation of hyaluronidase, and tocilizumab and trastuzumab were used to estimate the lymphatic trunk-LN clearance (58, 63-65). Due to the co-formulation with hyaluronidase, T_{max} was over-predicted for tocilizumab and trastuzumab. The *Observed* T_{max}/*Predicted* T_{max} ratio for tocilizumab and trastuzumab was 0.58 and 0.6, respectively. We hypothesized that the alteration of SC injection site by hyaluronidase may lead to altered SC injection site lymph flow. Therefore, lymphatic trunk-LN clearance and SC injection site lymph flow were estimated simultaneously (Table 2.4). After the simultaneous estimation of both the parameters, T_{max} prediction was improved for tocilizumab (*Observed* T_{max}/*Predicted* T_{max}= 0.87). Similarly, trastuzumab T_{max} prediction accuracy was also improved (*Observed* T_{max}/*Predicted* T_{max}= 0.82). The estimated SC injection site lymph flow for the co-formulation of the mAb and hyaluronidase was higher when compared to the original lymph flow used in the model. The estimated SC injection site lymph flow for tocilizumab was 0.04474 L/h, which was 330-fold higher than the minimal PBPK model's value (Table 2.1). In the case of trastuzumab, the average SC injection site lymph flow was

0.002955 L/h (22-fold higher than the original value) for healthy volunteers and HER2-positive breast cancer patients (64) (observed and model estimated PK profiles shown in Figure 2.6). In the case of other SC PK profile (65) (data not shown) obtained from the healthy volunteers, SC site lymph flow was 0.01307 L/h (96-fold higher than the original value).

In addition to above analysis, the SC PK (tocilizumab) profiles obtained without co-formulation with hyaluronidase enzyme were also used for simultaneous estimation of the SC injection site lymph flow and lymphatic trunk-LN clearance using the minimal PBPK model. This was done to demonstrate that the change in the SC site lymph flow observed previously was in fact due to co-formulation of hyaluronidase and mAbs. In the case of tocilizumab without hyaluronidase, the SC site lymph flow was 0.0009557 L/h (only 7-fold higher than the original value). This proves that the SC injection site lymph flow was altered when hyaluronidase co-formulation strategy was used. For the SC profiles where this strategy was not used, the SC injection site lymph flow was relatively less affected.

2.3.4 Comparison of lymphatic trunk-LN clearance with pI and bioavailability of mAbs

The estimated lymphatic trunk-LN clearance was compared with the *pI* (Figure 2.7) and bioavailability (Figure 2.8) of mAbs. The interstitial space has overall anionic charge due to cell surface of various immune cells in the LNs. The mAbs with higher *pI* had higher values of the estimated lymphatic trunk-LN clearance. The lymphatic trunk-LN clearance increased with decrease in bioavailability (obtained from literature) of the mAbs (Figure 2.8). This suggests that the model accounted for the lymphatic proteolysis of mAbs after SC administration. This may indicate that the lymphatic system was an important organ for clearance of mAbs.

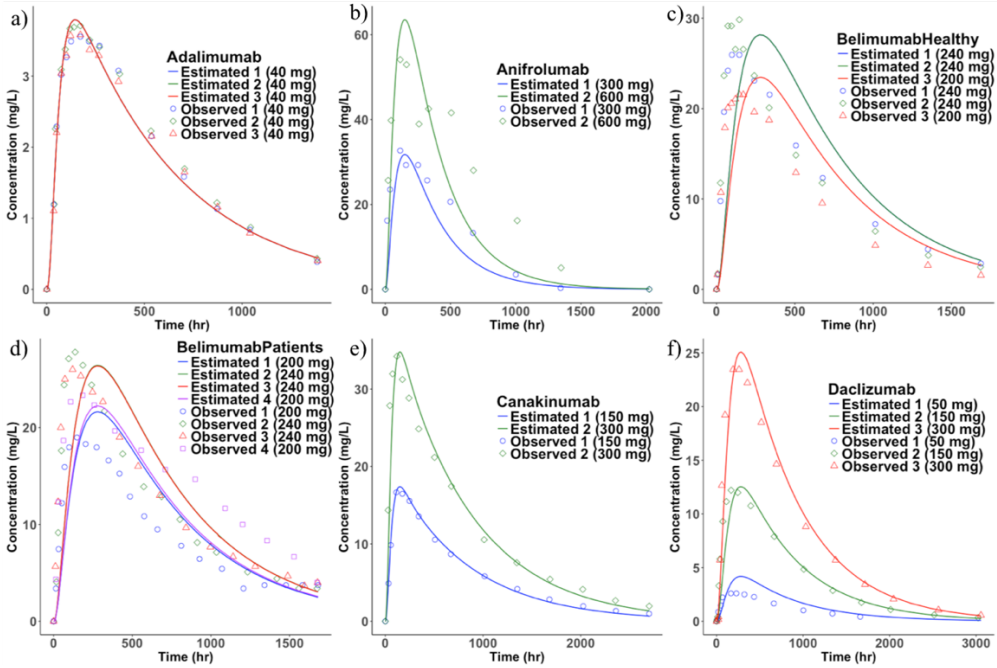

Figure 2.5: Observed and the model fitted SC PK profiles. a) adalimumab, b) anifrolumab, c) belimumab-Healthy, d) belimumab-patients, e) canakinumab, and f) daclizumab (Mean observed PK profiles were used for comparison with the model estimates. Observed belimumab

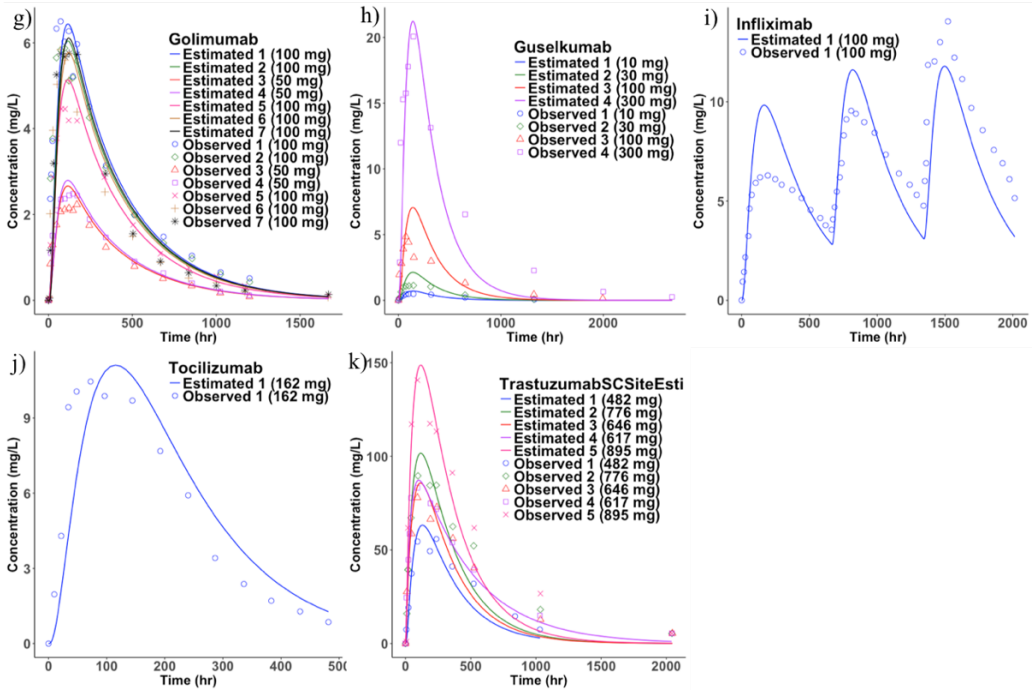

Figure 2.6: Observed and the model fitted SC PK profiles. g) golimumab, h) guselkumab, i) infliximab, j) tocilizumab, and k) trastuzumab (Mean observed PK profiles were used for comparison with the model estimates)

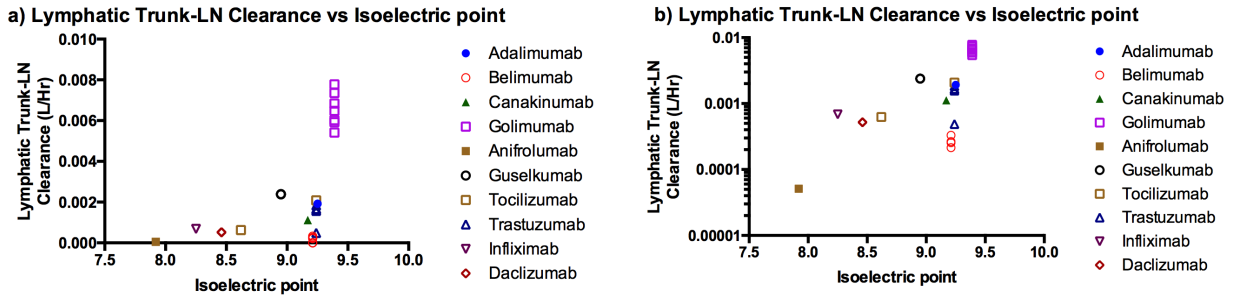

Figure 2.7: Correlation of the model estimated lymphatic trunk-LN clearance with the isoelectric point a) Linear scale, b) Logarithmic scale

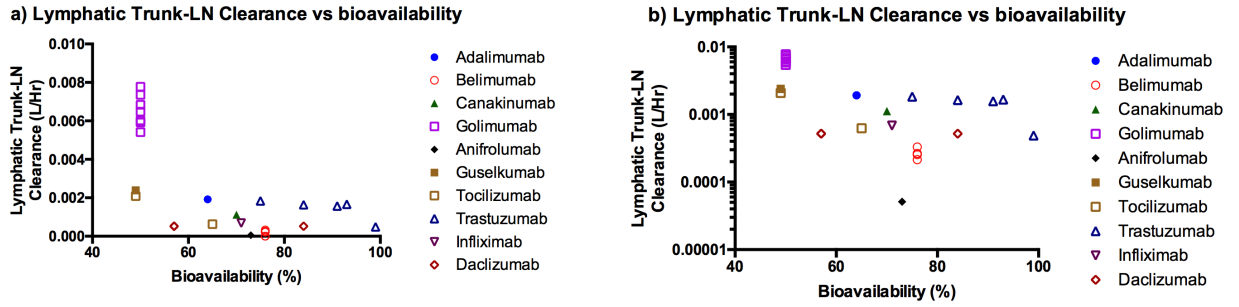

Figure 2.8: Correlation of the model estimated lymphatic trunk-LN clearance with the bioavailability a) Linear scale, b) Logarithmic scale (Trastuzumab: Co-formulated with hyaluronidase. Tocilizumab: Only one sample co-formulated with hyaluronidase.)

2.3.5 Sensitivity analysis

The sensitivity analysis showed that the SC injection site interstitial volume (V_{SC}^{I}), SC lymph flow (L_{SC}), and lymphatic capillary volume (V^{LCap}), and afferent lymph flow (L_{Aff}) were responsible for changes in C_{max} and T_{max} of mAbs (Figure 2.9 S1). In the case of lymphatic trunk-LN interstitial volume (V_{LY}^{I}), increases of the volume by 50- and 100-fold lead to alterations of mAb PK profiles, while changes by 0.1 to 10-fold of the original value did not alter C_{max} or T_{max}. The alteration of lymphatic trunk-LN clearance (CL_{LN}) and efferent lymph flow (L_{Eff}) mainly

lead to modification of the C_{max}. In addition, changes in the thoracic duct lymph flow (L_{Thor}) and central lymphatic volume (V_{LY-Cen}) did not impact PK of mAbs. This indicates that transit through the initial lymphatic system after SC injection is the rate determining step for mAb absorption instead of the thoracic duct. Therefore, SC injection site volume, SC injection site lymph flow, lymphatic capillary volume, afferent lymph flow, and efferent lymph flow are important physiological parameters for absorption of mAbs. Change in the thoracic duct lymph flow and central lymphatic volume did not alter the PK of mAbs (Figure 2.9 S1). Both the C_{max} and T_{max} were sensitive to change in the SC injection site volume, SC injection site lymph flow, lymphatic capillary volume, and afferent lymph flow (Figure 2.11 S3 to Figure 2.15 S7). However, changes in the efferent lymph flow had no impact on T_{max}. In addition, when the lymphatic reflection coefficient was increased; C_{max} decreased, while T_{max} increased. There was no change in the PK profile after alteration of the vascular reflection coefficient (Figure 2.10 S2).

2.3.6 Model validation

Accuracy of the model prediction was evaluated by plotting observed and predicted values of C_{max} and T_{max} (Figure 2.8 S8). In addition, the ratio of observed and predicted C_{max} and T_{max} were plotted with the *pI*, lymphatic trunk-LN clearance, and bioavailability (Figure 2.17 S9, Figure 2.18 S10, and Figure 2.19 S11). In the case of C_{max}, all predicted values were within 1.2-to 0.5-fold of the observed literature values. The predicted T_{max} was within the range of 1.8 to 0.3-fold of the observed values.

2.4 Discussion

In this manuscript, the sequential transfer of mAbs after SC administration via the lymphatic system is described using the minimal PBPK model. The SC injection site (interstitial, endosomal, vascular), lymphatic capillaries, lymphatic trunk-LNs (interstitial and endosomal), central lymphatic system (thoracic duct and cisterna chyli) compartments were used to describe the transit of mAbs after SC administration. The rest of the body was modeled with a 2-compartment model based on the literature IV PK data. The sequential transfer was based on the known anatomy of lymphatic system (24-27). However, detailed routes of TP transfer via different LNs remain to be investigated further. Also, some individuals may have alterations in the clearance patterns, for example the clearance in the arm, shoulder and thigh may be significantly changed after radical mastoidectomy. In addition, an injection site may clear into multiple adjacent lymph basins.

The clearance from the interstitial space of the SC injection site was not considered in the model, because a previously reported study indicated that protein (hGH) degradation was minimal at the SC injection site (5). In addition, simultaneous estimation of the clearance from the SC interstitial space and lymphatic trunk-LN interstitial compartment resulted in a minor contribution for the SC injection site proteolysis (data not shown). However, the endosomal proteolysis in the SC injection site and LNs was considered. The lymphatic trunk-LN interstitial clearance was estimated using the minimal PBPK model and the literature SC PK data (Figure 2.4 and Table 2.4). The estimated clearance differed with dosing and population changes. This alteration of the estimated clearance may be due to disease condition, change in formulation, or the differences in posttranslational modifications (e.g. glycosylation). These differences were not considered in the model. The model demonstrated that the estimated lymphatic trunk-LN clearance of mAbs may correlate with the bioavailability (Figure 2.8). The estimated clearance increased when the

bioavailability of the mAb decreased. This indicates efficiency of the model to account for the proteolysis of mAbs in the lymphatic system. According to the previously published reports, proteolysis was not observed after incubation of TPs with the freshly collected lymph, indicating absence of any protease enzymes in the lymph (5, 68). In this study, the lymphatic trunk volume (which mainly contains lymph fluid) and the LN (which mainly contains lymph node cells) volume were combined to represent the compartment responsible for proteolysis of the mAbs. The lymphatic trunk-LN compartment was mainly composed of the LN volume. The lymphatic trunk volume representing volume of the lymph fluid was very minor (< 7%).

Sensitivity analysis (Figure 2.9 S1) showed that the lymphatic trunk-LN interstitial space proteolysis was important to govern C_{max} of the mAbs. The degradation of mAbs in the lymphatic system was primarily due to extracellular or interstitial proteolysis. The protease enzymes secreted by the LN and other immune cells in the interstitial space may play an important role in reducing the bioavailability of mAbs. Intracellular or endosomal proteolysis of mAbs was negligible due to FcRn binding-mediated protection. The intracellular proteolysis of mAbs in the lymphatic system may be dependent on their uptake by the lymphocytes. In this model, we used endosomal uptake rate (R1) from a literature PBPK model (estimated by fitting liver data) (3, 4). Alteration of the endosomal uptake rate by 0.1 to 100-fold of the original value did not change the PK of mAbs (data not shown). However, *in vitro* studies to calculate R1 may be useful for an accurate understanding of proteolytic processes in the SC injection site and lymphatic system. Disease conditions like inflammation may also increase proteolytic activity of the lymph. However, this remains to be further investigated. In addition, alteration of the recycling fraction of FcRn bound mAb, dissociation constant for antibody FcRn binding, and FcRn concentration did not change PK of mAbs (data not shown).

Wang et al. (68) confirmed proteolysis of erythropoietin in the presence of rat LN cell suspension. The protein completely disappeared after the number of LN cells in the incubation was increased. This indicates that LNs are responsible for proteolysis of TPs. In addition, after incubation of the protein with the SC tissue homogenate, 90-95% of the parent protein remained unaffected (68). Although the authors raised doubts about loss of proteolytic activity during preparation of the SC tissue homogenate, this finding corroborates our conclusion that the SC site degradation plays a minor role in governing the bioavailability. However, in another study, insulin was reported to degrade at the SC injection site (69). Detailed investigation of *in vitro* proteolysis of mAbs in various systems must be done to arrive at more definite conclusion about the cause of reduced bioavailability after SC administration.

The PK studies in humans indicate that variation in the injection site (abdomen and thigh) do not have any impact on C_{max} and $AUC_{0-\infty}$ of belimumab (44). In another clinical study, golimumab's median T_{max} after SC injection in the thigh was 1.25-fold higher than SC injection in the abdomen and upper arm. The C_{max} after thigh SC injection was 1.33-fold higher than SC injection in the upper arm, and the C_{max}-abdomen was 1.24-fold higher than that of the upper arm (42). This suggests that the volumes of lymphatic compartments and lymph flows may not be significantly different for each of the SC injection sites. Therefore, lymphatic volumes and flows rates for one injection site may be applied to the other. The calculations used in the model showed that the interstitial volume of the lymphatic trunk-LN was similar for various SC injection sites (upper arm, abdomen, and thigh) (Table 2.1).

The prediction accuracy of the model was determined by plotting observed and predicted PK parameters (Figure 2.16 S8). There was no correlation of the prediction accuracy of T_{max} or C_{max} with the *pI* or bioavailability or the estimated lymphatic trunk-LN clearance of mAbs. This

confirms that the *pI* of mAbs did not affect the uptake by lymphatic system. Similarly, lymphatic trunk-LN clearance and bioavailability did not govern the prediction accuracy of the model.

The model also showed that for the mAbs with higher *pI*, the estimated lymphatic trunk-LN clearance was greater. The cationic proteins with higher *pI* have a propensity to bind with the anionic cell surfaces and interstitial space (e.g. hyaluronic acid). Higher *pI* also leads to faster clearance of mAbs (70). Similar trend was observed for the mAbs investigated in this study (Figure 2.7). This correlation may be used to predict the lymphatic trunk-LN clearance based on the known *pI* of mAbs. The lymphatic clearance can be used in the minimal PBPK model to predict SC PK of the mAbs.

Sensitivity analysis of the model parameters indicate that the initial lymphatics are rate determining for absorption of mAbs via the SC route. Mainly, the SC injection site lymph flow, SC injection site volume, afferent lymph flow, efferent lymph flow, and lymphatic trunk-LN volume impacted T_{max}, after their alteration by 0.1 to 100-fold of the original value. However, thoracic duct lymph flow had no effect on T_{max} even after 0.1 to 100-fold changes in its value. Therefore, alteration of thoracic lymph duct flows due to disease condition may not alter overall PK of mAbs. However, the parameters associated with the initial lymphatic system are important to govern the absorption of mAbs and change in those parameters due to the disease conditions may significantly alter the SC PK of mAbs.

It was reported earlier that the PK of mAbs is prone to high inter-subject variability. Factors like body weight, age, sex, ethnicity, disease condition, immune status are responsible for variations in the PK (71). However, more research is needed to evaluate their influence on physiological parameters related to the SC injection site and lymphatic system. The minimal PBPK model may be used for prediction of bioavailability of mAbs using *in vitro* lymphatic proteolysis

data and to evaluate the impact of changes in lymphatic flow rates on the PK. In addition, the model may be utilized to guide *in vitro* experiments for mechanistic prediction of the bioavailability. This study has explained various physiological parameters related to the SC injection site and lymphatic system responsible for regulating the PK of mAbs.

2.5 Conclusion

The lymphatic trunk-LN clearance was estimated using the minimal PBPK model. The physiological parameters related to the SC tissue and lymphatic system were used along with the 2-compartment IV parameters to construct the minimal PBPK model for prediction of SC PK of the mAbs. The model may serve as a platform to utilize the *in vitro* clearance data from the SC tissue and lymphatic system to predict SC PK of mAbs. The LNs were mainly responsible for proteolysis of mAbs leading to their reduced bioavailability. Therefore, LN cell suspension may be used to generate inputs for the PBPK model. However, the *in vitro* studies were beyond the scope of this manuscript. Further, this study identified SC injection site lymph flow, afferent lymph flow, efferent lymph flow, volumes associated with the SC injection site, and lymphatic trunk-LN clearance as important parameters responsible for absorption of mAbs. The lymphatic trunk-LN clearance increased with increase in the *pI* of mAbs. Therefore, the *pI* of mAbs can be used to calculate the lymphatic clearance. Overall, the model is useful to understand disposition of mAbs after SC administration.

2.6 Supplementary Data

The raw digitalized data of the Figures in this chapter and the SimBiology (Matlab 2017a) model file are archived and available free of charge at the University of Kansas ScholarWorks Repository (https://kuscholarworks.ku.edu/handle/1808/26648).

Model equations

$$V_{SC}^{I}\left(\frac{dC_{SC}^{I}}{dt}\right) = \left((1-\sigma_V)\times L_{SC}\times C_{SC}^{V}\right) - (R1\times C_{SC}^{I}) + \left((1-FR)\times R2\times(1-f_{uSC})\times C_{SC}^{E}\right) - \left((1-\sigma_L)\times L_{SC}\times C_{SC}^{I}\right)$$

$$V_{SC}^{V}\left(\frac{dC_{SC}^{V}}{dt}\right) = -\left((1-\sigma_V)\times L_{SC}\times C_{SC}^{V}\right) - \left((Q_{SC}-L_{SC})\times C_{SC}^{V}\right) + (FR\times R2\times(1-f_{uSC})\times C_{SC}^{E}) - \left(R1\times C_{SC}^{V}\right) + (Q_{SC}\times C_{Cen})$$

$$V_{SC}^{E}\left(\frac{dC_{SC}^{E}}{dt}\right) = (R1\times C_{SC}^{I}) - (FR\times R2\times(1-f_{uSC})\times C_{SC}^{E}) - \left((1-FR)\times R2\times(1-f_{uSC})\times C_{SC}^{E}\right) + \left(R1\times C_{SC}^{V}\right) - ((1-f_{uSC})\times CL_{Endo-SC}\times C_{SC}^{E})$$

$$V^{LCap}\left(\frac{dC^{LCap}}{dt}\right) = \left((1-\sigma_L)\times L_{SC}\times C^{LCap}\right) - \left(L_{Aff}\times C^{LCap}\right)$$

$$V_{LN}^{I}\left(\frac{dC_{LN}^{I}}{dt}\right) = \left(L_{Aff}\times C_{LN}^{Cap}\right) - \left(L_{Eff}\times C_{LN}^{I}\right) - (CL_{LN}\times C_{LN}^{I}) - (R1\times C_{LN}^{I}) + \left((1-FR)\times R2\times(1-f_{uLN})\times C_{LN}^{E}\right)$$

$$V_{LN}^{E}\left(\frac{dC_{LN}^{E}}{dt}\right) = (R1\times C_{LN}^{I}) - \left((1-FR)\times R2\times(1-f_{uLN})\times C_{LN}^{E}\right) - ((1-f_{uLN})\times CL_{Endo-LN}\times C_{LN}^{E})$$

$$V_{LN-Cen}\left(\frac{dC_{LN-Cen}}{dt}\right) = -(L_{Thor}\times C_{LN-Cen}) + \left(L_{Eff}\times C_{LN}^{I}\right)$$

$$V_{Cen}\left(\frac{dC_{Cen}}{dt}\right) = (L_{Thor}\times C_{LN-Cen}) + ((Q_{SC}-L_{SC})\times C_{SC}^{V}) - (CL_{Cen}\times C_{Cen}) - (K_{12}\times C_{Cen}) + (K_{21}\times C_{Per}) - (Q_{SC}\times C_{Cen})$$

$$V_{Per}\left(\frac{dC_{Per}}{dt}\right) = (K_{12}\times C_{Cen}) - (K_{21}\times C_{Per})$$

$$f_{uSC} = 1 - \left(\frac{1}{2\times(C_{Endo} + C_{SC}^{E})}\right) \times \left((K_d + nPt + C_{Endo} + C_{SC}^{E}) - \left(\sqrt{(Kd + nPt + C_{Endo} + C_{SC}^{E})^2 - (4\times(C_{Endo} + C_{SC}^{E})\times nPt)}\right)\right)$$

$$f_{uLN} = 1 - \left(\frac{1}{2\times(C_{Endo} + C_{LN}^{E})}\right) \times \left((K_d + nPt + C_{Endo} + C_{LN}^{E}) - \left(\sqrt{(Kd + nPt + C_{Endo} + C_{LN}^{E})^2 - (4\times(C_{Endo} + C_{LN}^{E})\times nPt)}\right)\right)$$

Glossary

Parameter	Definition
C_{SC}^{V}	Concentration of mAb in the vascular space of SC injection site
C_{SC}^{I}	Concentration of mAb in the interstitial space of SC injection site
C_{SC}^{E}	Concentration of mAb in the endosomal space of SC injection site
C^{LCap}	Concentration of mAb in the lymphatic capillary compartment
C_{LN}^{I}	Concentration of mAb in the interstitial space of lymphatic trunk-LNs
C_{LN}^{E}	Concentration of mAb in the endosomal space of lymphatic trunk-LNs
C_{LY-Cen}	Concentration of mAb in the central lymphatic system
C_{Cen}	Concentration of mAb in the central compartment
C_{Per}	Concentration of mAb in the peripheral compartment
V_{SC}^{I}	SC injection site interstitial volume
V_{SC}^{V}	SC injection site vascular volume
V_{SC}^{E}	SC injection site endosomal volume
V^{LCap}	Volume of the lymphatic capillaries
V_{LN}^{I}	Combined interstitial volume of lymphatic trunk-LNs after SC injection in thigh
V_{LN}^{E}	Combined endosomal volume of all LNs to which the mAb is exposed after SC injection in thigh
V_{LY-Cen}	Volume of central lymphatic system
V_{Cen}	Volume of the central compartment
V_{Per}	Volume of the peripheral compartment
L_{SC}	Lymph flow at the SC injection site

L_{Aff}	Lymph flow afferent to LNs
L_{Eff}	Lymph flow efferent to LNs
L_{Thor}	Thoracic duct lymph flow
Q_{SC}	Blood flow at the SC injection site
σ_L	Lymphatic reflection coefficient
σ_V	Vascular reflection coefficient
CL_{LN}	Clearance of mAb in the lymphatic trunk-LN interstitial compartment
$CL_{Endo-SC}$	Endosomal clearance of mAb in the SC injection site
$CL_{Endo-LN}$	Endosomal clearance of mAb in LNs
CL_{Cen}	Clearance of mAb from the central compartment
K_{12}	Transfer rate constant from the central compartment to the peripheral compartment
K_{21}	Transfer rate constant from the peripheral compartment to the central compartment
f_{uSC}	Unbound fraction of mAb in SC tissue
f_{uLN}	Unbound fraction of mAb in lymphatic trunk and LNs
C_{Endo}	Concentration of endogenous mAb in endosomal compartment
$R1$	Endosomal uptake rate of antibody
$R2$	Endosomal return rate of antibody
FR	Recycling fraction of FcRn bound mAb
Kd	Dissociation constant for antibody FcRn binding
nPt	*FcRn concentration in SC tissue or LN*

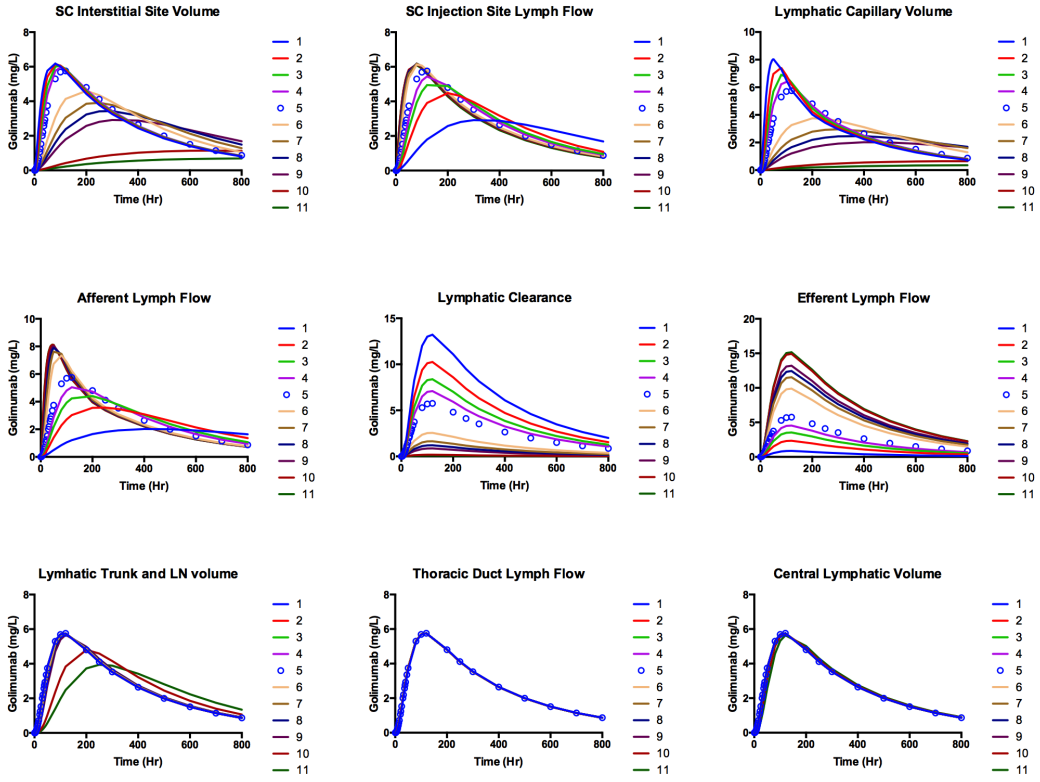

Figure 2.9 S1: Effect of change in various model parameters on pharmacokinetics of mAbs.
(PK profiles 1-11 in each diagram represent 0.1-, 0.3-, 0.5-, 0.7-, 1-, 3-, 5-, 7-, 10-, 50-, and 100-fold of the original parameter value as mentioned in the Table 1. The pharmacokinetic profile '5' (circles) represents the original parameter value. In the case of lymphatic clearance, estimated lymphatic clearance of golimumab was used as an original value (Table 4))

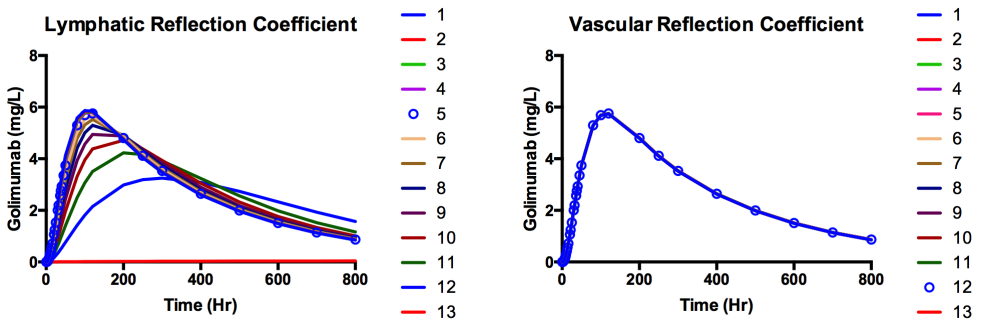

Figure 2.10 S2: Effect of change in lymphatic reflection coefficient and vascular reflection coefficient on PK of mAbs.
(The lymphatic reflection coefficient was altered by 0.1-, 0.3-, 0.5-, 0.7-, 1-, 1.5-, 2-, 2.5-, 3-, 3.5-, 4-, 4.5-, 5-folds of the original parameter value as mentioned in Table 2. The vascular reflection coefficient was altered by 0.01-, 0.1-, 0.105-, 0.21-, 0.31-, 0.42-, 0.52-, 0.63-, 0.73-, 0.84-, 0.94-, 1-, 1.05-folds of the original parameter value as mentioned in Table 2. The pharmacokinetic profiles from 1 to 13 indicate increasing value of the parameters.)

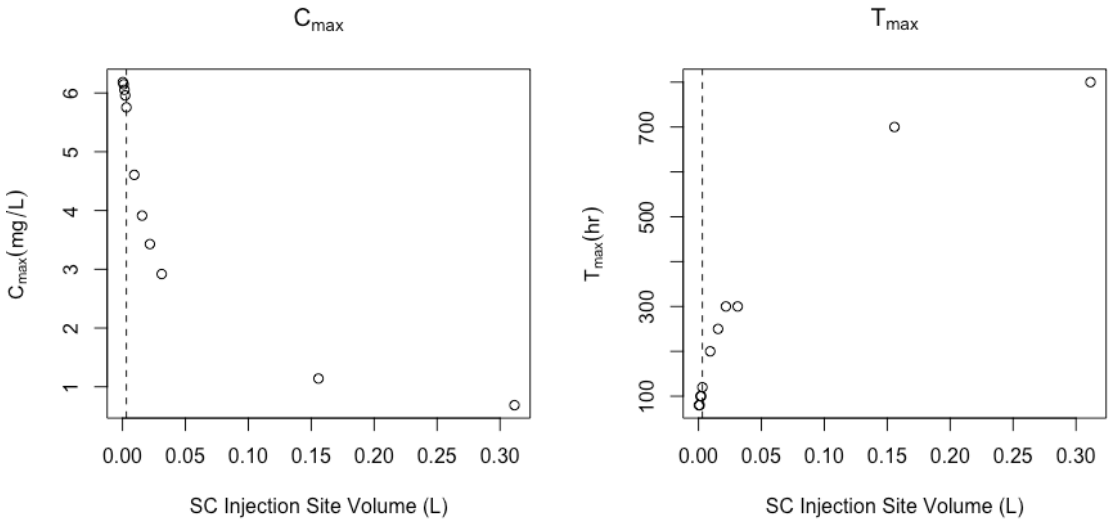

Figure 2.11 S3: C_{max} and T_{max} values with alteration of SC injection site volume.
The volume was altered by 0.1-, 0.3-, 0.5-, 0.7-, 1-, 3-, 5-, 7-, 10-, 50-, and 100-fold of the original parameter value as mentioned in Table 1.
(Dashed line indicates the original value of the SC injection site volume used in the model)

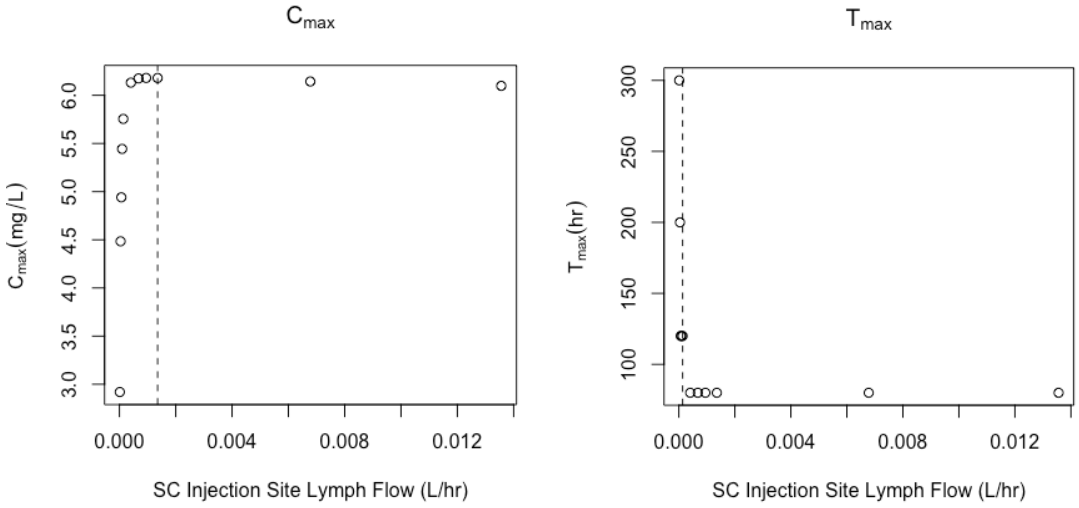

Figure 2.12 S4: C_{max} and T_{max} values with alteration of SC injection site lymph flow.
The lymph flow was altered by 0.1-, 0.3-, 0.5-, 0.7-, 1-, 3-, 5-, 7-, 10-, 50-, and 100-fold of the original parameter value as mentioned in Table 1. (Dashed line indicates the original value of the SC injection site lymph flow used in the model)

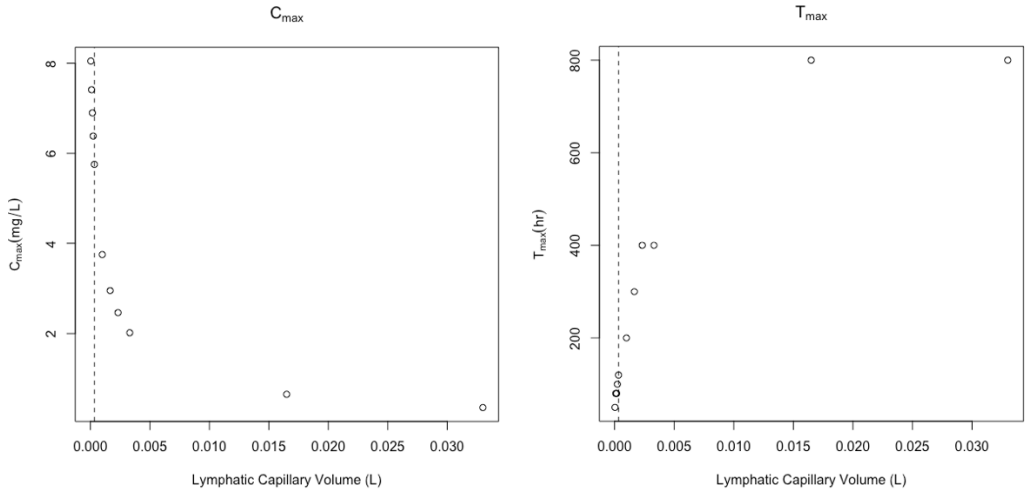

Figure 2.13 S5: C_{max} and T_{max} values with alteration of lymphatic capillary volume
The volume was altered by 0.1-, 0.3-, 0.5-, 0.7-, 1-, 3-, 5-, 7-, 10-, 50-, and 100-fold of the original parameter value as mentioned in Table 1. (Dashed line indicates the original value of the lymphatic capillary volume used in the model)

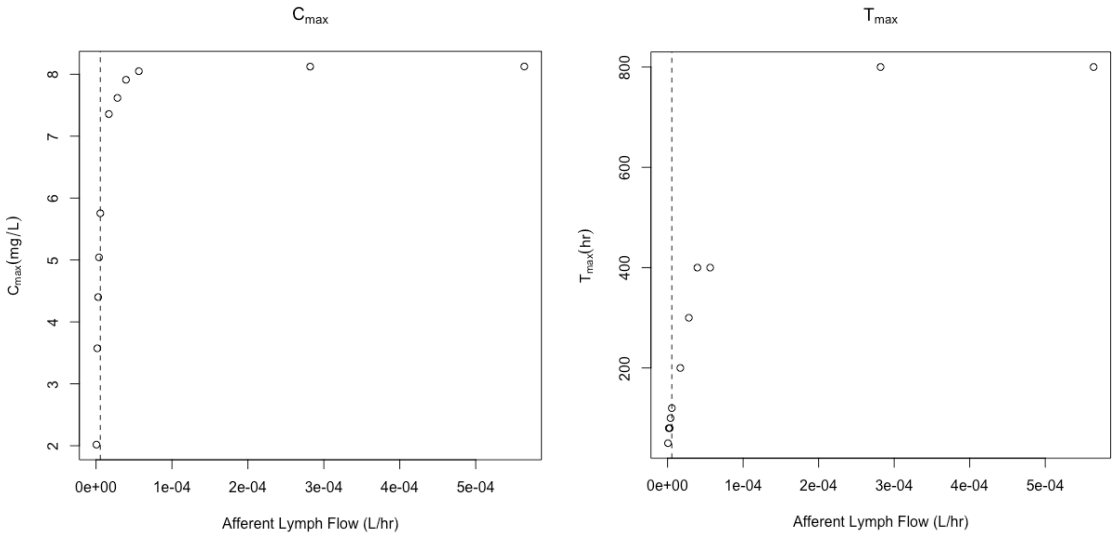

Figure 2.14 S6: C_{max} and T_{max} values with alteration of afferent lymph flow
The lymph flow was altered by 0.1-, 0.3-, 0.5-, 0.7-, 1-, 3-, 5-, 7-, 10-, 50-, and 100-fold of the original parameter value as mentioned in Table 1. (Dashed line indicates the original value of the afferent lymph flow used in the model)

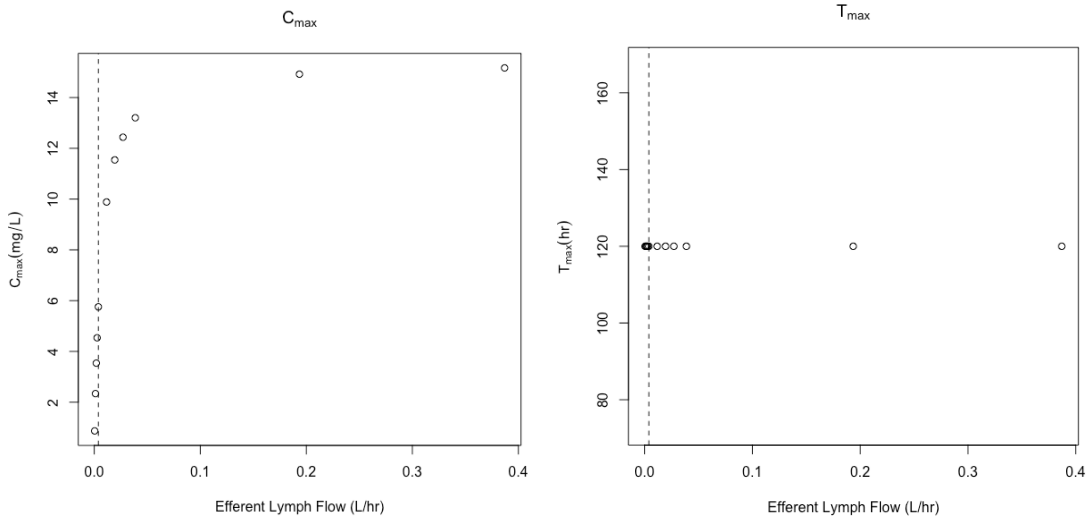

Figure 2.15 S7: C_{max} and T_{max} values with alteration of efferent lymph flow
The lymph flow was altered by 0.1-, 0.3-, 0.5-, 0.7-, 1-, 3-, 5-, 7-, 10-, 50-, and 100-fold of the original parameter value as mentioned in Table 1. (Dashed line indicates the original value of the efferent lymph flow used in the model)

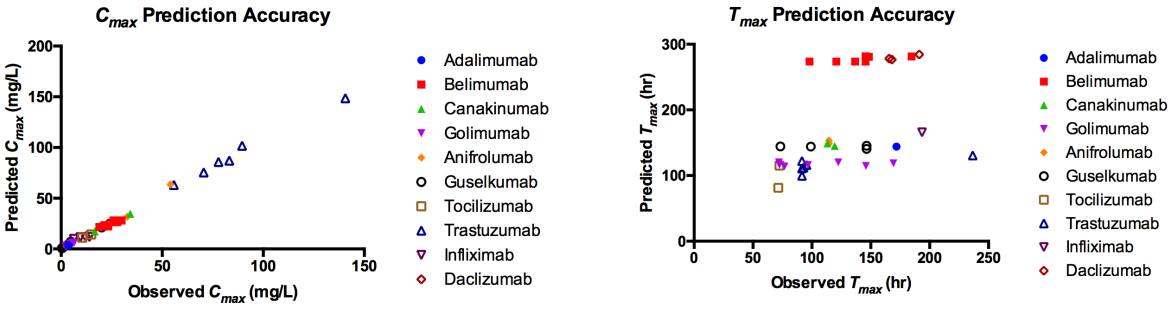

Figure 2.16 S8: Accuracy of C_{max} and T_{max} prediction by the minimal PBPK model

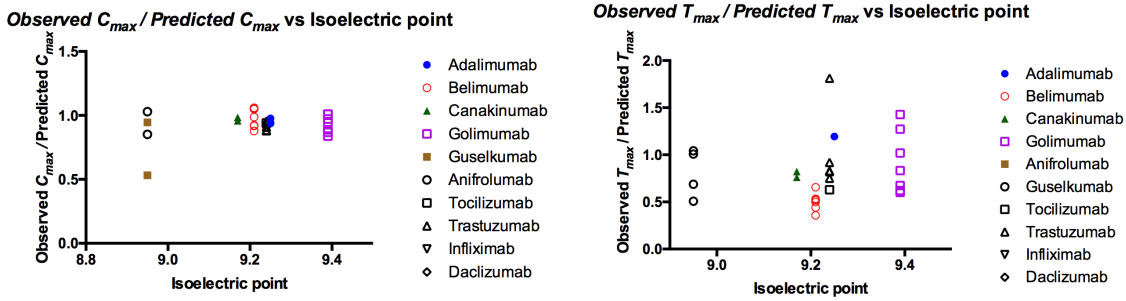

Figure 2.17 S9: Accuracy of the predicted C_{max} and T_{max} in comparison with the isoelectric point of mAbs

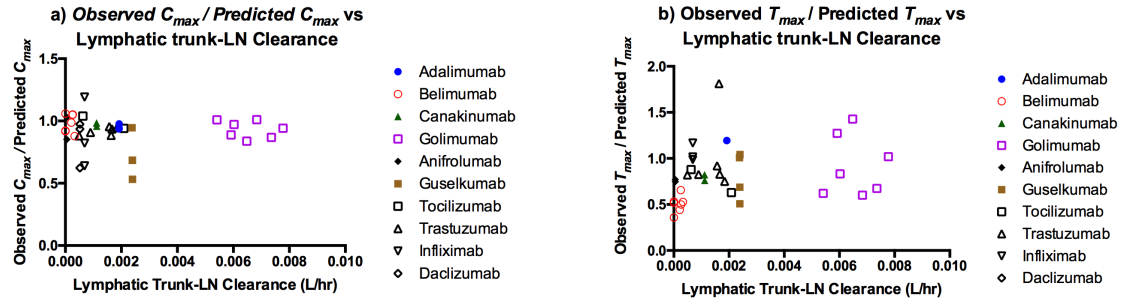

Figure 2.18 S10: Accuracy of the predicted C_{max} and T_{max} in comparison with the estimated lymphatic trunk-LN clearance of mAbs

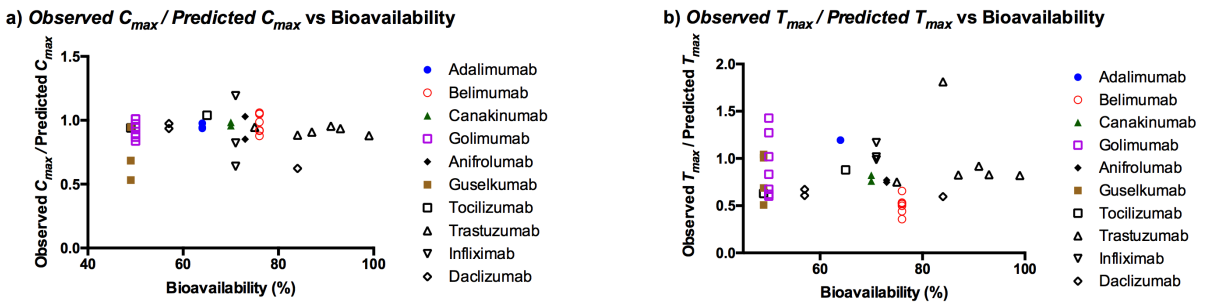

Figure 2.19 S11: Accuracy of the predicted C_{max} and T_{max} in comparison with the bioavailability of mAbs

2.7 References

1. Jackisch C, Müller V, Maintz C, Hell S, Ataseven B. Subcutaneous administration of monoclonal antibodies in oncology. Geburtshilfe Frauenheilkd. 2014;74(4):343
2. Dirks NL, Meibohm B. Population pharmacokinetics of therapeutic monoclonal antibodies. Clin Pharmacokinet. 2010;49(10):633-659
3. Zhao L, Ji P, Li Z, Roy P, Sahajwalla CG. The antibody drug absorption following subcutaneous or intramuscular administration and its mathematical description by coupling physiologically based absorption process with the conventional compartment pharmacokinetic model. J Clin Pharmacol. 2013;53(3):314-325
4. Davda JP, Jain M, Batra SK, Gwilt PR, Robinson DH. A physiologically based pharmacokinetic (PBPK) model to characterize and predict the disposition of monoclonal antibody CC49 and its single chain Fv constructs. Int Immunopharmacol. 2008;8(3):401-413
5. Charman SA, Segrave AM, Edwards GA, Porter CJ. Systemic availability and lymphatic transport of human growth hormone administered by subcutaneous injection. J Pharm Sci. 2000;89(2):168-177
6. Abuqayyas L, Balthasar JP. Application of PBPK modeling to predict monoclonal antibody disposition in plasma and tissues in mouse models of human colorectal cancer. J Pharmacokinet Pharmacodyn. 2012;39(6):683-710
7. Baxter LT, Zhu H, Mackensen DG, Butler WF, Jain RK. Biodistribution of monoclonal antibodies: scale-up from mouse to human using a physiologically based pharmacokinetic model. Cancer Res. 1995;55(20):4611-4622
8. Shah DK, Betts AM. Towards a platform PBPK model to characterize the plasma and tissue disposition of monoclonal antibodies in preclinical species and human. J Pharmacokinet Pharmacodyn. 2012;39(1):67-86
9. Gill KL, Gardner I, Li L, Jamei M. A bottom-up whole-body physiologically based pharmacokinetic model to mechanistically predict tissue distribution and the rate of subcutaneous absorption of therapeutic proteins. AAPS J. 2016;18(1):156-170
10. Chen X, DuBois DC, Almon RR, Jusko WJ. Interrelationships between Infliximab and rhTNF-α in Plasma using Minimal Physiologically-Based Pharmacokinetic (mPBPK) Models. Drug Metab Dispos. 2017;45(7):790-797

11. Elmeliegy M, Lowe P, Krzyzanski W. Simplification of complex physiologically based pharmacokinetic models of monoclonal antibodies. AAPS J. 2014;16(4):810-842
12. Li L, Gardner I, Dostalek M, Jamei M. Simulation of Monoclonal Antibody Pharmacokinetics in HumansUsing a Minimal Physiologically Based Model. AAPS J. 2014;16(5):1097-1109
13. Sager JE, Yu J, Raguenau-Majlessi I, Isoherranen N. Physiologically based pharmacokinetic (PBPK) modeling and simulation approaches: a systematic review of published models, applications and model verification. Drug Metab Dispos. 2015;43:1823-1837
14. Wong H, Chow TW. Physiologically based pharmacokinetic modeling of therapeutic proteins. J Pharm Sci. 2017;106(9):2270-2275
15. Rohatgi A. WebPlotDigitizer, Web based tool to extract data from plots, images, and maps. 2018 Accessed on May 09, 2018. Available from: https://automeris.io/WebPlotDigitizer/.
16. Kuo I, Akpa BS. Validity of the Lipid Sink as a Mechanism for the Reversal of Local Anesthetic Systemic ToxicityA Physiologically Based Pharmacokinetic Model Study. Anesthesiology. 2013;118(6):1350-1361
17. Garg A, Balthasar JP. Physiologically-based pharmacokinetic (PBPK) model to predict IgG tissue kinetics in wild-type and FcRn-knockout mice. J Pharmacokinet Pharmacodyn. 2007;34(5):687-709
18. Mellor R, Stanton A, Azarbod P, Sherman M, Levick J, Mortimer P. Enhanced cutaneous lymphatic network in the forearms of women with postmastectomy oedema. J Vasc Res. 2000;37(6):501-512
19. Nathanson SD, Nelson L, Karvelis KC. Rates of flow of technetium 99m-labeled human serum albumin from peripheral injection sites to sentinel lymph nodes. Ann Surg Oncol. 1996;3(4):329-335
20. Margaris K, Black RA. Modelling the lymphatic system: challenges and opportunities. J R Soc Interface. 2012;9(69):601-612
21. Fischer M, Franzeck UK, Herrig I, Costanzo U, Wen S, Schiesser M, Hoffmann U, Bollinger A. Flow velocity of single lymphatic capillaries in human skin. Am J Physiol Heart Circ Physiol. 1996;270(1):H358-H363
22. Fujiwara M, Sawada M, Kasuya A, Matsushita Y, Yamada M, Fukamizu H, Magata Y, Tokura Y, Sakahara H. Measurement of cutaneous lymphatic flow rates in patients with skin cancer: area extraction method. J Dermatol. 2014;41(6):498-504
23. Quin J, Shannon A. The influence of the lymph node on the protein concentration of efferent lymph leaving the node. J Physiol. 1977;264(2):307-321
24. Lymphatics of the Upper Limb. Department of Neurobiology and Developmental Sciences, University of Arkansas for Medical Sciences. Accessed on April 14, 2018. Available from: http://anatomy.uams.edu/lymph_upperlimb.html.
25. Bontumasi N, Jacobson JA, Caoili E, Brandon C, Kim SM, Jamadar D. Inguinal lymph nodes: size, number, and other characteristics in asymptomatic patients by CT. Surg Radiol Anat. 2014;36(10):1051-1055
26. Usovich A, Borziak E. Variants in the number and size and the topography of the lumbar lymph nodes in the regional of the liver in the human adult. Arkh Anat Gistol Ehmbriol. 1982;83(7):29-33

27. Ying M, Pang B. Three-dimensional ultrasound measurement of cervical lymph node volume. Br J Radiol. 2009;82(980):617-625
28. Corlier F, Rivals I, Lagarde J, Hamelin L, Corne H, Dauphinot L, Ando K, Cossec J, Fontaine G, Dorothée G. Modifications of the endosomal compartment in peripheral blood mononuclear cells and fibroblasts from Alzheimer's disease patients. Transl Psychiatry. 2015;5(7):e595
29. Sikorski E, Gerberick G, Ryan C, Miller C, Ridder G. Phenotypic analysis of lymphocyte subpopulations in lymph nodes draining the ear following exposure to contact allergens and irritants. Fundam Appl Toxicol. 1996;34(1):25-35
30. Skandalakis JE, Skandalakis LJ, Skandalakis PN. Anatomy of the lymphatics. Surg Oncol Clin N Am. 2007;16(1):1-16
31. Lymphatics of the Lower Limb. Department of Neurobiology and Developmental Sciences, University of Arkansas for Medical Sciences. Accessed on April 14, 2018. Available from: http://anatomy.uams.edu/lymph_lowerlimb.html.
32. Lymphatics of the Abdomen. Department of Neurobiology and Developmental Sciences, University of Arkansas for Medical Sciences. Accessed on April 14, 2018. Available from: http://anatomy.uams.edu/lymph_abdomen.html.
33. Giragossian C, Vage C, Li J, Pelletier K, Piché-Nicholas N, Rajadhyaksha M, Liras J, Logan A, Calle RA, Weng Y. Mechanistic Investigation of the Preclinical Pharmacokinetics and Interspecies Scaling of PF-05231023, a Fibroblast Growth Factor 21–Antibody Protein Conjugate. Drug Metab Dispos. 2015;43(6):803-811
34. Dumont AE, Mulholland JH. Flow rate and composition of thoracic-duct lymph in patients with cirrhosis. N Engl J Med. 1960;263(10):471-474
35. Zhou J, Johnson JE, Ghetie V, Ober RJ, Ward ES. Generation of mutated variants of the human form of the MHC class I-related receptor, FcRn, with increased affinity for mouse immunoglobulin G. J Mol Biol. 2003;332(4):901-913
36. Ferl GZ, Wu AM, DiStefano JJ. A predictive model of therapeutic monoclonal antibody dynamics and regulation by the neonatal Fc receptor (FcRn). Ann Biomed Eng. 2005;33(11):1640-1652
37. Center for drug evaluation and research, guselkumab application 761061Orig1s000 2018 Accessed on April 13, 2018. Available from: https://www.accessdata.fda.gov/drugsatfda_docs/nda/2017/761061Orig1s000OtherR.pdf.
38. Doyle Keith, Halo Maria, Harding Emma R, Lewis Peter, Uden Mark, Damian Valeriu, Xuan H. Antibody variants. In.; 2017.
39. Hillson J, Mant T, Rosano M, Huntenburg C, Alai-Safar M, Darne S, Palmer D, Pavlova BG, Doralt J, Reeve R. Pharmacokinetic equivalence, comparable safety, and immunogenicity of an adalimumab biosimilar product (M923) to Humira in healthy subjects. Pharmacol Res Perspect. 2018;6(1)
40. Chakraborty A, Tannenbaum S, Rordorf C, Lowe PJ, Floch D, Gram H, Roy S. Pharmacokinetic and pharmacodynamic properties of canakinumab, a human anti-interleukin-1β monoclonal antibody. Clin Pharmacokinet. 2012;51(6):e1-e18
41. Ling J, Lyn S, Xu Z, Achira M, Bouman-Thio E, Shishido A, Ford J, Shankar G, Wagner C, Kim KT. Lack of racial differences in the pharmacokinetics of subcutaneous golimumab in healthy Japanese and Caucasian male subjects. J Clin Pharmacol. 2010;50(7):792-802

42. Xu Z, Wang Q, Zhuang Y, Frederick B, Yan H, Bouman-Thio E, Marini JC, Keen M, Snead D, Davis HM. Subcutaneous bioavailability of golimumab at 3 different injection sites in healthy subjects. J Clin Pharmacol. 2010;50(3):276-284
43. Yapa SWS, Roth D, Gordon D, Struemper H. Comparison of intravenous and subcutaneous exposure supporting dose selection of subcutaneous belimumab systemic lupus erythematosus Phase 3 program. Lupus. 2016;25(13):1448-1455
44. Cai WW, Fiscella M, Chen C, Zhong ZJ, Freimuth WW, Subich DC. Bioavailability, pharmacokinetics, and safety of belimumab administered subcutaneously in healthy subjects. Clin Pharmacol Drug Dev. 2013;2(4):349-357
45. Tummala R, Rouse T, Berglind A, Santiago L. Safety, tolerability, and pharmacokinetics of subcutaneous and intravenous anifrolumab in healthy volunteers. In.ACR/ARHP Annual Meeting: BMJ Publishing Group Ltd; 2017.
46. Zhuang Y, Calderon C, Marciniak SJ, Bouman-Thio E, Szapary P, Yang T-Y, Schantz A, Davis HM, Zhou H, Xu Z. First-in-human study to assess guselkumab (anti-IL-23 mAb) pharmacokinetics/safety in healthy subjects and patients with moderate-to-severe psoriasis. Eur J Clin Pharmacol. 2016;72(11):1303-1310
47. Product monograph for Tremfya (guselkumab). Janssen Inc. . Accessed on April 16, 2018. Available from: http://www.janssen.com/canada/sites/www_janssen_com_canada/files/prod_files/live/tremfya_cpm.pdf.
48. Infliximab DrugBank. 2018 Accessed on May 17, 2018. Available from: https://www.drugbank.ca/drugs/DB00065.
49. Daclizumab DrugBank. 2018 Accessed on May 17, 2018. Available from: https://www.drugbank.ca/drugs/DB00111.
50. Miao S, Fan L, Zhao L, Ding D, Liu X, Wang H, Tan W-S. Physicochemical and Biological Characterization of the Proposed Biosimilar Tocilizumab. Biomed Res Int. 2017;2017
51. International Nonproprietary Names for Pharmaceutical Substances (INN), WHO Drug Information, Vol. 28, No. 1, 2014 (INN List 71). Accessed on May 25, 2018. Available from: http://www.who.int/medicines/publications/druginformation/innlists/RL71.pdf.
52. Gasteiger E, Hoogland C, Gattiker A, Wilkins MR, Appel RD, Bairoch A. Protein identification and analysis tools on the ExPASy server. In. The proteomics protocols handbook: Springer; 2005. p. 571-607.
53. Weisman MH, Moreland LW, Furst DE, Weinblatt ME, Keystone EC, Paulus HE, Teoh LS, Velagapudi RB, Noertersheuser PA, Granneman GR. Efficacy, pharmacokinetic, and safety assessment of adalimumab, a fully human anti-tumor necrosis factor-alpha monoclonal antibody, in adults with rheumatoid arthritis receiving concomitant methotrexate: a pilot study. Clin Ther. 2003;25(6):1700-1721
54. Goldberg A, Geppert T, Schiopu E, Frech T, Hsu V, Simms RW, Peng SL, Yao Y, Elgeioushi N, Chang L. Dose-escalation of human anti-interferon-α receptor monoclonal antibody MEDI-546 in subjects with systemic sclerosis: a phase 1, multicenter, open label study. Arthritis Res Ther. 2014;16(1):R57
55. Othman AA, Tran JQ, Tang MT, Dutta S. Population pharmacokinetics of daclizumab high-yield process in healthy volunteers: integrated analysis of intravenous and subcutaneous, single-and multiple-dose administration. Clin Pharmacokinet. 2014;53(10):907-918

56. Zhou H, Jang H, Fleischmann RM, Bouman-Thio E, Xu Z, Marini JC, Pendley C, Jiao Q, Shankar G, Marciniak SJ. Pharmacokinetics and safety of golimumab, a fully human anti-TNF-α monoclonal antibody, in subjects with rheumatoid arthritis. J Clin Pharmacol. 2007;47(3):383-396
57. Palaparthy R, Udata C, Hua SY, Yin D, Cai C-H, Salts S, Rehman MI, McClellan J, Meng X. A randomized study comparing the pharmacokinetics of the potential biosimilar PF-06438179/GP1111 with Remicade®(infliximab) in healthy subjects (REFLECTIONS B537-01). Expert Rev Clin Immunol. 2018;14(4):329-336
58. Zhang X, Georgy A, Rowell L. Pharmacokinetics and pharmacodynamics of tocilizumab, a humanized anti-interleukin-6 receptor monoclonal antibody, following single-dose administration by subcutaneous and intravenous routes to healthy subjects. Int J Clin Pharmacol Ther. 2013;51(6):443-455
59. Morita J, Tanaka M, Nomoto M, Matsuki S, Tsuru T, Matsuguma K, Shiramoto M. Pharmacokinetic bioequivalence, safety, and immunogenicity of DMB-3111, a trastuzumab biosimilar, and trastuzumab in healthy Japanese adult males: results of a randomized trial. BioDrugs. 2016;30(1):17-25
60. Pivot X, Deslypere JP, Park LS, Kim MJ, Lee W, Lee J. A Randomized Phase I Study Comparing the Pharmacokinetics of HD201, a Trastuzumab Biosimilar, With European Union–sourced Herceptin. Clin Ther. 2018;40(3):396-405. e394
61. Westhovens R, Houssiau F, Joly J, Everitt DE, Zhu Y, Sisco D, Van Hartingsveldt B, Mascelli MA, Graham MA, Durez P. A phase I study assessing the safety, clinical response, and pharmacokinetics of an experimental infliximab formulation for subcutaneous or intramuscular administration in patients with rheumatoid arthritis. J Rheumatol. 2006;33(5):847-853
62. Zhu Y, Pendley C, Sisco D, Westhovens R, Durez P, Bouman-Thio E, Hartingsveldt B, Everitt D, Graham M. Pharmacokinetics and pharmacodynamics of infliximab, an anti-tumor necrosis factor-alpha monoclonal antibody, following single subcutaneous administrations in rheumatoid arthritis patients. Clin Pharmacol Ther. 2005;77(2)
63. Morcos PN, Zhang X, McIntyre C, Bittner B, Rowell L, Hussain Z. Pharmacokinetics and pharmacodynamics of single subcutaneous doses of tocilizumab administered with or without rHuPH20. Int J Clin Pharmacol Ther. 2013;51(7):537-548
64. Wynne C, Harvey V, Schwabe C, Waaka D, McIntyre C, Bittner B. Comparison of Subcutaneous and Intravenous Administration of Trastuzumab: A Phase I/Ib Trial in Healthy Male Volunteers and Patients With HER2-Positive Breast Cancer. J Clin Pharmacol. 2013;53(2):192-201
65. Wynne CJ, Ellis-Pegler RB, Waaka DS, Schwabe C, Lehle M, Heinzmann D, Mangat R, Li C, Dick AE, Cranshaw NA. Comparative pharmacokinetics of subcutaneous trastuzumab administered via handheld syringe or proprietary single-use injection device in healthy males. Cancer Chemother Pharmacol. 2013;72(5):1079-1087
66. Richter WF, Jacobsen B. Subcutaneous Absorption of Biotherapeutics: Knowns and Unknowns. Drug Metab Dispos. 2014;42(11):1881-1889
67. Liu S, Xie B, Wei W, Hui M, Su Z. Design and preparation of chimeric hyaluronidase as a chaperone for the subcutaneous administration of biopharmaceuticals. Biochem Eng J. 2016;112:32-41

68. Wang W, Chen N, Shen X, Cunningham P, Fauty S, Michel K, Wang B, Hong X, Adreani C, Nunes CN. Lymphatic transport and catabolism of therapeutic proteins after subcutaneous administration to rats and dogs. Drug Metab Dispos. 2012;40(5):952-962
69. Okumura K, Komada F, Hori R. Fate of porcine and human insulin at the subcutaneous injection site. I. degradation and absorption of insulins in the rat. J Pharmacobiodyn. 1985;8(1):25-32
70. Bumbaca D, Boswell CA, Fielder PJ, Khawli LA. Physiochemical and biochemical factors influencing the pharmacokinetics of antibody therapeutics. AAPS J. 2012;14(3):554-558
71. Gill KL, Machavaram KK, Rose RH, Chetty M. Potential sources of inter-subject variability in monoclonal antibody pharmacokinetics. Clin Pharmacokinet. 2016;55(7):789-805

Chapter 3 : Effect of iron oxide nanoparticles on the secondary structure and oxidation of rat growth hormone

3.1 Introduction

The higher order structure (secondary, tertiary, quaternary) of TPs is important for their biological activity and stability. Chemical changes including oxidation of susceptible amino acids can lead to alteration in the secondary structure of TPs, resulting in increased aggregation, altered pharmacokinetics, lower biological activity and increased immunogenicity (1). For example, bioavailability may be reduced leading to a need to increase the dose or alteration in the therapy due to generation of antibodies against the TP (1, 2).

The trace metal impurities arising from buffers, formulation components, and processing equipment, can oxidize TPs by catalyzing formation of reactive oxygen species (ROS). Soluble iron impurities can generate superoxide radicals, hydrogen peroxide (H_2O_2), and hydroxyl radicals leading to oxidation of TPs (3, 4). In addition, iron oxide nanoparticles (IONPs) may be present due to iron containing equipment used during the manufacturing process or produced by injection needles during TP administration. A protein corona can develop around nanoparticles (NPs) leading to formation of larger particle sizes and possibly aggregation (5). Protein-NP interactions may induce changes in protein secondary structure (6) and further oxidation of TPs (7). It is not known, however, if altered secondary structure of TPs due to binding to IONPs can influence the extent of TP oxidation. We therefore selected rat growth hormone (rGH) as a model protein for studying oxidation, since it is a very similar analogue to the TP human growth hormone, and is suitable for future *in vivo* immunogenicity studies (8).

3.2 Experimental

3.2.1 Materials

The IONPs (γ-form) were purchased from US Research Nanomaterials Inc (Houston, TX). The 2,2′-azobis (2-methylpropionamidine) dihydrochloride (AAPH), H_2O_2, potassium ferricyanide, 1,10-phenanthroline monohydrate, sodium citrate tribasic dihydrate, and ascorbic acid were purchased from Sigma Aldrich (St. Louise, MO). Ammonium bicarbonate, dithiothreitol, iodoacetamide, LC/MS-grade water (0.1% v/v formic acid), acetonitrile (0.1% v/v formic acid), monobasic sodium dihydrogen phosphate, sulfuric acid, hydrogen fluoride, dibasic sodium hydrogen phosphate, and the Pierce BCA protein assay kit (Product number: 23227) were purchased from Fisher Scientific (Waltham, MA). Trypsin/Lys-C (mass spectrometry grade) was purchased from Promega (Madison, WI). Amicon ultra-0.5 centrifugal filter devices (10, 30, 100 kDa cut off membranes) were purchased from Millipore Inc., (Bedford, MA, USA). The 4-aminomethyl-benzylsulfonic acid (ABS) was synthesized according to a published method (9, 10).

3.2.2 Production of rat growth hormone (rGH)

rGH is a 22-kDa protein of 191 amino acids and contains two disulfide bonds (11, 12). The cDNA plasmid for the rGH protein sequence (Protein accession number- AAI66872) was synthesized by GenScript (New Jersey, USA) and inserted into pET-28a(+) using the NdeI and BamHI restriction sites (13). The pre-protein sequence (first 25 amino acids) was removed from the original cDNA; the resulting rGH amino acid sequence is shown in the Figure 3.9 S1. The plasmid was transformed into DH5α competent E. coli cells, and a single colony was expanded, mini-prepped, and the sequence confirmed by KanPro Research Inc. (Lawrence, KS).

The confirmed rGH plasmid was transformed into BL21 (DE3) E. coli, and rGH was produced by shake flask culture using a protocol modified from previously reported methods (12, 14, 15). In brief, the *E. coli* cells were cultured in lysogeny broth (LB) media with kanamycin (40 μg/mL) and chloramphenicol (40 μg/mL) at 37 °C and 200 rpm shaking. Once an optical density (at 600 nm) of around 0.6 was reached, cultures were induced with isopropyl β-d-1-thiogalactopyranoside (IPTG) (1.0 mM). After 4 h, cultures were centrifuged at 1391×g for 10 min and the cell pellet was suspended in lysis buffer (50 mM Tris-hydrochloride, 500 mM sodium chloride, pH 8). The mixture was then sonicated (50% power, 4 cycles × 30 sec, at 4 °C) until it was no longer viscous using a Fisher Scientific Sonic Dismembrator Model 500 (Waltham, MA). Inclusion bodies of rGH were isolated by centrifuging at 6,000×g (at 4 °C) for 30 min, followed by a water wash, and then dissolved in 6 M urea lysis buffer. The proteins were refolded by following proprietary procedures (KanPro Research Inc.), and then dialyzed in phosphate buffer saline (PBS), containing 88 mM mannitol. rGH was analyzed for purity using SDS-PAGE (Figure 3.10). Intact mass analysis of the protein confirmed the molecular weight of 21.9 kDa and also showed around 15% initial oxidation (+16 m/z) on two methionine residues (M1 and/or M5). This modification probably occurred during purification and refolding (data not shown). Detailed analysis of a tryptic digest of the protein (sequence coverage of ~92%) using mass spectrometry was previously reported (14).

3.2.3 Chemical Oxidation of rGH and sample processing

Chemically accelerated oxidation of rGH was induced with H_2O_2 or AAPH, in the absence or presence of IONPs. The final concentrations of rGH, H_2O_2, AAPH and IONPs were 0.8 mg/mL, 2 mM, 10 mM and 1.7 mM, respectively. This mixture was incubated at 37 °C for 3 or 24 h while

shaking at 100 revolutions/minute. For H_2O_2-induced oxidation, 10 μL of catalase solution (1 mg/mL) were added to quench the oxidation. AAPH was removed using Amicon ultra-0.5 centrifugal filters (10 kDa). The oxidized rGH was processed further for reduction of disulfide bonds using dithiothreitol and alkylation of cysteine residues using iodoacetamide to prevent reformation of disulfide bonds. The disulfide bonds are reduced to increase efficiency of tryptic digestion by disrupting secondary structure of the protein. The disulfide bonds of rGH were reduced by adding 100 μL of dithiothreitol (26 mM stock solution in 50 mM ammonium bicarbonate buffer) and incubating this mixture at 45 °C for 1 h. The reduced cysteine residues were alkylated by adding 200 μL of IAA (50 mM stock solution in 50 mM ammonium bicarbonate buffer) and incubating at 37 °C for 1 h.

3.2.4 Trypsin/Lys-C digestion of rGH

The reduced and alkylated rGH (0.4 mg) was precipitated with 700 μL of 0.5 M perchloric acid. The samples were centrifuged at 15000×g for 15 min and the resulting pellet was suspended in 400 μL of 50 mM ammonium bicarbonate buffer (pH 7.5). Four μg of trypsin/Lys-C were added and the samples were incubated at 37 °C overnight. The proteolytic digests were centrifuged using 10 kDa centrifuge filters to remove trace amounts of undigested rGH and trypsin/Lyc-C. The tryptic peptides were stored at -20 °C until mass spectrometry analysis.

3.2.5 Mass spectrometry

A nanoAcquity UPLC (Waters Corporation, Milford, MA) connected to a Xevo Q-TOF (Waters Corporation, UK) was used for for LC-ESI-MS experiments. Tryptic peptides were first trapped on an UPLC Symmetry C18 nanoAcquity trap column (5 μm, 180 μm × 20 mm, Water

Corporation) and then separated on an UPLC Peptide CSH C18 nanoAcquity column (1.7 μm, 75 μm × 250 mm, Waters Corporation). For separation, we applied an optimized method and parameters that we previously reported (9). *In silico* tryptic digestions of rGH and prediction of fragment ions were performed with web based applications, Proteomics Toolkit (Institute of Systems Biology, Seattle, WA) and ProteinProspector 5.21.2 (The University of California, San Francisco, CA).

3.2.6 Fluorogenic derivatization

Tyrosine residues of rGH were oxidized with AAPH in the absence or presence of IONPs. The oxidation products were derivatized with ABS to produce a fluorescent benzoxazole according to our previously described protocol (9, 16). Briefly, rGH oxidized by AAPH was buffer exchanged with 100 mM sodium phosphate buffer (pH 9) using 10-kDa cutoff filter devices. Potassium ferricyanide and rGH and were mixed in a molar ratio of 30:1. ABS (10 mM) was added, and the mixture incubated at ambient temperature in the dark for 90 min. Fluorescence (360 nm-excitation/ 490 nm-emission) was measured using a SpectraMax GeminiXS microplate fluorometer (Molecular Devices, Sunnyvale, CA).

3.2.7 Fourier transform infrared (FTIR)

Spectra of rGH solutions (1 mg/mL) with varying concentrations of IONP (0.42 to 1.47 mM) were acquired with a Bruker Tensor 27 FTIR spectrometer fitted with a Bio-ATR cell (Bruker, Billerika, MA). Scans were recorded from 600 to 4000 cm^{-1} at a resolution of 1 cm^{-1}. The FTIR spectra were acquired after 10 and 30 min as well as 1 and 2 h incubation period at ambient temperature. In addition, rGH and rGH-IONP mixtures were incubated at increasing temperatures from 15 to 85 °C at increments of 2.5 °C/step with a 120 s equilibration time, and 128 scans/step.

The phosphate buffer-IONP-mixture was used for background subtraction of the FTIR spectra. Opus 6.5 (Bruker, Billerika, MA) was used for baseline and atmospheric correction, generation of second derivative spectra and smoothing.

3.2.8 Circular Dichroism (CD) spectroscopy

Far-ultraviolet (UV) CD spectra were acquired using a Chirascan spectropolarimeter (Applied Photophysics, Surrey, United Kingdom). The final concentration of rGH was 13 μM and the path-length for CD measurements was 0.2 cm. The spectra were acquired from 200 nm to 260 nm with increasing temperature from 10 to 90 °C at increments of 2.5 °C. The secondary structures were estimated from the CD spectra using the BeStSel web tool (17).

3.2.9 Measurement of iron content in IONPs

The iron content of the IONP was determined with a 1,10-phenanthroline colorimetric assay (18-20). The 10% IONP-water dispersion was diluted 5-fold and centrifuged at 500×g for 30 min. The pellet of IONPs was discarded and the supernatant was used for further analysis. Dynamic light scattering (Zetasizer Helix, Malvern Instruments Ltd., Malvern, UK) was used to measure particle size of the supernatant IONPs (~20 nm, 99.2% by number analysis, standard deviation of 3.8 nm) suspended in phosphate buffer (pH 7.4). The supernatant IONPs (1 mL) were treated with 0.5 ml of 8 N sulfuric acid (H_2SO_4), 0.4 ml of 15% w/v ascorbic acid solution, and 0.2 mL of 48% hydrogen fluoride (HF) at 70 °C for 1 h. Ascorbic acid was used as a reducing agent to convert Fe^{+3} to Fe^{+2} ions, so only Fe^{+2} ions would be available to form a colored complex after addition of 1,10-phenanthroline (0.5 ml, 100 mM). After incubating at 40 °C for 25 min, the reaction was quenched with 1 mL of 5% w/v boric acid, and then incubated at ambient temperature

for a further 30 min. Samples were then diluted 20-fold with sodium citrate tribasic dihydrate buffer (10% w/v). Absorbance measurements at 510 nm were acquired with a SpectraMax Plus Microplate Spectrophotometer (Molecular Devices, Sunnyvale, CA), using a calibration curve of known Fe^{+2} concentrations. Fe^{+2} content was assayed in the same manner without the ascorbic acid reduction step. No color developed in any samples (data not shown), indicating that the IONPs did not have a significant Fe^{+2} content and were composed predominantly of Fe^{+3}.

3.2.10 Statistical analysis

ChemoSpec (R package) was used in RStudio (Version 1.1.383) (Boston, MA) to perform principle component analysis (PCA) on FTIR (21). Analysis of variance (ANOVA) and Tukey's multiple comparison test were used to compare the degree of oxidation measured using the mass spectrometry and ABS derivatization technique. ANOVA and Tukey's test were performed using GraphPad Prism 6 (La Jolla, CA).

3.3 Results

3.3.1 Identification of oxidized residues

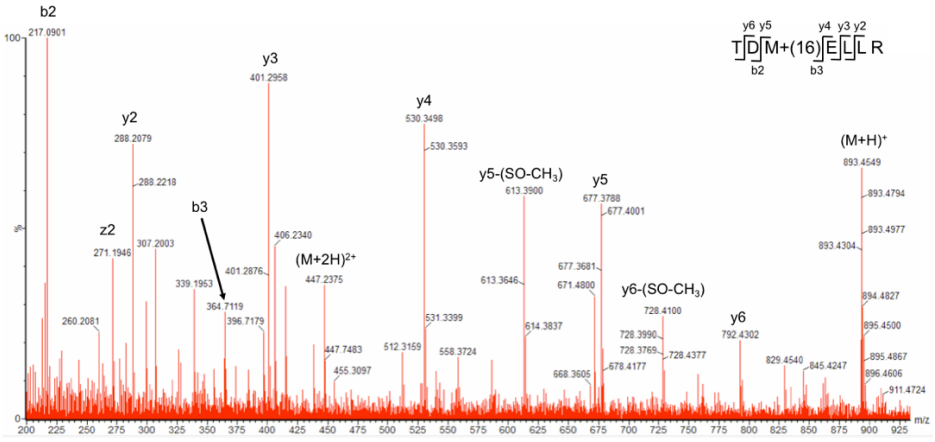

Figure 3.1: Collision-induced dissociation (CID) of the oxidized peptide TDM(+16)ELLR obtained using LC-ESI-MS

In this study, H_2O_2 and AAPH were used to induce the chemical oxidation of rGH. Tryptic digestions were used to monitor the oxidation of methionine residues (Table 3.1). The MS/MS spectrum (Figure 3.1) of tryptic peptide TDMELLR shows that the M73 represents an oxidation target. The fragment ions y5, y6 and b3 indicate an increase in mass of 16 Da. In addition, a characteristic loss (22) of methanesulfenic acid (CH_3SOH, 64 Da) from the y5 ion was observed. This further confirmed the oxidation of methionine (M73) to methionine sulfoxide in the tryptic peptide TDM(+16)ELLR. Other methionine-containing peptides, DLEEGIQALMQELEDGSPR, IFTNSLMFGTSDR and MFPAMPLSSLFANAVLR, also showed oxidation of the methionine amino acids. The MS/MS spectra for these tryptic peptides are described in the Figure 3.11 S3, Figure 3.12 S4, Figure 3.13 S5, Figure 3.14 S6, Figure 3.15 S7 and Figure 3.16 S8, and the results are summarized in Table 3.1.

Table 3.1: Oxidized residues and the associated tryptic peptides

Oxidized residue	**Tryptic peptide**
M1, M5, F2	MFPAMPLSSLFANAVLR
M73	TDMELLR
M102	IFTNSLMFGTSDR
M124	DLEEGIQALMQELEDGSPR
M149	FDANMR

The *y11* and *y13* ions indicated that M124 was oxidized on the tryptic peptide DLEEGIQALM(+16)QELEDGSPR (Figure 3.11 S3). In the case of tryptic peptide IFTNSLMFGTSDR; *y7*, *y8*, *y9*, *y10* and *y11* ion fragments were increased by 16 Da (Figure 3.12 S4). Therefore, M102 was oxidized to methionine sulfoxide in the tryptic peptide IFTNSLM(+16)FGTSDR.

Similarly, 2 peaks of oxidized tryptic peptide MFPAMPLSSLFANAVLR were observed in the chromatogram (data not shown) with the same m/z. CID of the first peak (Figure 3.13 S5) showed that either M1 or F2 were oxidized, because the fragment ions *b2*, *b3*, *b4*, *b5* and *b6*

showed an increase in mass by 16 Da. The fragment ion which could distinguish oxidation specifically on M1 or F2 was not found. While in the case of the second peak of tryptic peptide MFPAM(+16)PLSSLFANAVLR, which eluted earlier, we concluded that the M5 amino acid was oxidized because the *y13* and *b5* fragment ions increased in mass by 16 Da (Figure 3.14 S6).

The tryptic peptide MFPAMPLSSLFANAVLR was oxidized at both the M1/F2 and M5 amino acids. This can be shown by the increase in mass by 32 Da for the *b5* fragment ion (Figure 3.15 S7). The other fragment ions (*y13*, *y15*, *b4*) were increased in mass by 16 Da, indicating oxidation of M1/MF2 and M5.

In the case of tryptic peptide FDANMR, oxidation of M149 was confirmed using the MS/MS fragmentation pattern (Figure 3.16 S8). Oxidation of M149 can be shown by the increase in mass of the *y4* and *y5* fragment ions by +16 Da. Furthermore, a characteristic loss of methanesulfenic acid (CH_3SOH, 64 Da) from the *y4* and *y5* ions was observed. These fragments confirmed that FDANM(+16)R was oxidized at the M149 residue. However, this oxidized tryptic peptide co-eluted with the native non-oxidized FDANMR. Hence the fragmentation pattern had several fragment ions which originated from the native peptide, and they were not assigned.

3.3.2 Quantification of oxidized residues in the presence of IONPs

Out of the 7 methionine (M) residues (Table 3.1) found in rGH, 6 residues (M1, M5, M73, M102, M124, and M149) were monitored for oxidation in the presence of IONPs and H_2O_2. The peptide containing M179 was not found in the mass spectrometric analysis. According to the in silico tryptic digestion, M179 is part of a small 4 amino acid peptide. We hypothesize that this peptide was poorly retained on the trap column and therefore not detected.

The oxidation of M73 was significantly reduced ($P \leq 0.01$) after 24 h of incubation in the presence of H_2O_2 and IONPs compared to H_2O_2 alone (Figure 3.2). After 3-h incubation of rGH with IONPs and H_2O_2, however, M73 showed more oxidation ($P \leq 0.001$) than to H_2O_2 alone. In addition, M73 oxidation was significantly reduced ($P \leq 0.001$) in the presence of IONPs compared to the samples with H_2O_2 alone. The MFPAMPLSSLFANAVLR peptide was also di-oxidized (M1/F2 and M5) by H_2O_2 (Figure 3.17 S9). Similarly, IONPs suppressed oxidation of M102 and M124. In contrast, no difference in oxidation in the presence and absence of IONPs was observed for the peptide M149. The results indicate that the IONPs suppressed H_2O_2-induced oxidation of the tryptic peptides.

After incubation with AAPH, M1, M5, and M149 were either not oxidized or much less oxidized compared to incubation with H_2O_2. However, in the case of M73, M102 and M124, similar results were observed as shown previously with H_2O_2-induced oxidation (Figure 3.18 S10). Overall, IONPs reduced AAPH-induced oxidation of rGH.

3.3.3 AAPH-induced rGH oxidation in the presence of IONPs and use of fluorogenic derivatization for analysis

The tyrosine residues (7 total) in rGH were oxidized by AAPH in the presence and absence of IONPs. The degree of oxidation was monitored using a fluorogenic derivatization method (Figure 3.3). Tyrosine oxidation was reduced in the presence of IONPs. Control groups such as buffer-IONPs, buffer, buffer-IONPs-AAPH were also studied (Figure 3.19 S11). These controls confirmed that IONPs did not have any negative or positive impact on the fluorescence signal used in the assay for quantitation.

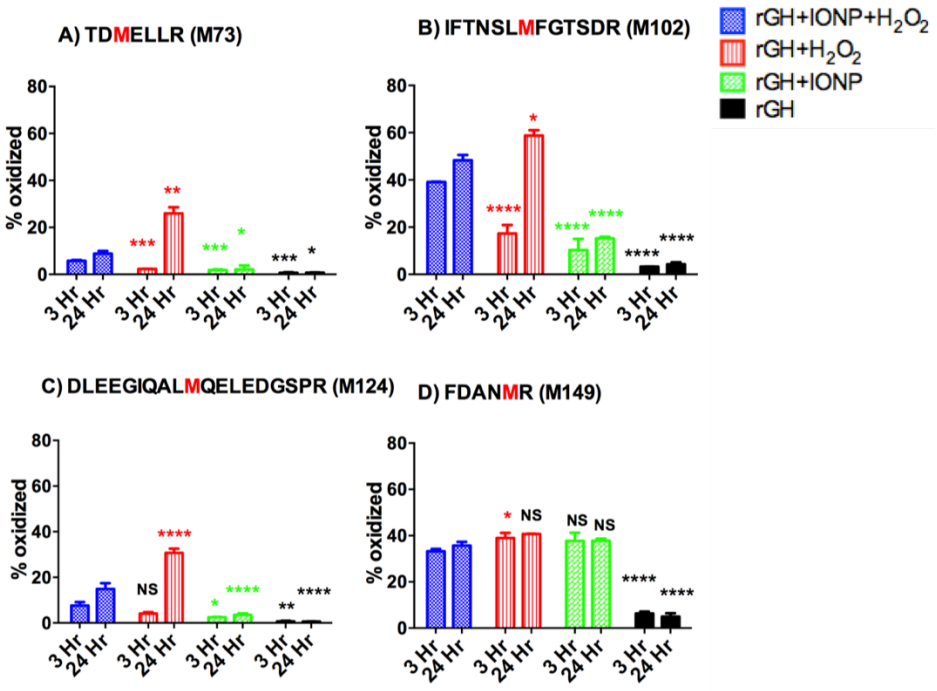

Figure 3.2: Methionine (M73, M102, M124, M149) oxidation in the presence of IONPs and H2O2 using mass spectrometry

The results are presented as percent of the peptide oxidized (mean and standard deviation, n=2). Percent oxidation of various rGH residues was calculated based on the mass spectrometry derived area under the curve of oxidized and non-oxidized peptides.

3 h and 24 h groups were compared separately using 2-way ANOVA. The symbols above each column indicate the 3 or 24 h time points of rGH+IONP+H2O2.

*NS: Not significant, ****: P≤0.0001, ***: P≤0.001, **: P≤0.01, * P≤0.05*

In another experiment, rGH was incubated with AAPH after removing the IONPs to monitor if the effect of IONPs on rGH is reversible. This study showed that even after removing the IONPs, tyrosine residues were not oxidized. Briefly, the IONPs were removed by filtration at the end of 3 h-incubation. Following that, the same amount of additional AAPH was added and incubated again for 3 h. A control sample was kept without any additional AAPH. Differences between these 2 samples were not statistically significant as shown by ANOVA and Tukey's multiple comparison test (Figure 3.20 S12).

The reduced oxidation (Figure 3.3) of rGH in presence of IONPs may be due to loss of protein during the sample processing steps or due to binding to the IONPs. This possibility of the loss of rGH was eliminated by another experiment in which a rGH-IONP mixture and rGH alone were filtered and the filtrate was measured for protein concentration using a BCA assay. There was no significant loss of the protein during filtration with and without IONPs (Figure 3.21 S13). This suggests that the reduced oxidation of rGH seen in the presence of IONPs is due to the IONP binding and not due to loss of protein in the sample processing steps.

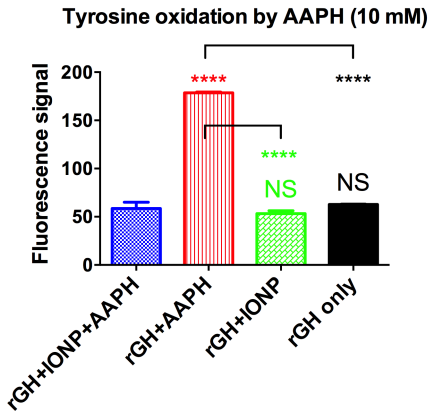

Figure 3.3: Oxidation of tyrosine amino acids of rGH in presence of AAPH (10 mM) and IONPs (1.7 mM) after 3-h of incubation at 37 °C

*Samples were compared using 1-way ANOVA. The symbols above each column indicate comparison with rGH+IONP+AAPH. NS: Not significant, ****: P≤0.0001, ***: P≤0.001, **: P≤0.01, * P≤0.05*

3.3.4 Use of FTIR to monitor IONP-induced changes in rGH secondary structure

The FTIR spectra of rGH were altered after incubation with various concentrations of IONPs, suggesting change in the secondary structure of the protein. Incubation with 1.7-mM IONPs appears to lead to aggregation or intramolecular beta sheet formation resulting in the creation of new bands denoted as a and b, corresponding to 1627 and 1640 cm^{-1} signals, respectively (Figure 3.22 S14). Lower concentrations of IONPs (0.85 and 0.42 mM) leads to more subtle structural changes in the α-helical region (1653 cm^{-1}) (Figure 3.4 and Figure 3.22 S14) (23).

In the presence of 0.85 and 0.42 mM IONPs (1-and 2-h samples) the α-helical band is split into 2 bands at 1649 and 1657 cm^{-1}. This again indicates that the interaction of rGH with the IONPs can lead to structural changes. In addition, there is an increase in intensity of the band around 1680 cm^{-1} compared to pure rGH and the 0-h sample of the rGH-IONP mixture. The spectra of IONPs and phosphate buffer showed that they did not affect the FTIR bands of rGH (Figure 3.23 S15).

The rGH-IONP mixture and rGH were subjected to increasing temperatures from 15 to 85 °C and FTIR spectra were acquired (Figure 3.5). Both groups (with and without IONPs) showed alteration of FTIR spectra with increasing temperature indicating aggregation as manifested by increase in the 1620 cm^{-1} peak. In the presence of IONPs, an additional band at around 1650 cm^{-1} (marked with a dashed red line) was detected in the 'y region' (Figure 3.5). The intramolecular beta sheets are generally observed at 1635 and 1689 cm^{-1} (24). In this study, bands at 1620 and 1694 cm^{-1} were observed, which may indicate intramolecular beta sheet formation. Therefore, the transition temperature for rGH in presence of IONPs is monitored using the 2nd derivative absorbance at 1620 and 1694 cm^{-1} with increasing temperature from 15 to 85 °C (Figure 3.24 S16). The transition temperature in the presence and absence of IONPs was similar (around 55 °C).

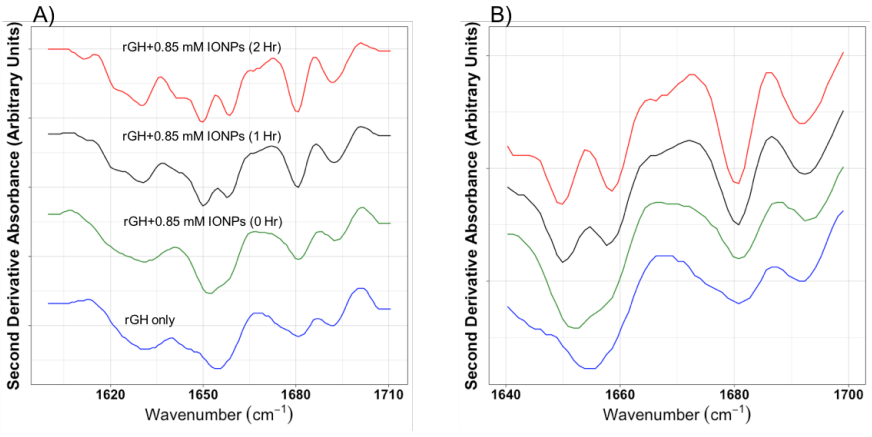

Figure 3.4: Second derivative FTIR spectra of rGH and rGH-IONP mixtures (0.85 mM IONPs) at 25 °C A) Unzoomed and B) Zoomed (1640-1700 cm^{-1})

FTIR spectra were acquired as duplicates or triplicates. Mean representative spectra are shown. Blue: rGH alone; Green: rGH+0.85 mM IONP (0 h); Black: rGH+0.85 mM IONP (1 h); Red: rGH+0.85 mM IONP (2 h)

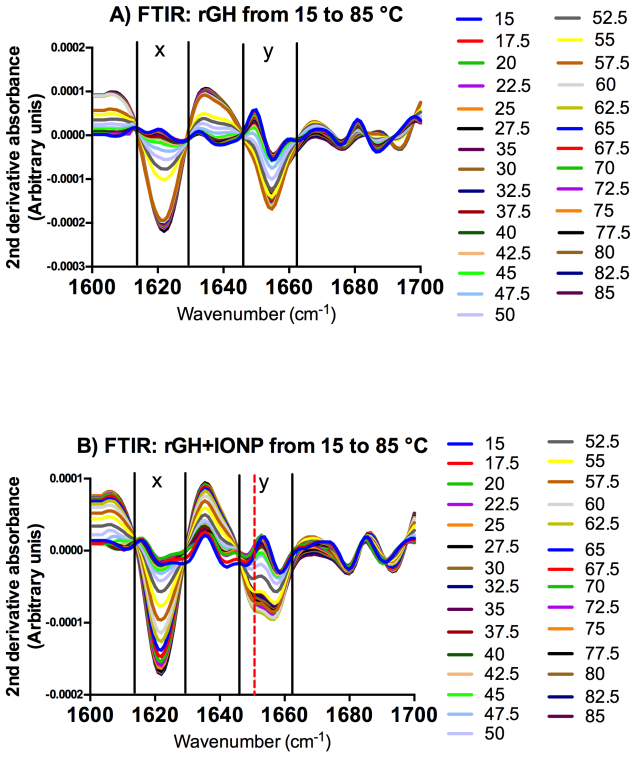

Figure 3.5: FTIR spectra of A) rGH and B) rGH+IONP (1.7 mM) from 15 to 85 °C
(x and y indicate altered regions due to IONPs, dashed red line shows an additional feature observed at 1650 cm^{-1} due to IONPs)

3.3.5 Principal component analysis (PCA) on the FTIR spectra

Principal component analysis was used to differentiate the FTIR spectra generated using rGH and various combinations of the rGH-IONP mixture (Figure 3.6). The spectra of mixtures of rGH and IONPs based on various IONP concentrations (1.7, 0.85 and 0.42 mM) and incubation times (0, 10, 30 min, 1 and 2 h) were separated effectively using PCA. Principle component (PC)1 and PC2 were the major components with contribution of around 50 and 35%, respectively (Figure 3.6-A). Longer incubation (2.5 h) of rGH with 1.7-mM IONPs leads to aggregation and hence it was not included in the PCA. However, other time points (0, 10 and 30 min) of 1.7-mM IONP and rGH mixture were included. Pure rGH, 0-h (1.7, 0.85, 0.42 mM IONP and rGH) and 10-min (1.7

mM IONP and rGH) time points were in the same region of PC1 vs PC2 plot which constitutes the first cluster. There is a second cluster for the 1- and 2-h time points of rGH and 0.42 or 0.85 mM IONP mixtures. In addition, the 30-min time point of rGH and 1.7-mM IONP mixture present in the third cluster. In the case of PC3 vs. PC1 scores plot, pure rGH sample was separated from the other samples (Figure 3.6-B). However, the PC3 contribution was minor (10%) compared to PC1 and PC2 (Figure 3.25 S17). Loading plots (Figure 3.26 S18) indicate that PC1 and PC2 had significant contributions to the α-helical FTIR spectral region (1645 to 1660 cm^{-1}) (23).

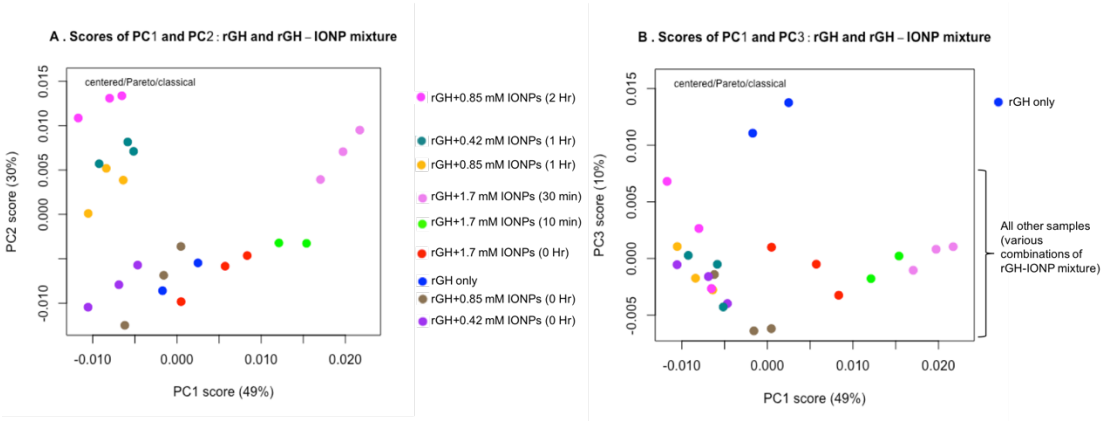

Figure 3.6: Principal component analysis of FTIR spectra for rGH and rGH-IONP mixture at various concentrations of IONPs and incubation times A) Plot of PC1 and PC2, B) Plot of PC1 and PC3

Principal component analysis on the FTIR data acquired with increasing temperature from 15 to 85 °C showed two separate clusters for the rGH and rGH-IONP mixture (Figure 3.7). PC1 was the major component with contribution of around 82%, while PC2 had a lower contribution of around 18% (Figure 3.27 S19). Loading plots indicate that PC1 and PC2 had contributions from the FTIR bands indicating aggregation (1627 cm^{-1}), intramolecular beta sheets (1640 cm^{-1}) and α-helical structure (1645 to 1660 cm^{-1}) (Figure 3.28 S20).

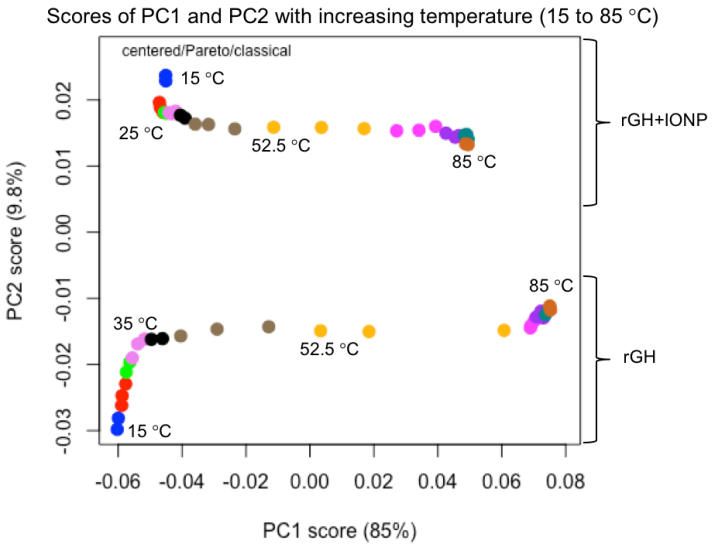

Figure 3.7: Principal component analysis of FTIR spectra acquired for rGH and the rGH-IONP mixture at different temperatures (15 to 85 °C ramping with a 2.5 °C interval)

3.3.6 Circular Dichroism (CD) spectroscopy

CD spectroscopy was also used to evaluate any change in rGH secondary structure due to IONPs. For this study, 3 IONP concentrations were tested (1.7, 0.85 and 0.42 mM). Higher concentration of IONPs (1.7 and 0.85 mM) interfered with the CD spectra (data not shown). Interference from 0.42 mM IONPs was minimal; therefore, this concentration was selected for further analysis. The spectra of rGH alone and the rGH-IONP mixture were identical for lower temperatures (Figure 3.29 S21); however, at higher temperatures (57.5, 60 and 62.5 °C) the CD spectra were different with the negative α-helical band at 208 nm clearly reduced in intensity (Figure 3.8). The transition temperature (66 °C) calculated by measurements at 220 nm was similar for rGH samples with and without IONPs (Figure 3.30 S22). The percent α-helical structure decreased with increases in temperature for both rGH and the rGH-IONP mixture. The contribution of α-helical structure at 40 °C was around 27% and 10% for rGH and the rGH-IONP mixture, respectively. For other temperature points, the α-helical contribution was similar for both

the rGH and rGH-IONP mixture, although visual checks on the CD spectra at different temperatures showed minor changes (Figure 3.8).

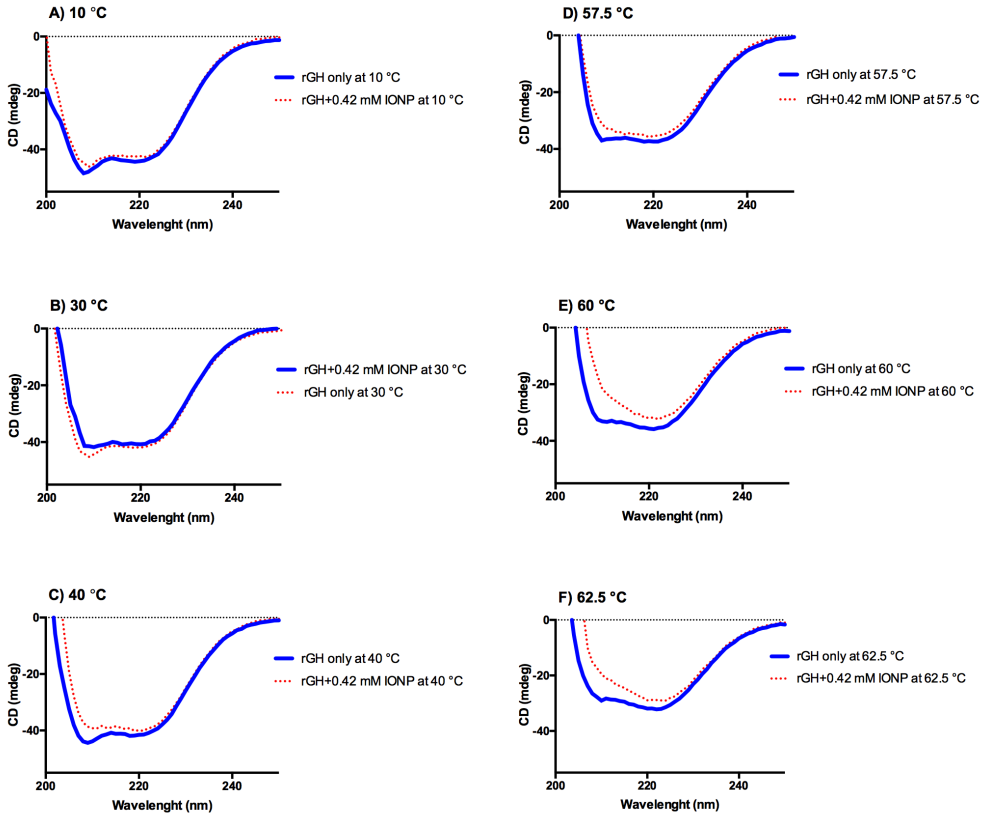

Figure 3.8: Comparison of CD spectra of rGH and rGH-0.42 mM IONP mixtures at various temperatures A) 10 °C, B) 30 °C, C) 40 °C, D) 57.5 °C, E) 60 °C, F) 62.5 °C

3.4 Discussion

Soluble metal impurities from manufacturing processes can oxidize sensitive amino acids via metal-catalyzed reactions that may significantly impact the stability and shelf life of TP formulations. Along with the soluble iron impurities, IONPs may be present as contaminants during TP manufacturing due to the iron shredding of manufacturing equipment. IONPs may also be shredded by the injection needle used during administration of TPs. Therefore, it is important to investigate the impact of IONPs on the oxidation of proteins. Whereas multiple studies have

confirmed the iron induced oxidation of TPs, our results show that the extent of H_2O_2- and AAPH-mediated oxidation of rGH is reduced in the presence of IONPs. This result is in marked contrast with the well-known effect of soluble iron impurities leading to increased oxidation of TPs (3). In our specific case, this may be due to formation of a rGH protein corona around the IONPs, leading to protection from oxidation by the external oxidizing agents. These results were confirmed by monitoring H_2O_2 levels using the FOX assay in the presence of IONPs and without any protein. The H_2O_2 levels did not decrease significantly during 24 h of incubation in the presence of the IONPs (data not shown). This indicated that oxidant levels were not decreased by the IONPs and that suppression of rGH oxidation was due to interaction with the IONPs. In contrast, Jayaram et al reported that titanium dioxide nanoparticles generated ROS (hydroxyl radicals and superoxide radicals), which catalyzed oxidation of corona proteins around the nanoparticles (25).

The oxidation of methionine residues (M73, M102, and M124) was suppressed due to IONPs. However, M149 oxidation was not altered even in the presence of IONPs (Figure 3.4). This could be due to the location of methionine residues in the 3-D structure of rGH. M124 is a part of α-helix number 3 in rGH (11), while other methionine residues are a part of the non-helical polypeptide chains. In the case of M124, the 24-h sample containing IONPs significantly differed ($P \leq 0.0001$) in a level of oxidation from the one without IONPs. The H_2O_2-mediated oxidation of other methionine residues was either not significantly different (M149) in the presence of IONPs or affected to a lesser extent (M73, M102) relatively. These results indicate that the location of methionine residues in the 3-D structure of TP may alter the impact of IONPs on the extent of their oxidation.

The metal oxide nanoparticles can also alter the secondary structure of TPs and enzymes. For example, zinc oxide nanoparticles increased the amount of α-helical structure of lysozyme as

demonstrated by CD and FTIR (26). In addition, airborne nanoparticles changed the expression of proteins by human bronchial epithelial cells (27). Furthermore, alteration of human growth hormone structure due to metal ions (cobalt and iron) was reported previously (28, 29). Trace amounts of copper (>75 ppb) were responsible for cabonylation and aggregation of TPs (30). Formation of higher order clusters of the proteins and gold nanoparticles was demonstrated (5). In another study, CD data showed alteration of secondary structure of cytochrome c due to interaction with gold nanoparticles (31). In this study, the rGH-IONP interaction was studied using FTIR and CD.

Incubation with 1.7-mM IONPs probably leads to aggregation or formation of intramolecular beta sheets as shown by the new FTIR bands at 1627 and 1640 cm^{-1} (Figure 3.22 S14). Similar FTIR bands were reported previously as indicating protein aggregation (1620 cm^{-1}) and intramolecular beta sheets (1635 cm^{-1}) (24, 32). Various amounts of IONPs were tested to analyze alteration of rGH FTIR spectra. PCA was successfully used to distinguish the FTIR spectra of various combinations of rGH-IONP mixtures and incubation time points. Thus, PCA may be useful to distinguish various formulations and provide stability evaluation of TP formulations. The CD spectra of rGH and the rGH-IONP mixture were different at higher temperatures (Figure 3.8). These findings probably reflect a role for IONPs in the alteration of the secondary structure of rGH. In the case of proteins having predominantly α-helical structure, 2 bands are usually observed at around 220 and 208 nm (17). Similar bands were observed for rGH and rGH-IONPs mixtures. In addition, the CD spectra of rGH were similar to the previously published CD spectra acquired from human growth hormone, human pituitary growth hormone and ovine pituitary lactogenic growth hormone (33, 34). In addition, tryptophan fluorescence intensity was used to study effect of IONPs on the tertiary structure of the protein (Figure 3.31 S23) (35). There was not, however,

any significant difference in the CD-determined transition temperatures at various IONP concentrations.

It is well known that oxidation of TPs may lead to alteration of their secondary structure. The changes in secondary structure of TPs can result in alteration of their biological activity, pharmacokinetics and immunogenicity (1). However, it is not clearly known if modification of the secondary structure of TPs due to the metal-nanoparticle interactions (i.e. a corona) can influence the degree of oxidation. These changes in oxidation and secondary structure may impact the overall stability of the TPs. Although this study showed decreased oxidation of rGH and altered secondary structure due to IONPs, the oxidation and secondary structure evaluation experiments were conducted separately using different time points and temperature conditions. For example, the FTIR data were recorded over 2 h and rGH oxidation was studied until 24 h. Furthermore, FTIR and CD spectra were recorded with increasing temperatures up to 90 °C, while oxidation experiments were conducted at a much lower constant temperature (37 °C). Therefore, these experiments do not directly establish a correlation between altered secondary structure and the degree of rGH oxidation. Overall, this study has demonstrated decreased oxidation and alteration in the secondary structure of rGH in the presence of IONPs. It should be emphasized that, effect of the change in secondary structure on the extent of oxidation is not yet clear and must be investigated further.

3.5 Conclusion

This study found that IONPs can affect the degree of oxidation and secondary structure of rGH. In contrast to other reports of increased oxidation of proteins catalyzed by metal nanoparticles, the IONPs decreased H_2O_2- and AAPH-mediated oxidation. This could indicate that

the protein corona that may form around the IONPs could be protective against some forms of chemically induced oxidation. Furthermore, the relative rates of oxidation for amino acids in different locations changed, which means that IONPs may alter the composition of peptide epitopes derived from degraded TPs. Proteins are also oxidized in the presence of soluble iron. However, the rGH protein incubated with IONPs, was not oxidized when compared to control incubations without IONPs. Thus, IONPs generated from the manufacturing processes may impact the stability of TPs, as shown by the altered degree of oxidation and secondary structure. In addition, the utility of PCA was demonstrated on the categorization of different protein stress conditions.

3.6 Supplementary Data

```
        10         20         30         40         50         60
MFPAMPLSSL FANAVLRAQH LHQLAADTYK EFERAYIPEG QRYSIQNAQA AFCFSETIPA

        70         80         90        100        110        120
PTGKEEAQQR TDMELLRFSL LLIQSWLGPV QFLSRIFTNS LMFGTSDRVY EKLKDLEEGI

       130        140        150        160        170        180
QALMQELEDG SPRIGQILKQ TYDKFDANMR SDDALLKNYG LLSCFKKDLH KAETYLRVMK

       190
CRRFAESSCA F
```

Figure 3.9 S1: rGH amino acid sequence

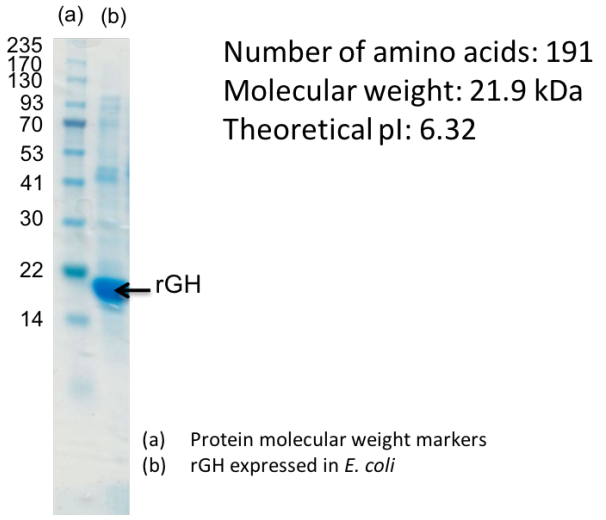

Figure 3.10 S2: SDS-PAGE analysis of rGH

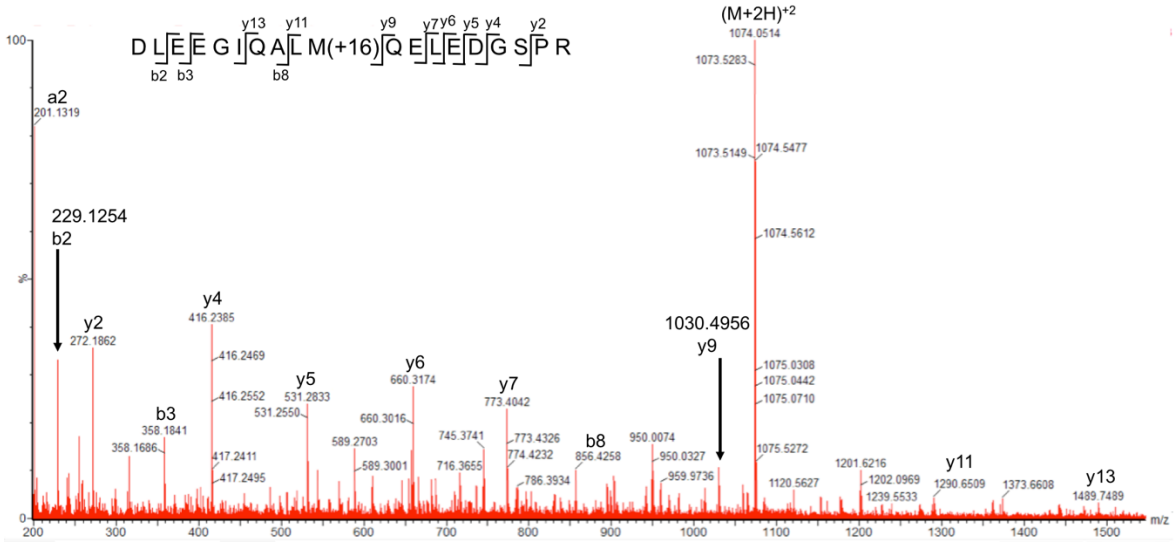

Figure 3.11 S3: Collision induced dissociation (CID) of oxidized peptide DLEEGIQALM(+16)QELEDGSPR obtained using LC-ESI-MS

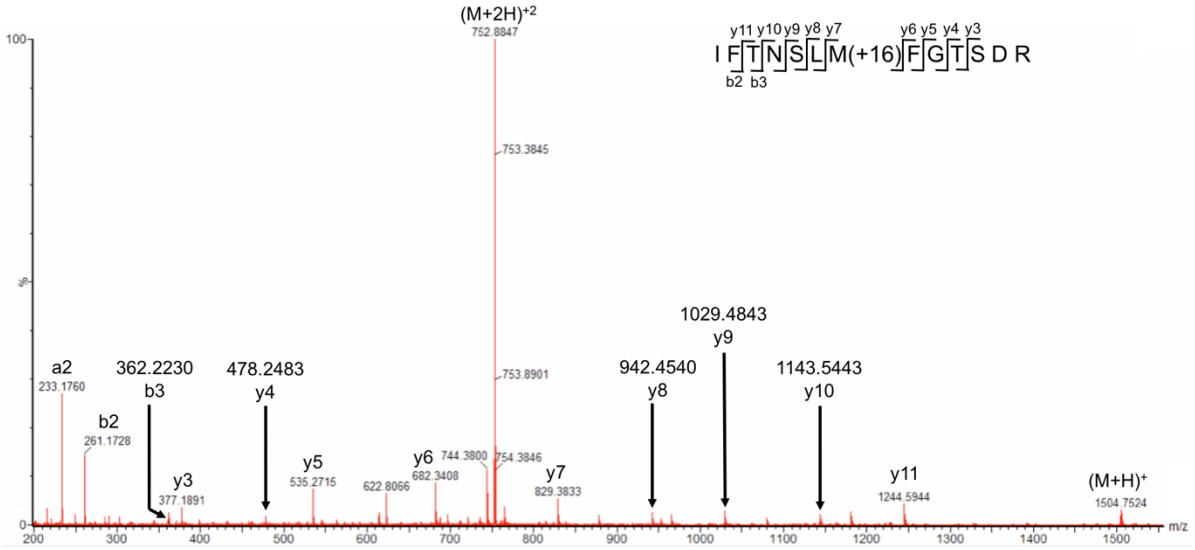

Figure 3.12 S4: CID of oxidized peptide IFTNSLM(+16)FGTSDR obtained using LC-ESI-MS

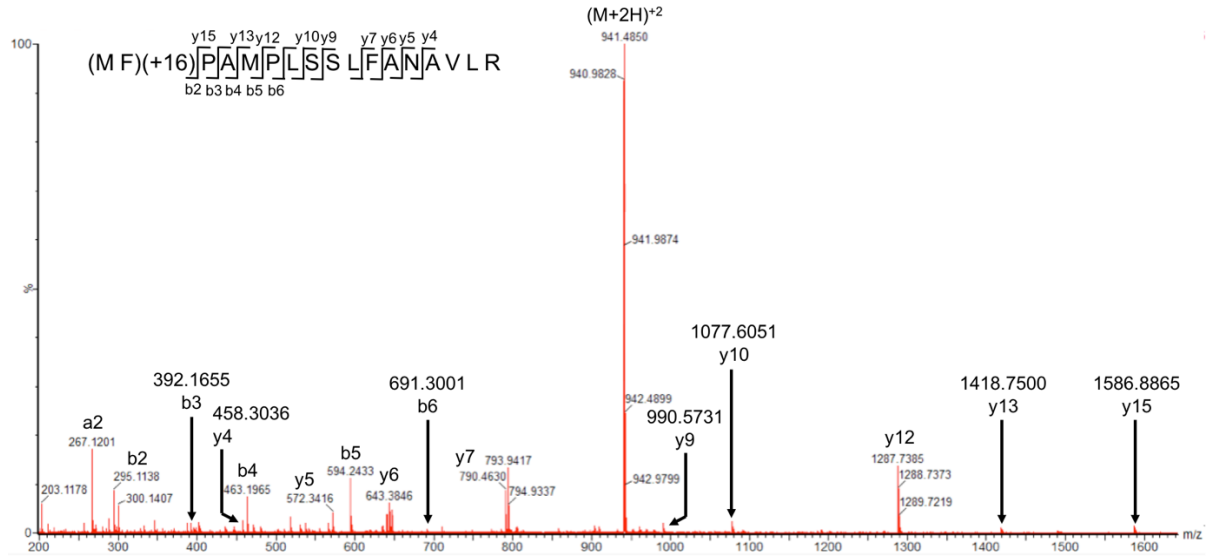

Figure 3.13 S5: CID of oxidized peptide (MF)(+16)PAMPLSSLFANAVLR obtained using LC-ESI-MS

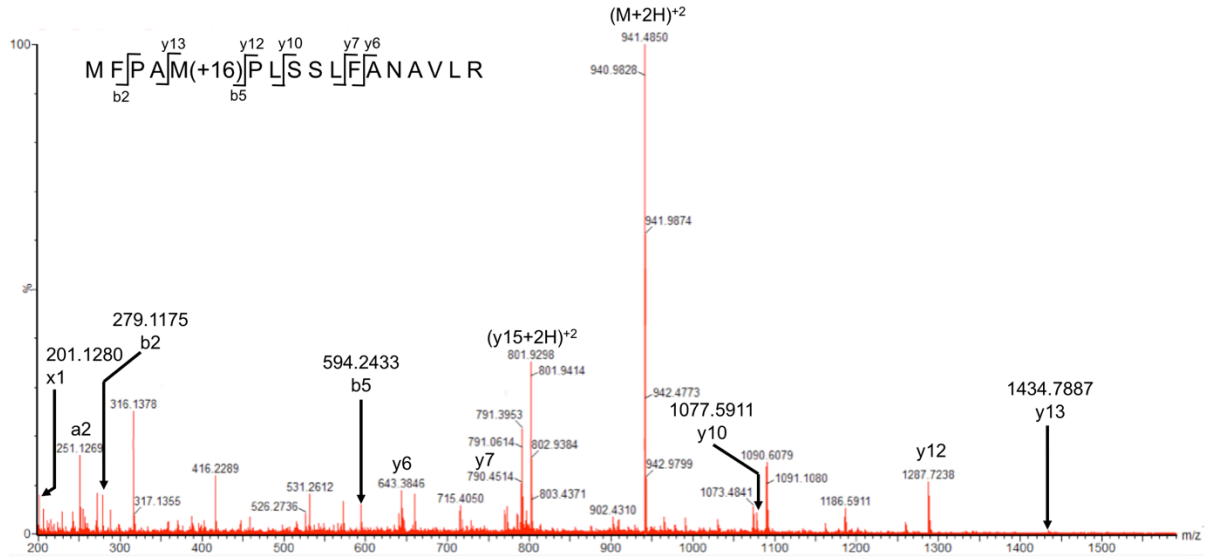

Figure 3.14 S6: CID of oxidized peptide MFPAM(+16)PLSSLFANAVLR obtained using LC-ESI-MS

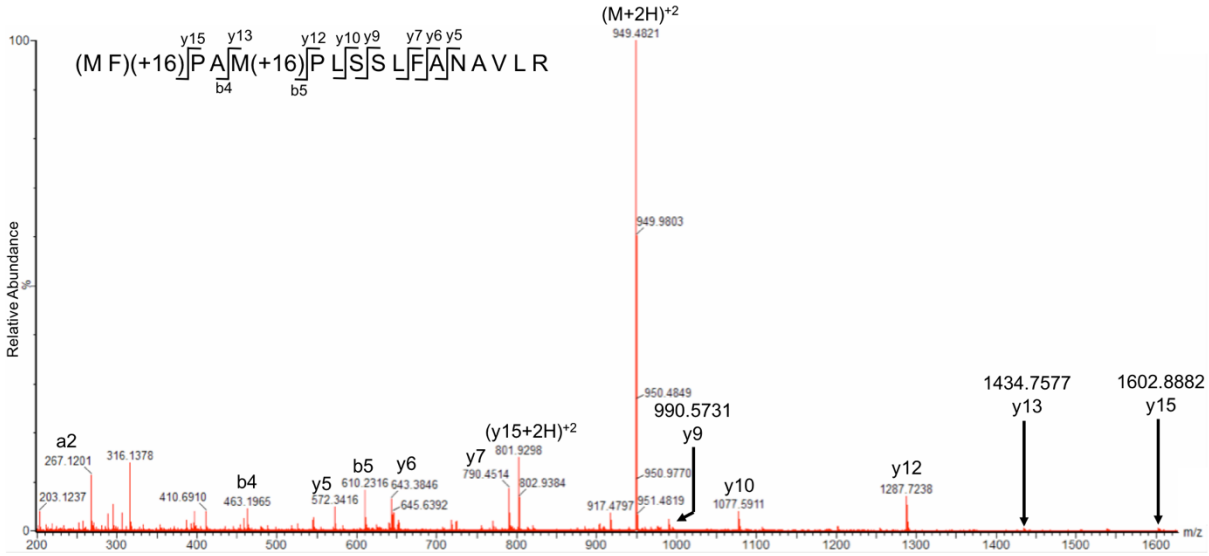

Figure 3.15 S7: CID of dioxidized tryptic peptide (MF)(16+)PAM(+16)PLSSLFANAVLR obtained using LC-ESI-MS

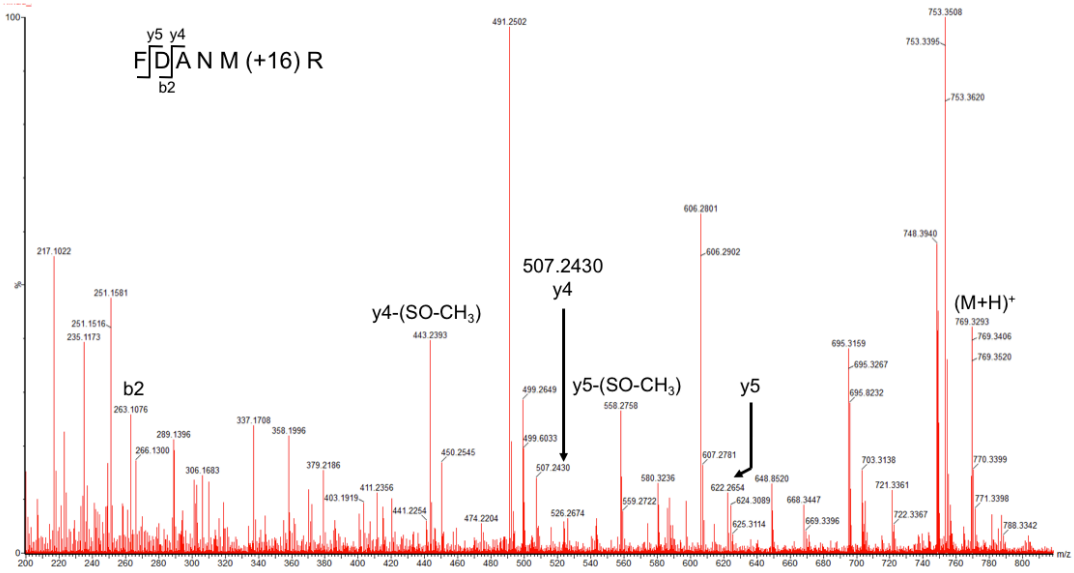

Figure 3.16 S8: CID of oxidized tryptic peptide FDANM(+16)R obtained using LC-ESI-MS

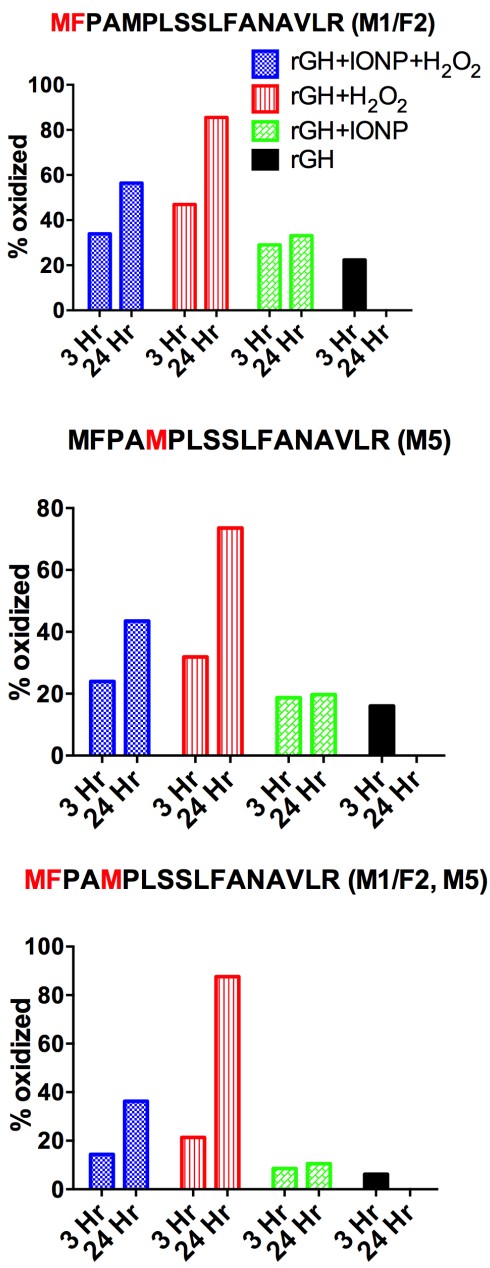

Figure 3.17 S9: Methionine/phenylalanine (M1/F2, M5) oxidation in the presence of IONPs and H2O2 using mass spectrometry

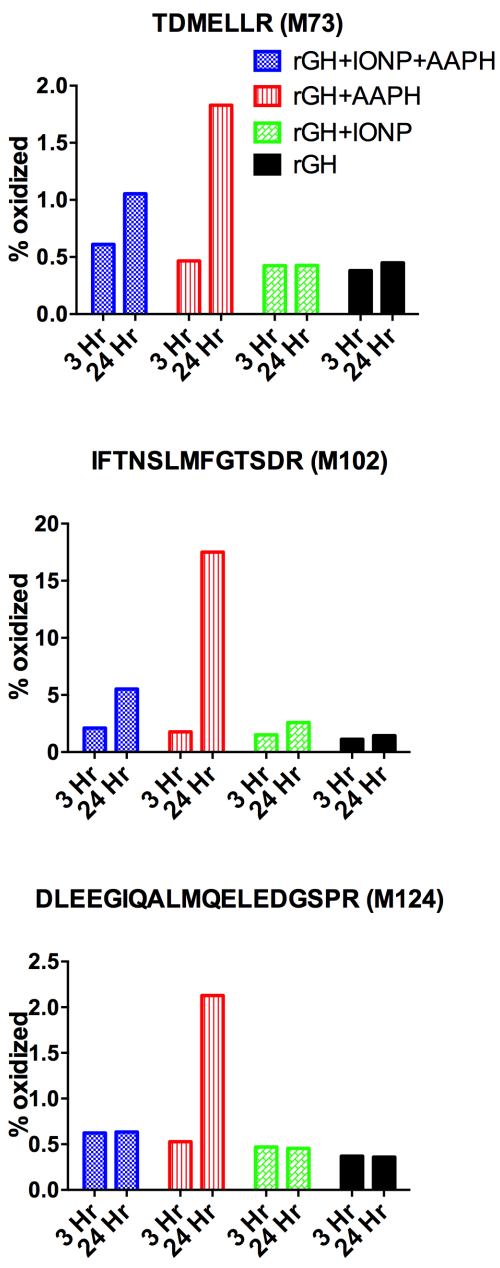

Figure 3.18 S10: Methionine (M73, M102, M124) oxidation in the presence of IONPs and AAPH using mass spectrometry

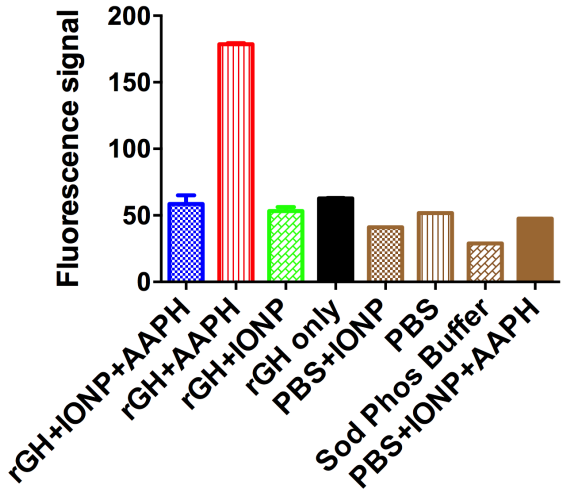

Figure 3.19 S11: AAPH-induced (tyrosine) oxidation of rGH using fluorogenic derivatization assay and comparison with the control groups

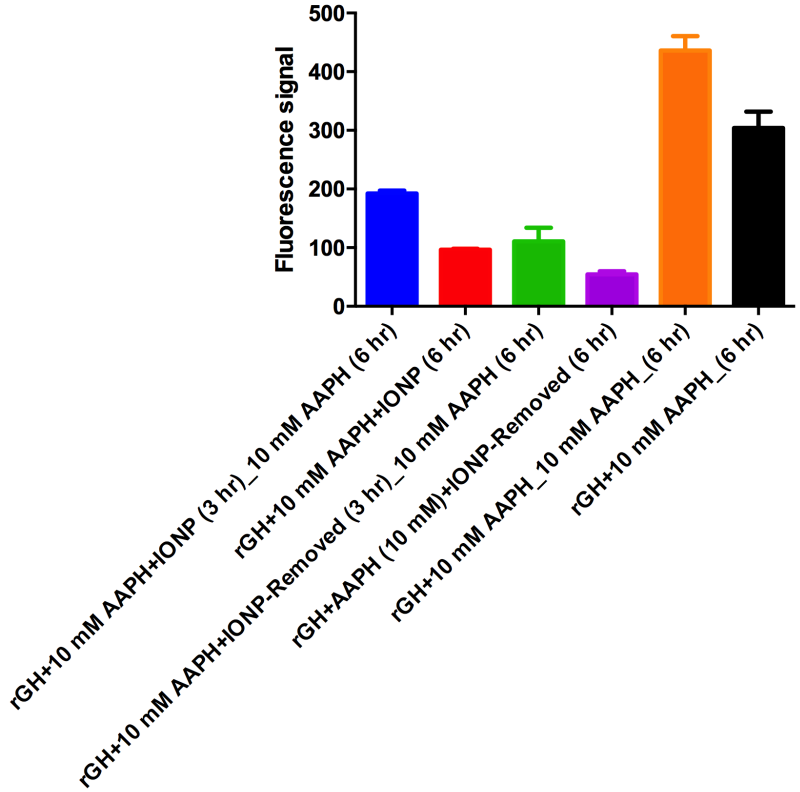

Figure 3.20 S12: Effect of IONP removal on AAPH-induced (tyrosine) oxidation of rGH using fluorogenic derivatization assay

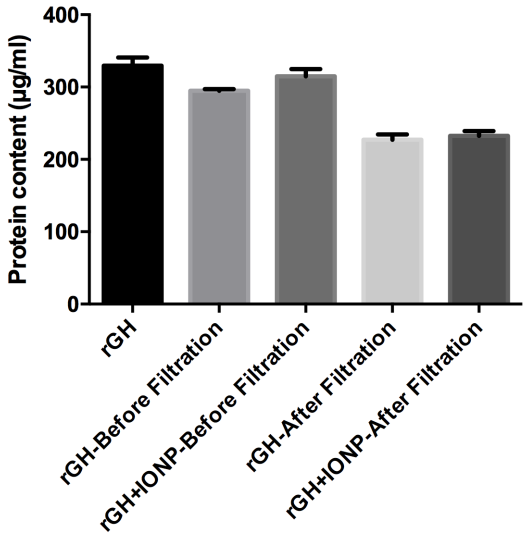

Figure 3.21 S13: Loss of protein content due to filtration in the presence of IONPs

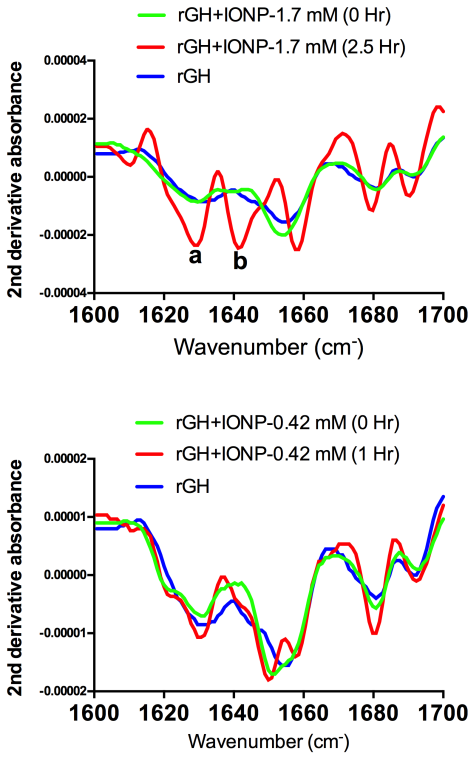

Figure 3.22 S14: Second derivative FTIR spectra of rGH and rGH-IONP (1.7 and 0.42 mM) mixture at 25 °C

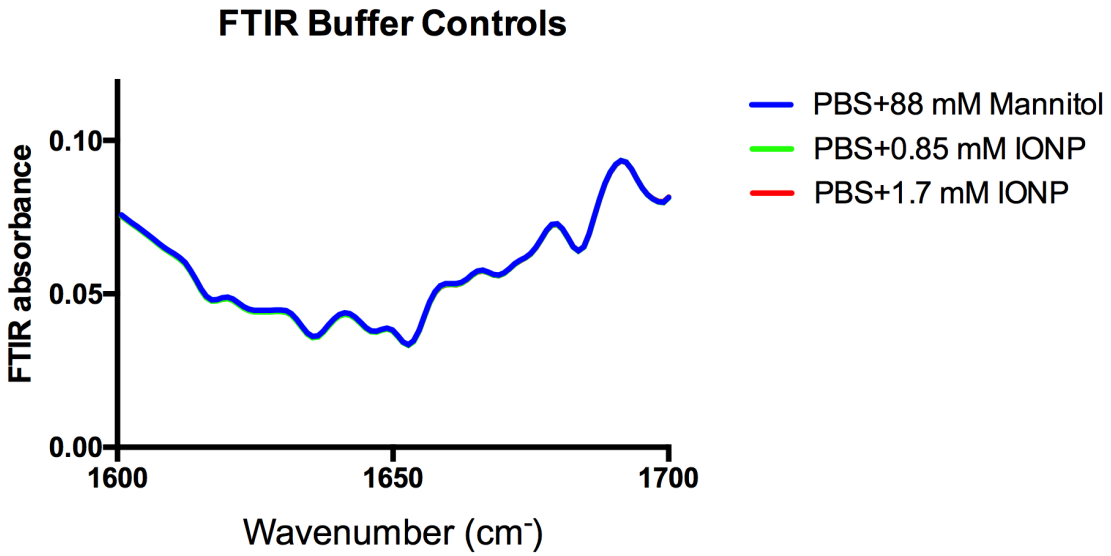

Figure 3.23 S15: FTIR buffer controls to demonstrate that mannitol in the rGH formulation and IONPs incubated with the protein did not interfere with the spectra

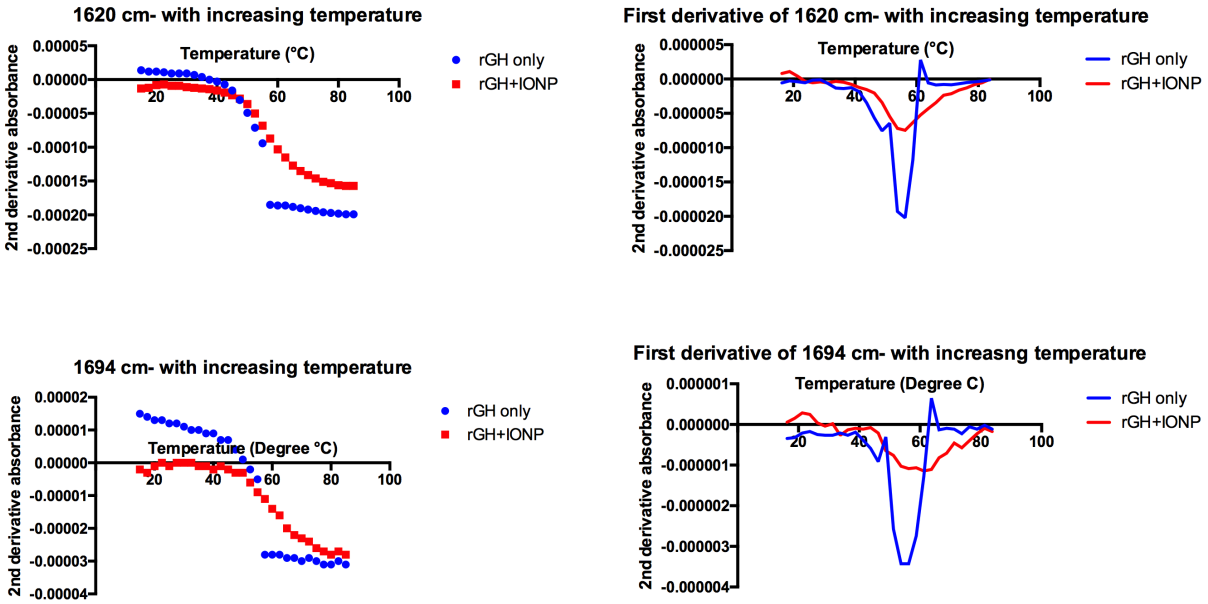

Figure 3.24 S16: Transition temperature for the rGH-IONP mixture using FTIR spectra (IONP-1.7 mM)

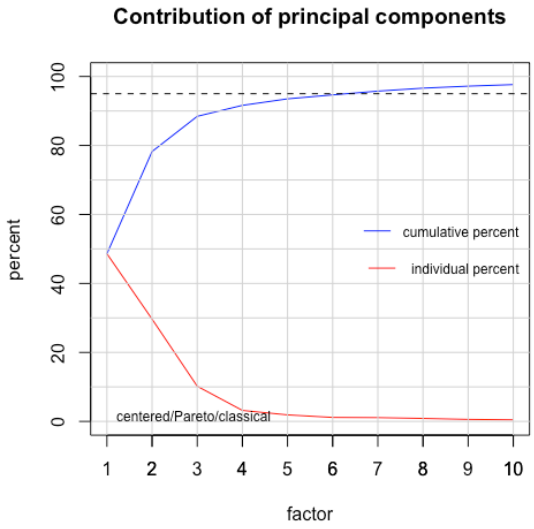

Figure 3.25 S17: Contribution of principle components (PC) to explain variance in the FTIR data acquired for rGH and rGH-IONP incubation at room temperature

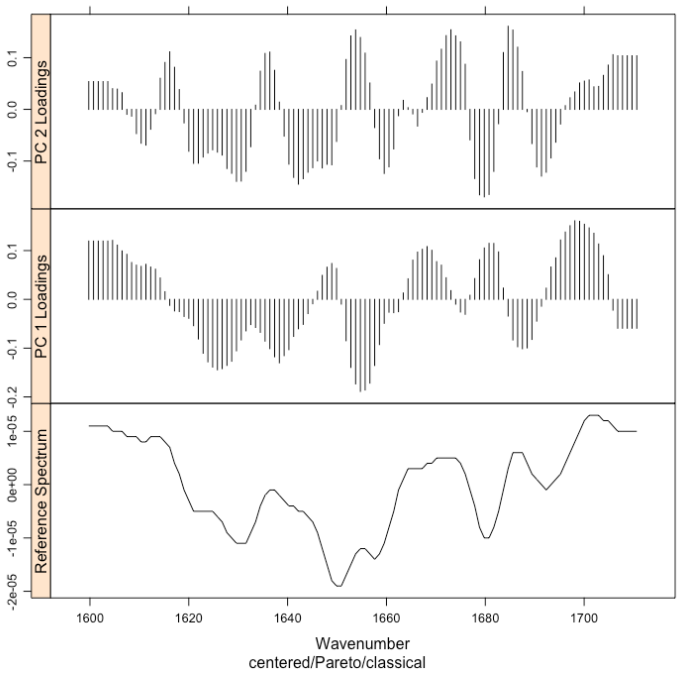

Figure 3.26 S18: Loadings for PC1 and PC2 for the FTIR data acquired for rGH and rGH-IONP incubation at room temperature (reference FTIR spectra: rGH + IONP (0.42 mM) incubation at 1 h.)

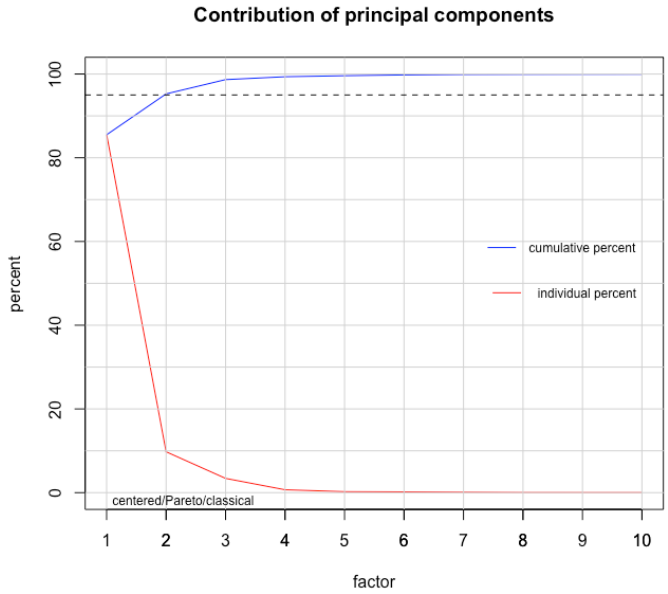

Figure 3.27 S19: Contribution of principle components (PC) to explain variance in the FTIR data acquired for rGH and rGH-IONP mixture at various temperatures (15 to 85 °C)

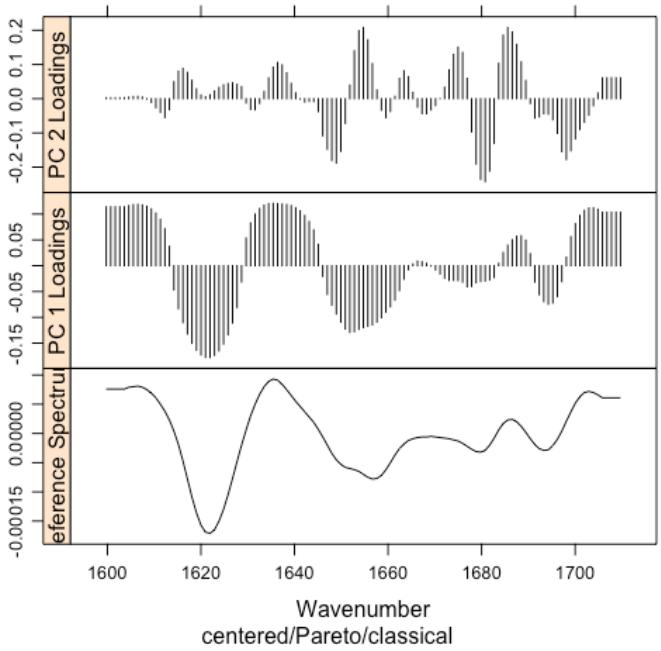

Figure 3.28 S20: Loadings for PC 1 and PC 2 for the FTIR data acquired for rGH and rGH-IONP mixture at various temperatures (15 to 85 °C) (reference FTIR spectra: rGH+IONP mixture at 85 °C)

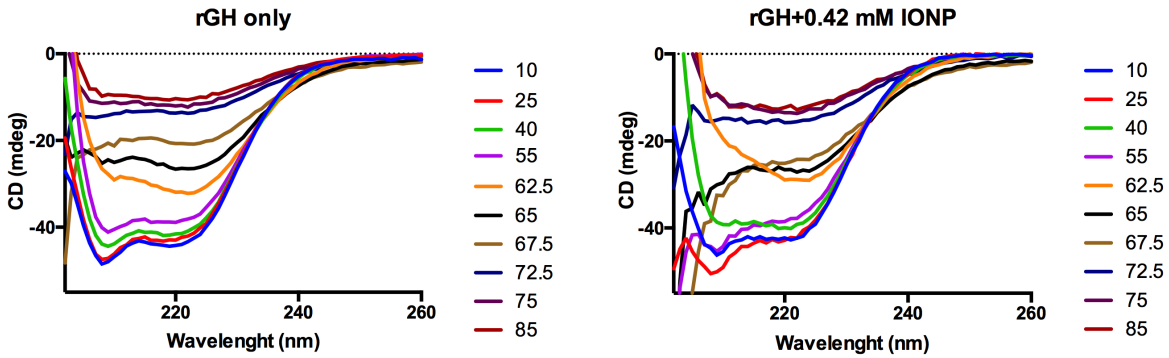

Figure 3.29 S21: Circular dichroism (CD) spectra for rGH and rGH-IONP mixture with increasing temperature
CD spectra was acquired from 10 to 90 ℃ with interval of 2.5 ℃. Above figure shows CD spectra at selected temperature points.

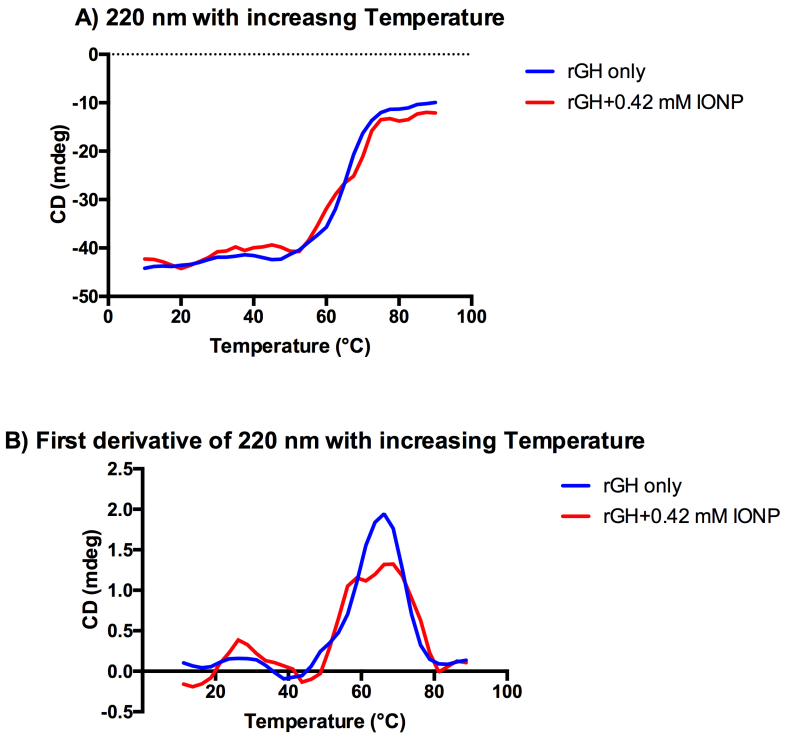

Figure 3.30 S22: A) CD measurement at 220 nm with increasing temperature B) First derivative of 220 nm readings with increasing temperature

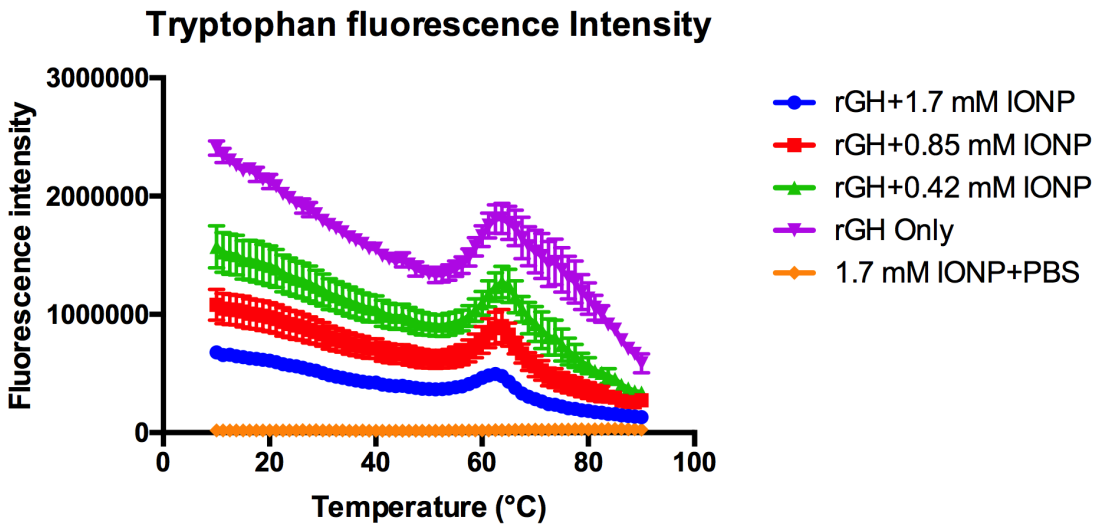

Figure 3.31 S23: Effect of IONPs on tryptophan fluorescence intensity with increasing temperature from 15 to 90 °C

The instrument used for measuring tryptophan fluorescence was manufactured by Fluorescence Innovations Inc. (Minneapolis, MN). Previsouly reported methods were used (35).

3.7 References

1. Torosantucci R, Schöneich C, Jiskoot W. Oxidation of therapeutic proteins and peptides: structural and biological consequences. Pharm Res. 2014;31(3):541-553
2. Bendtzen K, Geborek P, Svenson M, Larsson L, Kapetanovic MC, Saxne T. Individualized monitoring of drug bioavailability and immunogenicity in rheumatoid arthritis patients treated with the tumor necrosis factor α inhibitor infliximab. Arthritis & Rheumatology. 2006;54(12):3782-3789
3. Mozziconacci O, Ji JA, Wang YJ, Schöneich C. Metal-catalyzed oxidation of protein methionine residues in human parathyroid hormone (1-34): Formation of homocysteine and a novel methionine-dependent hydrolysis reaction. Mol Pharm. 2013;10(2):739-755
4. Li S, Schöneich C, Borchardt RT. Chemical instability of protein pharmaceuticals: mechanisms of oxidation and strategies for stabilization. Biotechnol Bioeng. 1995;48(5):490-500
5. Moerz ST, Kraegeloh A, Chanana M, Kraus T. Formation mechanism for stable hybrid clusters of proteins and nanoparticles. ACS nano. 2015;9(7):6696-6705
6. Treuel L, Malissek M. Interactions of nanoparticles with proteins: Determination of equilibrium constants. Cellular and Subcellular Nanotechnology: Methods and Protocols. 2013:225-235
7. Sakulkhu U, Mahmoudi M, Maurizi L, Salaklang J, Hofmann H. Protein corona composition of superparamagnetic iron oxide nanoparticles with various physico-chemical properties and coatings. Sci Rep. 2014;4:5020
8. Fradkin AH, Mozziconacci O, Schöneich C, Carpenter JF, Randolph TW. UV photodegradation of murine growth hormone: chemical analysis and immunogenicity consequences. Eur J Pharm Biopharm. 2014;87(2):395-402

9. Bommana R, Mozziconacci O, Wang YJ, Schöneich C. An Efficient and Rapid Method to Monitor the Oxidative Degradation of Protein Pharmaceuticals: Probing Tyrosine Oxidation with Fluorogenic Derivatization. Pharm Res. 2017;34(7):1428-1443
10. Sharov VS, Dremina ES, Galeva NA, Gerstenecker GS, Li X, Dobrowsky RT, Stobaugh JF, Schöneich C. Fluorogenic tagging of peptide and protein 3-nitrotyrosine with 4-(aminomethyl) benzenesulfonic acid for quantitative analysis of protein tyrosine nitration. Chromatographia. 2010;71(1-2):37-53
11. Abdel-Meguid SS, Shieh H-S, Smith WW, Dayringer HE, Violand BN, Bentle LA. Three-dimensional structure of a genetically engineered variant of porcine growth hormone. Proceedings of the National Academy of Sciences. 1987;84(18):6434-6437
12. Fradkin AH, Boand CS, Eisenberg SP, Rosendahl MS, Randolph TW. Recombinant murine growth hormone from E. coli inclusion bodies: Expression, high-pressure solubilization and refolding, and characterization of activity and structure. Biotechnol Prog. 2010;26(3):743-749
13. NCBI. Growth hormone 1 (Rattus norvegicus) GenBank: AAI66872.1. 2018 June 8, 2018. Available from: https://www.ncbi.nlm.nih.gov/protein/187469098/.
14. Mozziconacci O, Stobaugh JT, Bommana R, Woods J, Franklin E, Jorgenson JW, Forrest ML, Schöneich C, Stobaugh JF. Profiling the Photochemical-Induced Degradation of Rat Growth Hormone with Extreme Ultra-pressure Chromatography–Mass Spectrometry Utilizing Meter-Long Microcapillary Columns Packed with Sub-2-µm Particles. Chromatographia. 2017;80(9):1299-1318
15. Nelson CA, Lee CA, Fremont DH. Oxidative refolding from inclusion bodies. In. Structural Genomics and Drug Discovery: Springer; 2014. p. 145-157.
16. Torosantucci R, Mozziconacci O, Sharov V, Schöneich C, Jiskoot W. Chemical modifications in aggregates of recombinant human insulin induced by metal-catalyzed oxidation: covalent cross-linking via michael addition to tyrosine oxidation products. Pharm Res. 2012;29(8):2276-2293
17. Micsonai A, Wien F, Kernya L, Lee Y-H, Goto Y, Réfrégiers M, Kardos J. Accurate secondary structure prediction and fold recognition for circular dichroism spectroscopy. Proceedings of the National Academy of Sciences. 2015;112(24):E3095-E3103
18. Perry R, San Clemente C. Determination of iron with bathophenanthroline following an improved procedure for reduction of iron (III) ions. Analyst. 1977;102(1211):114-119
19. Anastácio AS, Harris B, Yoo H-I, Fabris JD, Stucki JW. Limitations of the ferrozine method for quantitative assay of mineral systems for ferrous and total iron. Geochim Cosmochim Acta. 2008;72(20):5001-5008
20. Fortune W, Mellon M. Determination of iron with o-phenanthroline: a spectrophotometric study. Industrial & Engineering Chemistry Analytical Edition. 1938;10(2):60-64
21. Hanson BA. ChemoSpec: Exploratory Chemometrics for Spectroscopy. R package version 4.4.97. Available from: https://cran.r-project.org/package=ChemoSpec.
22. Guan Z, Yates NA, Bakhtiar R. Detection and characterization of methionine oxidation in peptides by collision-induced dissociation and electron capture dissociation. J Am Soc Mass Spectrom. 2003;14(6):605-613
23. Barth A. Infrared spectroscopy of proteins. Biochimica et Biophysica Acta (BBA)-Bioenergetics. 2007;1767(9):1073-1101

24. Dong A, Prestrelski SJ, Allison SD, Carpenter JF. Infrared spectroscopic studies of lyophilization-and temperature-induced protein aggregation. J Pharm Sci. 1995;84(4):415-424
25. Jayaram DT, Runa S, Kemp ML, Payne CK. Nanoparticle-induced oxidation of corona proteins initiates an oxidative stress response in cells. Nanoscale. 2017;9(22):7595-7601
26. Elbrecht D, Mitchell J, Lekey A, Marquardt K, Knight K, Smith J, DeLong R. Nanoproteomics: The convergence of protein science and nanotechnology with important applications for bio-element metal and etal oxide nanoparticles. Reviews in Nanoscience and Nanotechnology. 2013;2(5):365-381
27. Park SK, Jeon YM, Son BS, Youn HS, Lee MY. Proteomic analysis of the differentially expressed proteins by airborne nanoparticles. J Appl Toxicol. 2011;31(5):463-470
28. Saboury A, Ghourchaei H, Sanati M, Atri M, Rezaei-Tawirani M, Hakimelahi G. Binding properties and structural changes of human growth hormone upon interaction with cobalt ion. J Therm Anal Calorim. 2007;89(3):921-927
29. Atri M, Saboury A, Rezaei-Tavirani M, Sanati M, Moosavi-Movahedi AA, Sadeghi M, Mansuri-Torshizi H, Khodabandeh M. Binding properties and conformational change of human growth hormone upon interaction with Fe3+. Thermochim Acta. 2005;438(1-2):178-183
30. Kryndushkin D, Rao VA. Comparative effects of metal-catalyzed oxidizing systems on carbonylation and integrity of therapeutic proteins. Pharm Res. 2016;33(2):526-539
31. Aubin-Tam M-E, Hamad-Schifferli K. Gold nanoparticle− cytochrome C complexes: the effect of nanoparticle ligand charge on protein structure. Langmuir. 2005;21(26):12080-12084
32. Dong A, Matsuura J, Manning MC, Carpenter JF. Intermolecular β-sheet results from trifluoroethanol-induced nonnative α-helical structure in β-sheet predominant proteins: Infrared and circular dichroism spectroscopic study. Arch Biochem Biophys. 1998;355(2):275-281
33. Bewley TA, Li CH. Circular dichroism studies on human pituitary growth hormone and ovine pituitary lactogenic hormone. Biochemistry. 1972;11(5):884-888
34. Lim JY, Kim NA, Lim DG, Kim KH, Jeong SH. Effects of thermal and mechanical stress on the physical stability of human growth hormone and epidermal growth factor. Arch Pharm Res. 2015;38(8):1488-1498
35. Wei Y, Larson NR, Angalakurthi SK, Russell Middaugh C. Improved Fluorescence Methods for High-Throughput Protein Formulation Screening. SLAS Technol. 2018:1-13

Chapter 4 : A minimal physiologically based pharmacokinetic model describing the altered metabolism of midazolam due to inflammation

4.1 Introduction

Inflammation and other disease conditions are known to alter the expression of cytochrome P450 enzymes (CYPs) due to increased proinflammatory cytokine levels (1, 2). Typically, cytokines such as IL-6, IL-1β, IFN-γ and TNF-α are increased during inflammation. Elevated cytokine levels can lead to suppression of various CYPs. Increased IL-6 levels downregulate CYP3A4, while TNF-α downregulates CYP2C19 (3-5). Thus, inflammation and elevated cytokine levels may cause disease-drug interactions by altering the pharmacokinetics (PK) and specifically clearance of drugs that are metabolized by CYPs.

Cytokine-mediated CYP suppression is believed to occur through a nuclear receptor, hepatic nuclear factor-4α (HNF-4α). Elevated IL-6, TNF-α and IL-1β can inhibit the action of HNF-4α. HNF-4α is involved in the regulation of pregnane X receptor (PXR) and constitutive androstane receptor (CAR) that are responsible for regulating the expression of CYP3A4 following exposure to some xenobiotics (4). Elevated IL-6 is known to down-regulate CYP3A4, CYP2C9, CYP2C19 and CYP1A2, while TNF-α down-regulates CYP2C19 (3, 6). In this study, the hypothesis was that the elevated cytokines during inflammation (diseased state) would suppress the expression of mouse cyp3a11 (76% amino acid homology with the human CYP3A4) (7), which may lead to changes in PK of its substrates.

In the case of glucose-6-phosphate isomerase (GPI)-mediated inflammation in DBA/1 mice, circulating levels of IL-6 and TNF-α were increased (8). This GPI model of inflammation is frequently used to test the anti-inflammatory activity of new chemical entities (NCEs) (9). The PK of NCEs is generally studied using healthy mice, and the data are often used to inform dose

selection for demonstration of efficacy in an inflammation model. Therefore, it is worthwhile to develop a mechanistic approach, which includes the CYP activity differences in healthy versus diseased mice, to inform dose selection for the pharmacological assays utilizing the GPI model. The overall goal of this study was to build a model for dose selection, which can more accurately predict dose response in the diseased state based off healthy animal-PK data and *in vitro* metabolism data (healthy and diseased).

Midazolam (MDZ), a known CYP3A4 substrate, was selected as a model compound for *in vitro* metabolism and PK studies. Lipopolysaccharide- (10, 11) and carrageenan-induced inflammation (12) both have been reported to alter the PK of MDZ. Metabolism of MDZ was evaluated using liver microsomes prepared from healthy and GPI-treated mice. According to the published *in vitro* experiments in humans and rodents, MDZ is mainly metabolized by CYP3A to form 1-OH-MDZ and 4-OH-MDZ. The phase 1 metabolites of MDZ may be further conjugated with glucuronide to form 1-OH-MDZ-glucuronide and 4-OH-MDZ-glucuronide. In a PK study using chimeric mice with humanized livers (PXB mice), 1-OH-MDZ, 4-OH-MDZ, 1,4-diOH-MDZ, and 1-OH-MDZ-glucuronide were detected in plasma. However, 4-OH-MDZ and 1-OH-MDZ-glucuronide were not detected in severe combined immune deficient (SCID) mice (10, 13-15).

In this work, a minimal physiologically based pharmacokinetic (PBPK) model was constructed to predict PK of MDZ in mice with GPI-mediated inflammation. The model equations and methodology could be applied to other drugs to predict altered PK parameters in disease models using a limited data set, including healthy-animal PK data and *in vitro* liver microsome studies.

4.2 Methods

The methods section is divided into various subsections describing the *in vitro* metabolism, PK, Liquid Chromatography-Mass Spectrometry (LC-MS) analysis, minimal PBPK model, and quantitation of cytokines and mRNA. Briefly, the rate of 1-OH-MDZ formation in the liver microsomes was used to assess the degree of inflammation-mediated suppression of MDZ metabolism. In addition, MDZ PK parameters were compared in the healthy and GPI-treated mice. Finally, both the *in vitro* (in healthy and GPI mice) and PK data (in healthy mice) were used to build the minimal PBPK model. The *in vitro* microsomal data defined metabolism of MDZ from the liver and intestines, while the parameters associated with a 2-compartment model were estimated using the healthy animal PK data. These estimated PK parameters were used to define the central and peripheral compartments of the minimal PBPK model (Figure 4.4). The 2-compartment model PK parameters from GPI mice were used to illustrate that the PK in the diseased state can be predicted using *in vitro* (healthy and diseased animals) and healthy animal PK data. In addition, serum cytokine levels were measured in the healthy mice and on days 12 and 21 after GPI treatment. The mRNA-levels of cyp3a11, cyp2c29 and cyp2d26 in liver were also measured on days 1, 5, 8 and 15 after GPI treatment.

4.2.1 Animals

Male DBA/1 mice (Harlan Laboratories, Indianapolis, IN) were acclimatized for 3 days and housed as 4 animals per cage or individually if a cage mate was not available. Animals were approximately 9-10 weeks old at the start of the study. A 12-h light and 12-h dark cycle was maintained throughout the study. Mice were fed and given access to water ad libitum. All procedures were in compliance with the Guide for the Care and Use of Laboratory Animals: Eighth

Edition, (Institute for Laboratory Animal Research, The National Academies Press, Washington, D.C.); and the National Institutes of Health, Office of Laboratory Animal Welfare (NIH publication no. 85-23, revised 1985). Whenever possible, procedures were designed to avoid or minimize discomfort, distress, and pain to the animals.

4.2.2 GPI treatment

The mice were treated with GPI according to a previously published protocol with a few modifications (16). Briefly, a 4-mg/mL solution of recombinant human GPI was mixed with an equal volume of complete Freund's adjuvant. This final 2 mg/mL solution of GPI was used for the treatment. A 100-µL (200-µg) injection of the above solution was administered at both sides of the tail base to induce inflammation.

4.2.3 Preparation of mouse liver microsomes (MLM) and in vitro experiments

Healthy and diseased mice were sacrificed using cardiac puncture either immediately or on day 12 after the GPI treatment, and the livers were collected and stored at -80° C until immediately before use. The MLM were prepared using previously reported protocols (17, 18). The protein content of MLM was measured using the bicinchoninic acid assay using a reported procedure (19). Liver microsome kinetic studies of 1-OH-MDZ and 4-OH-MDZ formation were carried out by following the reported methods (13, 15, 20). Based on the linear relationship of MDZ metabolism and MLM protein concentration from 0.1 to 0.5 mg/mL (data not shown), a protein content of 0.1 mg/mL was selected for all subsequent microsomal experiments. A 2-min incubation time was selected for kinetic experiments based on an earlier study, which reported that the incubation time for formation of the metabolites was linear up to 20 min using MLM and human liver microsomes

(HLM) (20). The rate of 1-OH-MDZ and 4-OH-MDZ formation was measured at concentrations of MDZ ranging from 0 to 250 μM. The data obtained was fitted to a substrate inhibition kinetics using GraphPad Prism 6 (GraphPad Software Inc., La Jolla, CA).

4.2.4 Pharmacokinetics of MDZ

MDZ was administered via intravenous (IV) or oral (PO) routes at 1 mg/kg or 5 mg/kg, respectively. The PO bioavailability of MDZ was low (F=0.023) according to the previously published report (21). Therefore, a higher PO dose was selected. Approximately 20 μL of blood was collected using a capillary and applied directly on dried blood spot (DBS) cards at time points as follows: IV- 0.08, 0.166, 0.33, 0.5, 1, 2, 4, 6, 8 h and PO- 0.166, 0.33, 0.5, 1, 2, 4, 6, 8 h. The DBS samples were analyzed for MDZ, 1-OH-MDZ, 4-OH-MDZ and 1-OH-MDZ-glucuronide. The MDZ used for dosing in the PK studies was obtained from Hospira (Lake Forrest, IL). The MDZ, 1-OH-MDZ and 4-OH-MDZ standards were obtained from Cerilliant Corporation (Round Rock, TX), while the 1-OH-MDZ-glucuonide standard was obtained from Toronto Research Chemicals (Ontario, Canada).

Pharmacokinetics of MDZ in the healthy and diseased mice were compared using 3 animal groups as shown in the Figure 4.1. The first group was not treated with GPI and was kept for 21 days before MDZ dosing and DBS sample collection. The second group was treated with GPI on day 10 of the study, while the third group was treated with GPI on day 1. Finally, MDZ was administered on day 21, and DBS samples were subsequently collected to measure blood concentration of the analytes (MDZ, 1-OH-MDZ, 4-OH-MDZ and 1-OH-MDZ-glucuronide). The healthy and diseased animal PK parameters were obtained using non-compartmental analysis

(NCA) using SimBiology (Matlab R2017a). Analysis of variance (ANOVA) and Tukey's comparison test were used to determine differences in PK parameters in healthy and diseased mice.

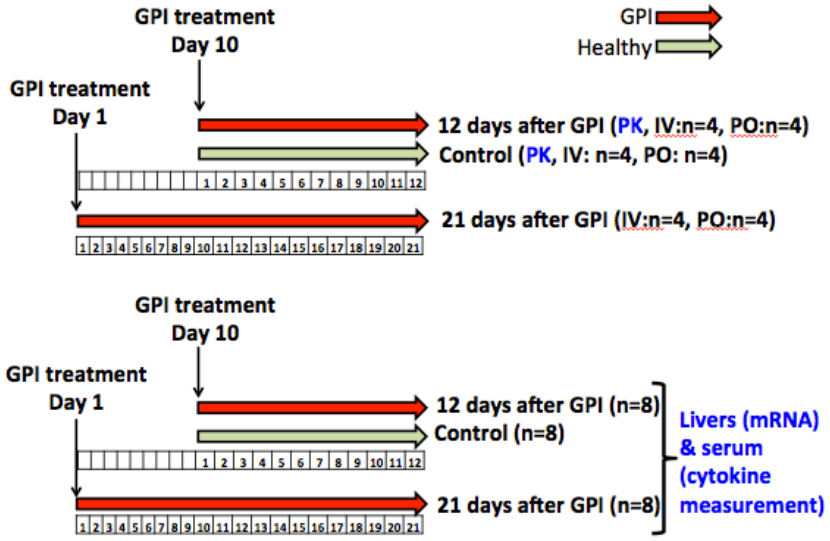

Figure 4.1: Protocol for the pharmacokinetic study

4.2.5 Measurement of fraction unbound in plasma and liver microsomes

The fraction unbound MDZ to the proteins in the plasma and liver microsomes was determined at 37° C using a HT dialysis micro equilibrium device with a 12-14kDa molecular weight cutoff (Gales Ferry, CT) in a stirred 37˚C bath. The microsomal protein concentration was 0.5 mg/mL in phosphate buffer (100 mM, pH 7.4), and the plasma was thawed on the day of use and adjusted to pH 7.4 using phosphoric acid. The samples were collected from both the protein side and buffer side of the membrane after 0 and 4.5 h. The signal for MDZ was monitored by LC-MS/MS with a calibration curve range from 1 to 5000 nM and an acceptable interference peak less than 25% of the lower limit of quantitation. Deviations of less than ±30% were acceptable for the calibration curve samples. Fraction unbound was calculated as a ratio of MDZ concentration in the

buffer and protein chambers. Percent recovery (data not shown) was calculated by dividing the sum of the buffer and protein chambers by the time 0 concentration.

4.2.6 Liquid Chromatography-Mass Spectrometry (LC-MS) analysis of DBS samples

Analysis of MDZ and its metabolites was performed using a previously published protocol with modifications as described (22). Stock solutions of each analyte were combined and serially diluted to produce a range of working solutions, which were used to fortify control mouse blood to yield calibration standards (1 to 10,000 ng/mL). These calibration standards were then spotted onto DBS cards and allowed to dry at room temperature. A 3-mm punch of each study and standard DBS sample was removed and placed in separate wells of 96-well plates, then extracted with a methanol/acetonitrile (1:1, v/v) solution containing internal standards. The resulting extracts were analyzed using an ABSciex API4000 triple quadrupole mass spectrometer LC-MS/MS instrument (Applied Biosystems/MDS; Foster City, CA) run in positive ion mode using a ThermoFisher Betasil C18 2x20-mm 5-micron HPLC column (ThermoFisher Scientific, Waltham, MA) with 0.1% formic acid/water and an acetonitrile gradient to achieve the chromatographic separation. Each compound was detected and quantified with analyte specific selected reaction monitoring (SRM) $(M+H)^+$ transitions (MDZ: *m/z* 326.1>291.2, 1-OH-MDZ: *m/z* 342.1>203.2, 4-OH-MDZ: *m/z* 342.1>234.2, 1-OH-MDZ-glucuronide: *m/z* 518.2>324.1, D_4-MDZ: *m/z* 330.1>295.2, and D_4-1-OH-MDZ: *m/z* 346.1>328.1). The mass spectrometer quadrupoles were tuned to achieve unit resolution (0.7 Da at 50% FWHM) and data were acquired and processed with Analyst 1.4.2 (Applied Biosystems/MDS). The limit of detection was set at 5-fold greater than the noise. The lower limit of quantitation was 5 nM for MDZ, 1-OH-MDZ and 4-OH-MDZ.

4.2.7 LC-MS analysis of the in vitro samples

The *in vitro* metabolism samples were analyzed by LC-MS/MS using an ABSciex QTrap 6500 triple quadrupole mass spectrometer (Applied Biosystems/MDS; Foster City, CA) equipped with a TurboIonSpray interface and operated in a positive ion mode. The analytes were separated using an Ace Ultracore SuperC18 column (2.1x30-mm, 5-micron) with a gradient elution of 5-mM ammonium bicarbonate and acetonitrile. Each compound was detected and quantified by analyte specific SRM $(M+H)^+$ transitions (1-OH-MDZ: *m/z* 342.1>203.0, 4-OH-MDZ: *m/z* 342.1>234.0, and D_4-1-OH-MDZ: *m/z* 346.1>203.0). The mass spectrometer quadrupoles were tuned to achieve unit resolution (0.7 Da at 50% FWHM) and data were acquired and processed with Analyst 1.6 (Applied Biosystems/MDS).

4.2.8 Construction of the Minimal PBPK model

The minimal PBPK model with a 2-compartment PK model was constructed using SimBiology (Matlab R2017a) (Figure 4.4). The mouse physiological parameters obtained from literature (23-26), experimental values and the 2-compartment model estimated parameters (Table 4.4, Table 4.5, and Table 4.6) were used to construct the minimal PBPK model. The volumes of the central and peripheral compartments and rate constants for transfer of MDZ between the central and peripheral compartments were estimated by fitting the healthy-animal IV PK data with the 2-compartment PK model. 'Nonlinear mixed-effects problems' was used as the estimation method for the 2-compartment model fitting. The *in vitro* kinetic data for 1-OH-MDZ and 4-OH-MDZ formation were used in the minimal PBPK model to define the rate of hepatic metabolism, while the literature data were used for the gut metabolism (Table 4.5) (27). In the case of hepatic metabolism, $V_{max\text{-}1\text{-}OH\text{-}MDZ\text{-}Liver}$, $V_{max\text{-}4\text{-}OH\text{-}MDZ\text{-}Liver}$, $K_{m\text{-}1\text{-}OH\text{-}MDZ\text{-}Liver}$ and $K_{m\text{-}4\text{-}OH\text{-}MDZ\text{-}Liver}$ values in both the healthy and the diseased animals were obtained experimentally and a $V_{max\text{-}1\text{-}OH\text{-}MDZ\text{-}Liver\text{-}}$

$_{Healthy}/V_{max\text{-}1\text{-}OH\text{-}MDZ\text{-}Liver\text{-}GPI}$ ratio (0.55) was calculated (Table 4.5). Experimental *in vitro* data were not available for gut metabolism, therefore literature values were used (27). It was assumed that the $V_{max\text{-}1\text{-}OH\text{-}MDZ\text{-}gw\text{-}Healthy}/V_{max\text{-}1\text{-}OH\text{-}MDZ\text{-}gw\text{-}GPI}$ ratio for intestine was same as that for the hepatic metabolism. The values of gut $V_{max\text{-}1\text{-}OH\text{-}MDZ\text{-}gw}$ and $V_{max\text{-}4\text{-}OH\text{-}MDZ\text{-}gw}$ for day 12 GPI mice were calculated using the ratio 0.55. Scaling of $V_{max\text{-}1/4\text{-}OH\text{-}MDZ\text{-}Liver}$ and $V_{max\text{-}1/4\text{-}OH\text{-}MDZ\text{-}gw}$ was done for the entire liver and intestine, respectively so that the values could be used in the minimal PBPK model. A scaling factor of 45 milligrams of liver microsomal protein per gram of mouse liver was used as mentioned in the previous report (28). For the intestinal $V_{max\text{-}1/4\text{-}OH\text{-}MDZ\text{-}gw}$ scaling, 23.6 milligrams of intestinal microsomal protein per gram of intestine was used (29). CYP3A is almost exclusively responsible for metabolism of MDZ to form hydroxylated metabolites (20, 27). However, additional nonCYP3A metabolism in the gut was estimated by fitting the PO healthy animal PK data to the minimal PBPK model. This additional metabolism was defined by $V_{max\text{-}nonCYP3A\text{-}MDZ\text{-}gw}$ and $K_{m\text{-}nonCYP3A\text{-}MDZ\text{-}gw}$ (Table 4.5). Similar to previously mentioned gut $V_{max\text{-}1\text{-}OH\text{-}MDZ\text{-}gw}$ calculations, the ratio of 0.55 was used to calculate $V_{max\text{-}nonCYP3A\text{-}MDZ\text{-}gw}$ for GPI treated mice, while $K_{m\text{-}nonCYP3A\text{-}MDZ\text{-}gw}$ was assumed as constant for the healthy and disease condition. Sensitivity analysis was performed on the model input parameters as shown in Figure 4.2 and Figure 4.3. The model parameters were altered by -100 to +500% of the original values listed in Table 4.4 and Table 4.5.

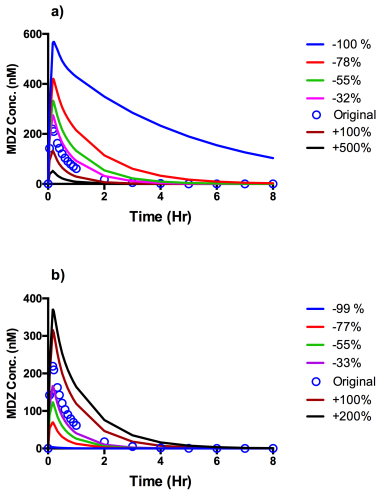

Figure 4.2: Sensitivity analysis for C_{max} after MDZ PO administration.
Effect of altered parameters (a) $V_{max\text{-}1\text{-}OH\text{-}MDZ\text{-}Liver}$ b) $K_{m\text{-}1\text{-}OH\text{-}MDZ\text{-}Liver}$) from approximately -100 to +500% of the healthy animal original value as mentioned in Table 5.

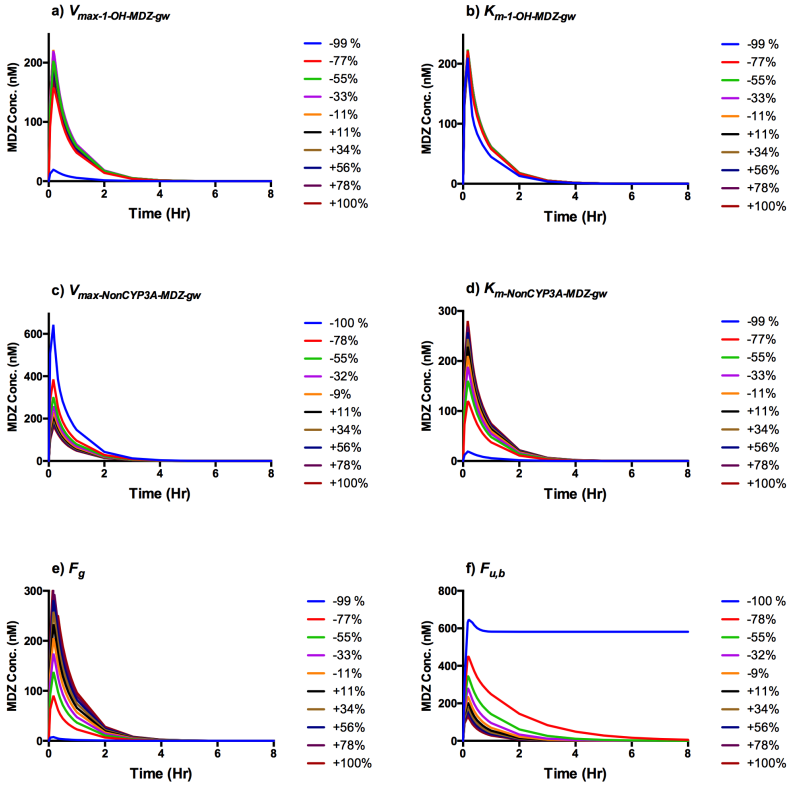

Figure 4.3: Sensitivity annalysis on C_{max} after PO MDZ administration.

Effect of altered parameters from approximately -100 to +100% of the healthy original value as mentioned in Table 4.4 or Table 4.5.

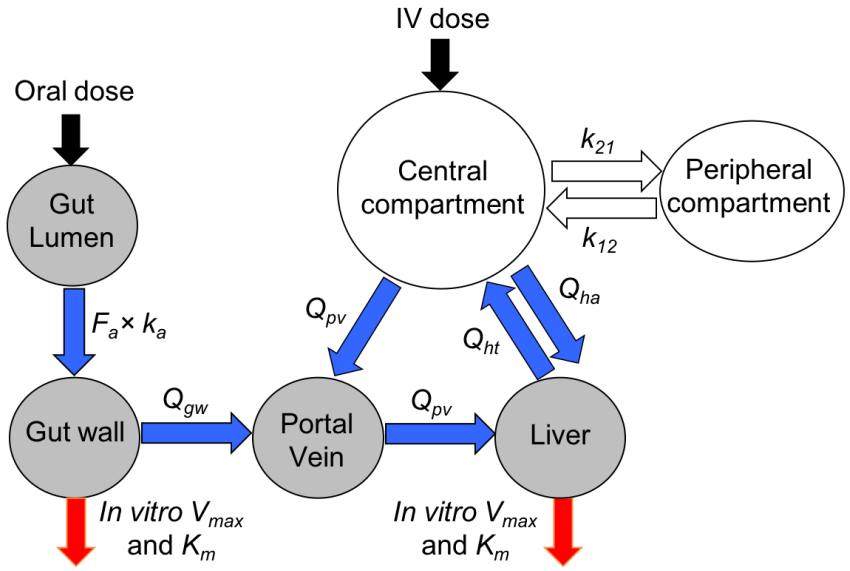

Figure 4.4: Schematic representation of the minimal PBPK model

The minimal PBPK model was adopted from a previously published study by Zhang et al (30). The model can be described by equations 1 to 6 (4.6 Supplementary Information), which were solved by the solver type 'Ordinary differential equations (ODE) 15s' (stiff/NDF). Equation 1 represents absorption of MDZ through the gut lumen. Equation 2 and 5 defines MDZ metabolism in the intestine and liver, respectively. Equation 3 is the 'Well-Stirred' gut model (31), which was used in equation 2 for calculation of fraction unbound in gut ($f_{u,g}$). Equation 4 defines the transit of MDZ from the intestine and central compartment to the portal vein and then to the liver. The transfer of MDZ from the liver to central compartment and further exchange with the peripheral compartment is shown in equation 6. C_{gw}, C_{pv}, C_{liv}, C_{cen}, C_{per} are concentration (nmol/L) of MDZ in gut wall, portal vein, liver, central compartment and peripheral compartment, respectively. A_{gl} is the amount (nmol) of MDZ in the gut lumen compartment. All other parameters in the equations 1 to 6 are mentioned in Table 4.4 and Table 4.5. Assumptions in the minimal PBPK model are described as follows. a) The *in vitro* literature data used to define intestinal metabolism of MDZ

was applicable to the minimal PBPK model (27). b) Suppression of intestinal CYP450 activity due to the GPI-mediated inflammation was same as in the liver. c) The mouse physiological parameters (blood flows, organ volumes) were same for the healthy and GPI treated diseased mice.

4.2.9 Quantitation of serum cytokines

Serum cytokines were quantitated using a mouse proinflammatory multiplex kit (Meso Scale Diagnostics, Rockville, MD) (32). Briefly, serum samples were diluted 2-fold with diluent, and 50 µL of diluted sample was added to each well on a pro-inflammatory panel plate (96-well) and incubated for 2 h at room temperature. After washing 3 times with the wash buffer, 25 µL of detection antibody solution was added per well, followed by an additional 2-h incubation at room temperature. The wells were washed 3 times with the wash buffer, and 150 µL of 2X Read Buffer T was added to each well. The plate was immediately read on a MSD Sector S 600 (Meso Scale Diagnostics, Rockville, MD). Sample concentrations were calculated using calibration curves that were fitted using a 4-parameter logistic model with a $1/Y^2$ weighting. ANOVA was used to establish statistical differences in cytokine levels for the healthy and diseased mice.

4.2.10 RNA isolation and cyp mRNA level detection by quantitative polymerase chain reaction (qPCR)

For each animal, 50-150 mg of frozen liver tissue was homogenized in the presence of 800 µL of Trizol™ (Thermo Fisher Scientific, Waltham, MA) using FastPrep® lysing matrix D beads and the FastPrep®-24 homogenizer (MP Biomedicals, Santa Ana, CA). The homogenate was chilled on ice and was clarified by centrifugation (10,000 x g for 4 minutes). The clarified homogenate was mixed with an equal volume of 100% ethanol, and then processed using the

Direc-Zol™ RNA isolation spin column protocol, including DNAse1 treatment (Zymo Research, Irvin, CA). The concentration and yields of the purified total liver RNA were determined using a Nanodrop™ 8000 spectrophotometer. Then 100 ng of purified RNA was used in a reverse transcription reaction to generate cDNA using TaqMan® High Capacity RNA-to-cDNA Kit (Applied Biosystems, Foster City, CA). The cDNA reaction was diluted 5-fold with sterile water and used for TaqMan® based quantitative PCR analysis for cyp3a11, cyp2c29, and cyp2d26 mRNA targets as well as for the PPIB house-keeping gene mRNA normalizer control. The qPCR data were collected on a 7900HT Real Time PCR instrument (Applied Biosystems). The data were analyzed using ExpressionSuite® software (Thermo Fisher Scientific, Waltham, MA), and cyp target mRNA levels were expressed relative to the PPIB mRNA normalizer control. The unpaired T-test was used to establish statistical differences between day-1 and -12 cyp mRNA levels.

4.2.11 Statistical analysis

Chi square test was used to find association between predicted and observed PK profiles using Excel Chi square test function (33). ANOVA, T-test, Tukey's multiple comparison test were performed using GraphPad Prism 6 (La Jolla, CA). Box-plots for cytokines and cyp-mRNA were plotted using RStudio (Version 1.1.383).

4.3 Results

4.3.1 Effect of GPI-mediated inflammation on the in vitro metabolism of MDZ

The rate of 1-OH-MDZ formation was higher in the MLM prepared from heathy mice as compared to the MLM prepared from GPI-treated mice (Figure 4.5 and Table 4.1). The $V_{max\text{-}1\text{-}OH\text{-}MDZ\text{-}Liver}$ was suppressed by 44% in the diseased mice-MLM as compared to the healthy. The $V_{max\text{-}}$

$_{1\text{-}OH\text{-}MDZ\text{-}Liver}$ was 2.047 (± 0.005) nmol/min/mg in MLM of the healthy mice and 1.143 (± 0.021) nmol/min/mg in MLM of the GPI treated mice (*P* value ≤0.0001). This indicated that the GPI-mediated inflammation suppressed cyp3a11 expression, leading to lower $V_{max\text{-}1\text{-}OH\text{-}MDZ\text{-}Liver}$. However, $K_{m\text{-}1\text{-}OH\text{-}MDZ\text{-}Liver}$ was relatively unchanged (*P* value=0.151) in the MLM prepared from the healthy versus diseased mice. In the case of 4-OH-MDZ, both $V_{max\text{-}4\text{-}OH\text{-}MDZ\text{-}Liver}$ and $K_{m\text{-}4\text{-}OH\text{-}MDZ\text{-}Liver}$ were suppressed with the MLM prepared from the diseased animals as compared to healthy animals (*P value* ≤0.0001) (Figure 4.5 and Table 4.2). The higher $K_{m\text{-}4\text{-}OH\text{-}MDZ\text{-}Liver}$ as compared to $K_{m\text{-}1\text{-}OH\text{-}MDZ\text{-}Liver}$ suggested that 4-OH-MDZ formation is a minor route of metabolism as compared to 1-OH-MDZ (*P* value ≤0.0001). Similar results concluding lower contribution of 4-OH-MDZ as compared to 1-OH-MDZ were reported earlier (13, 15).

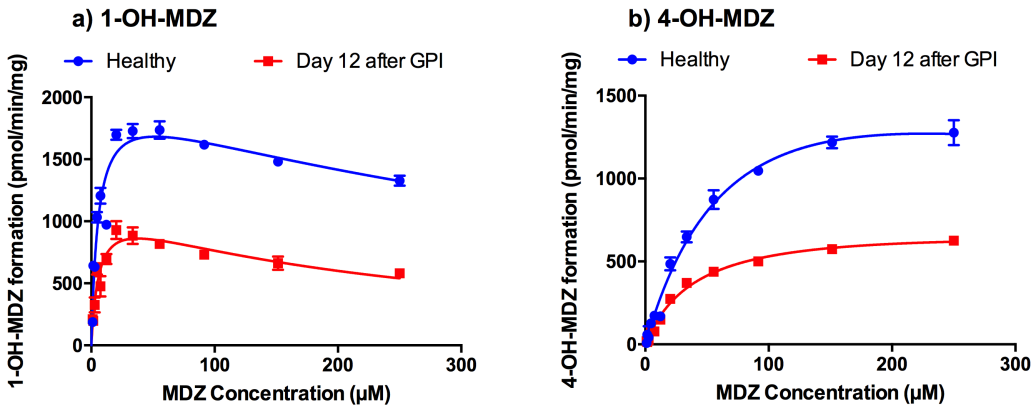

Figure 4.5: Rate of metabolite formation with increasing MDZ concentration in MLM prepared from the healthy and GPI-treated mice a) 1-OH-MDZ and b) 4-OH-MDZ
MLM were prepared using livers collected from the healthy mice and on day 12 after GPI treatment. Lines indicate fitted metabolite formation kinetics. Experimental values are represented as filled circles or squares with standard deviation (n=3).

Table 4.1: Rate of 1-OH-MDZ formation in MLM prepared using livers from the healthy and GPI treated mice (Fitted to substrate inhibition kinetics)

Parameter	Healthy mice	Mice treated with GPI (Day 12)
$V_{max\text{-}1\text{-}OH\text{-}MDZ\text{-}Liver}$ (nmol/min/mg)	2.047 (± 0.005)	1.143 (± 0.021)*
$K_{m\text{-}1\text{-}OH\text{-}MDZ\text{-}Liver}$ (nM)	5630 (±160)	6130 (± 380)$^{\#}$

$K_{i\text{-}1\text{-}OH\text{-}MDZ\text{-}Liver}$ (nM)	478400 (± 16000)	228760 (± 13000)

Each value represents the mean ± standard deviation (n=3)
$V_{max\text{-}1OH\text{-}MDZ\text{-}Liver}$: Maximum rate of metabolic conversion of MDZ to 1-OH-MDZ in liver
$K_{m\text{-}1\text{-}OH\text{-}MDZ\text{-}Liver}$: MDZ concentration corresponding to half of $V_{max\text{-}1OH\text{-}MDZ\text{-}Liver}$
$K_{i\text{-}1\text{-}OH\text{-}MDZ\text{-}Liver}$: Substrate inhibition constant
**Day 12-$V_{max\text{-}1\text{-}OH\text{-}MDZ\text{-}Liver}$ was significantly different than the healthy-$V_{max\text{-}1OH\text{-}MDZ\text{-}Liver}$ (Unpaired T-test with P≤0.0001)*
$^{\#}K_{m\text{-}1\text{-}OH\text{-}MDZ\text{-}Liver}$ were not significantly different (Unpaired T-test with P=0.151)

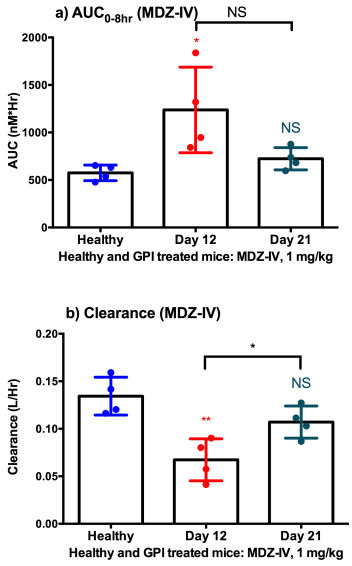

Figure 4.6: Comparison of a) $AUC_{0\text{-}8h}$ and b) clearance of MDZ in healthy and GPI-treated mice after MDZ IV administration (1 mg/kg). *Pharmacokinetic parameters were obtained using NCA and represented as mean and standard deviation. ANOVA and Tukey's test were used for comparison of Day 12 and Day 21 after GPI treatment with healthy mice. (NS: Not significant, *: P≤0.05, **: P≤0.01)*

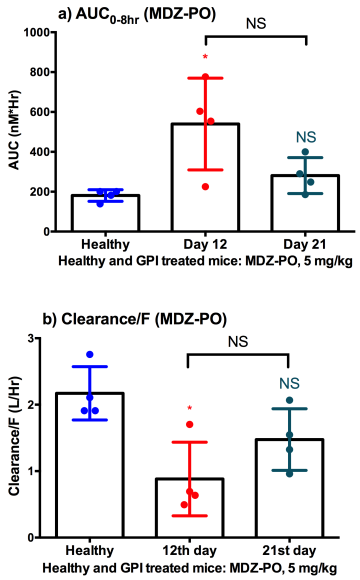

Figure 4.7: Comparison of a) $AUC_{0\text{-}8h}$ and b) Clearance/F of MDZ in healthy and GPI-treated mice after MDZ PO administration (5 mg/kg). *Pharmacokinetic parameters were obtained using NCA and represented as mean and standard deviation. ANOVA and Tukey's test were used for comparison of Day 12 and Day 21 after GPI treatment with healthy mice. (NS: Not significant, *: P≤0.05, **: P≤0.01)*

4.3.2 Pharmacokinetics of MDZ in healthy and GPI-treated mice

In the case of IV dosing, plasma MDZ profiles were available through 2 h for healthy and day 21 GPI mice, while for day 12 mice, plasma MDZ levels were available through 4 h (Figure 4.11). In the case of PO dosing, for day 12 and 21, PK were available through 8 h, while for PO dosing in healthy mice, data were available through 2 h. In the case of PO dosing on day 12, inter-

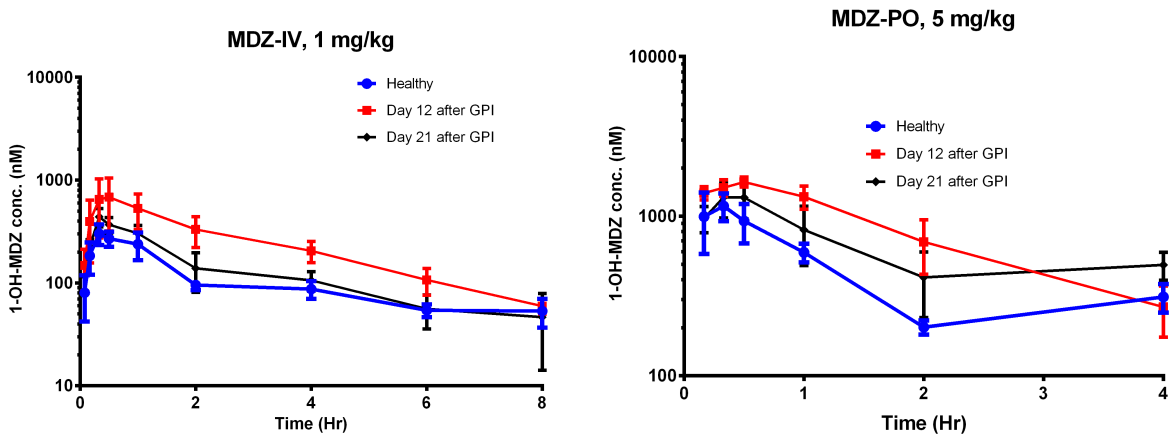

Figure 4.8: Pharmacokinetic profile of 1-OH-MDZ after IV and PO MDZ administration

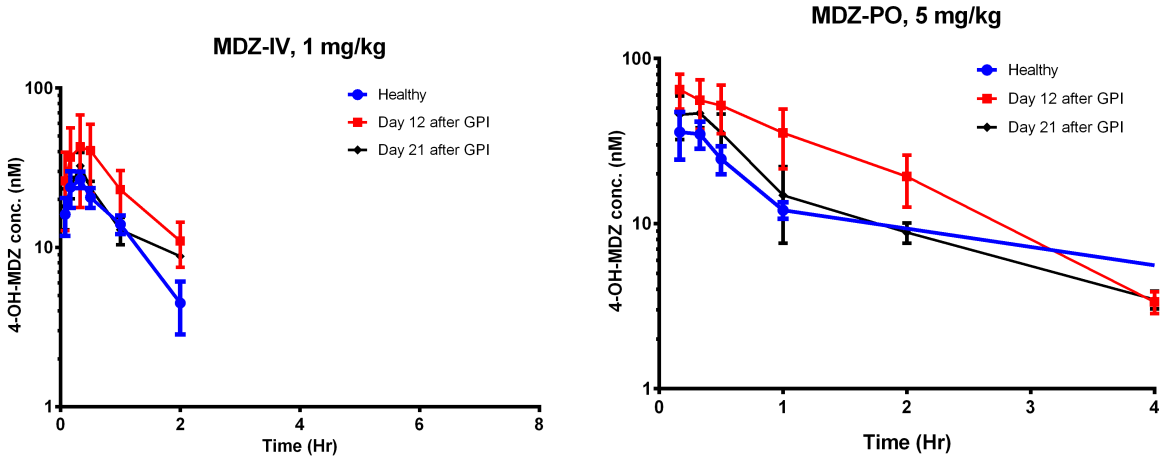

Figure 4.9: Pharmacokinetic profile of 4-OH-MDZ after IV and PO MDZ administration

individual variability in the PK parameters (Table 4.3, Figure 4.6 and Figure 4.7) was high. This inter-individual variability may be due to variability in the IL-6 levels (2700 to 6900 pg/mL) (Figure 4.15) on day 12 leading to differences in the CYP suppression and PK of MDZ. Figure 4.8 and Figure 4.9 describe PK profiles of 1-OH-MDZ and 4-OH-MDZ, respectively after IV and PO MDZ administration. The $AUC_{0\text{-}8h}$ of 1-OH-MDZ after IV and PO administration of MDZ is shown in Figure 4.10. Fraction unbound in plasma ($f_{u,p}$) for both the healthy and diseased states was measured and was same for both of these samples (Table 4.4).

Table 4.2: Rate of 4-OH-MDZ formation in MLM prepared using livers from the healthy and GPI treated mice (Fitted to substrate inhibition kinetics)

Parameter	Healthy mice	Mice treated with GPI (Day 12)
$V_{max\text{-}4\text{-}OH\text{-}MDZ\text{-}Liver}$ (nmol/min/mg)	2.201 (± 0.06)	0.772 (± 0.01)*
$K_{m\text{-}4\text{-}OH\text{-}MDZ\text{-}Liver}$ (nM)	83200 (± 2000)	42490 (± 1000)#
$K_{i\text{-}4\text{-}OH\text{-}MDZ\text{-}Liver}$ (nM)	622500 (± 125000)	3279000 (± 492000)

Each value represents the mean ± standard deviation (n=3)
$V_{max\text{-}4OH\text{-}MDZ\text{-}Liver}$: Maximum rate of metabolic conversion of MDZ to 4-OH-MDZ in liver
$K_{m\text{-}4\text{-}OH\text{-}MDZ\text{-}Liver}$: MDZ concentration corresponding to half of $V_{max\text{-}4OH\text{-}MDZ\text{-}lv}$
$K_{i\text{-}4\text{-}OH\text{-}MDZ\text{-}Liver}$: Substrate inhibition constant
** Day 12-$V_{max\text{-}4\text{-}OH\text{-}MDZ\text{-}Liver}$ was significantly different than the healthy-$V_{max\text{-}4\text{-}OH\text{-}MDZ\text{-}Liver}$ (Unpaired T-test with P≤0.0001)*
 # Day 12-$K_{m\text{-}4\text{-}OH\text{-}MDZ\text{-}Liver}$ was significantly different than the healthy-$K_{m\text{-}4\text{-}OH\text{-}MDZ\text{-}Liver}$ (Unpaired T-test with P≤0.0001)

The IV MDZ clearance decreased by 0.5-fold on day 12 after GPI treatment as compared to the healthy mice (P≤0.05) (Table 4.3 and Figure 4.6). By Day 21, the clearance in GPI-treated mice had still not returned to values observed in the healthy animals, although the differences were not significant (P=0.179). In the case of the PO MDZ administration, the day 12 GPI clearance/F was 0.4-fold lower than that of the healthy mice (P≤0.05) (Figure 4.7).

Table 4.3: Pharmacokinetic parameters after IV and PO administration of MDZ

Route	Parameter	Unit	Healthy mice	GPI-treated mice on day 12	GPI-treated mice on day 21
IV	Dose	mg/kg	1	1	1
	$AUC_{0\text{-}8h}$	nM×h	574 (± 71)	1237 (±389)*	723 (±101)^{NS}
	C_{max}	nM	1260 (± 224)	2493 (±1373)	1289 (±242)
	CL	L/h	0.134 (± 0.017)	0.067 (±0.019)**	0.107 (± 0.014)^{NS}
PO	Dose	mg/kg	5	5	5
	$AUC_{0\text{-}8h}$	nM×h	180 (± 25)	539 (± 199)*	281 (± 78)^{NS}
	T_{max}	h	0.207 (± 0.071)	0.166 (± 0)	0.207 (± 0.071)
	C_{max}	nM	224 (± 75)	662 (± 252)	282 (± 51)
	CL/F	L/h	2.17 (± 0.34)	0.881 (± 0.47)*	1.474 (± 0.4)^{NS}

*The PK parameters were obtained using NCA and represented as mean (standard deviation). ANOVA and Tukey's test were used for comparison of Day 12 and Day 21 after GPI treatment with healthy mice. *: P≤0.05, **: P≤0.01, NS: Not significant*

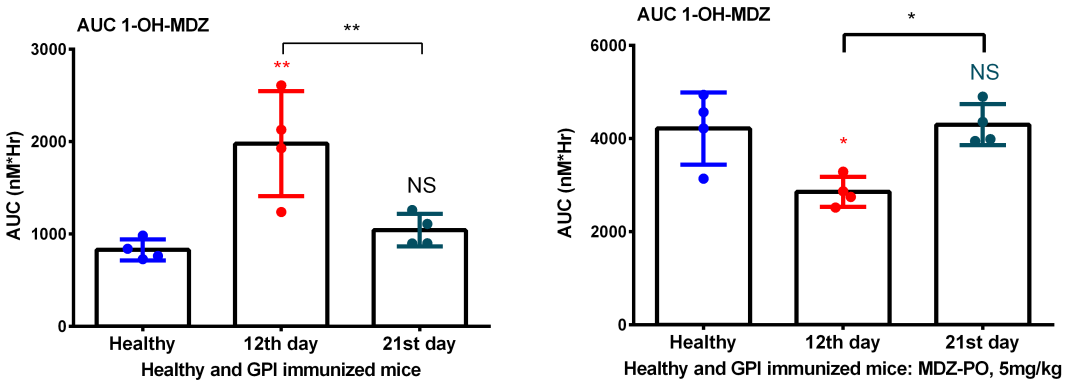

Figure 4.10: Comparison of 1-OH-MDZ $AUC_{0\text{-}8h}$ for healthy and GPI treated mice after MDZ (left side diagram) and PO (right side diagram) administration.
*NS: Not significant, *: P≤0.05, **: P≤0.01 (ANOVA and Tukey's test for comparison of Day 12 and Day 21 with Healthy)*

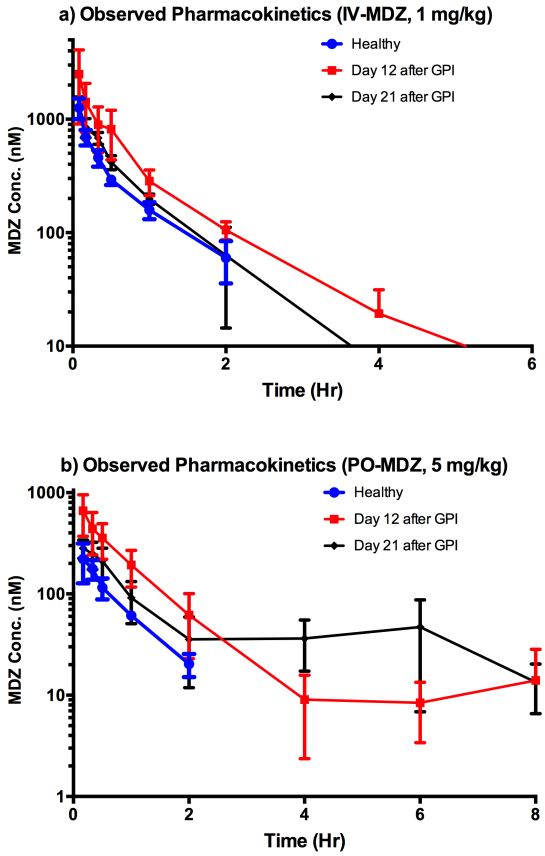

Figure 4.11: Observed pharmacokinetic profiles for a) IV (1 mg/kg) and b) PO (5 mg/kg) MDZ administration Observed MDZ PK represented as filled circles or squares with standard deviation (n=4).

4.3.3 Prediction of MDZ PK in GPI-treated mice using the minimal PBPK model

The Chi square test was used to compare observed PK profile with the predicted profile (Figure 4.14). For IV MDZ dosing, the observed and predicted healthy-animal PK profiles were similar with a Chi square test *p*-value of 0.999. While, day 12 observed and predicted PK profiles were similar with the Chi square test p-value was 0.996. In the case of PO MDZ dosing, predicted and observed profiles in the healthy mice had a Chi square test *p*-value of 0.999, while day 12 PK profiles had Chi square test *p*-value of 0.964. This indicated that the minimal PBPK model successfully predicted the PK after GPI treatment. In addition, $AUC_{0\text{-}8h}$ and clearance values of MDZ showed good agreement between predicted versus observed values for both the IV and PO MDZ administration. The mean observed values of the PK parameters and the 95% confidence interval were compared with the predicted PK parameter values. All the predicted PK parameters resided within the 95% confidence intervals of the observed data (Figure 4.12 and Figure 4.13). In the case of PK predictions after PO dosing on day 12 (Figure 4.14), a visual check showed that the data points after 4 h were not well correlated with the predicted profile. This was due to the lack of good terminal phase for the day 12 PO-PK profile.

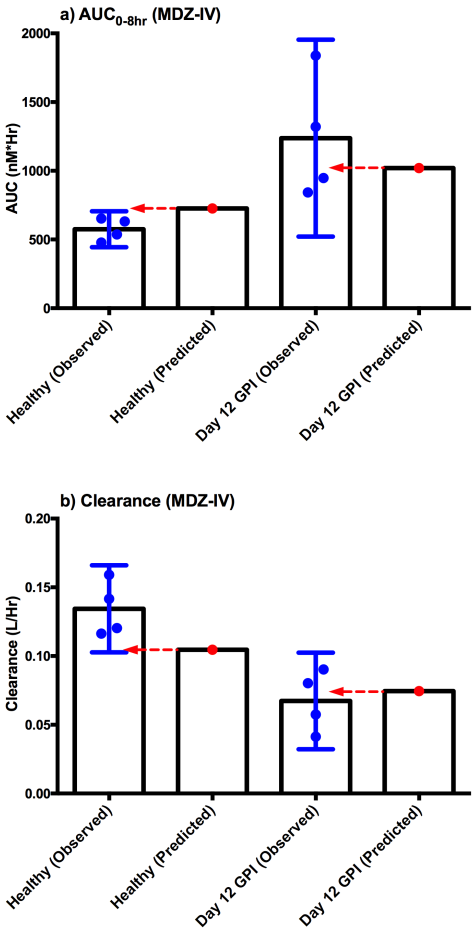

Figure 4.12: Comparison of observed and predicted PK parameters after IV (1 mg/kg) MDZ administration to healthy mice and day 12 after GPI treatment obtained using NCA a) $AUC_{0\text{-}8h}$ and b) Clearance.
Observed values represented as mean and 95% confidence interval. Dashed arrows indicate that the PK parameter predicted by the semi-PBPK model was within the 95% confidence interval of the observed data.

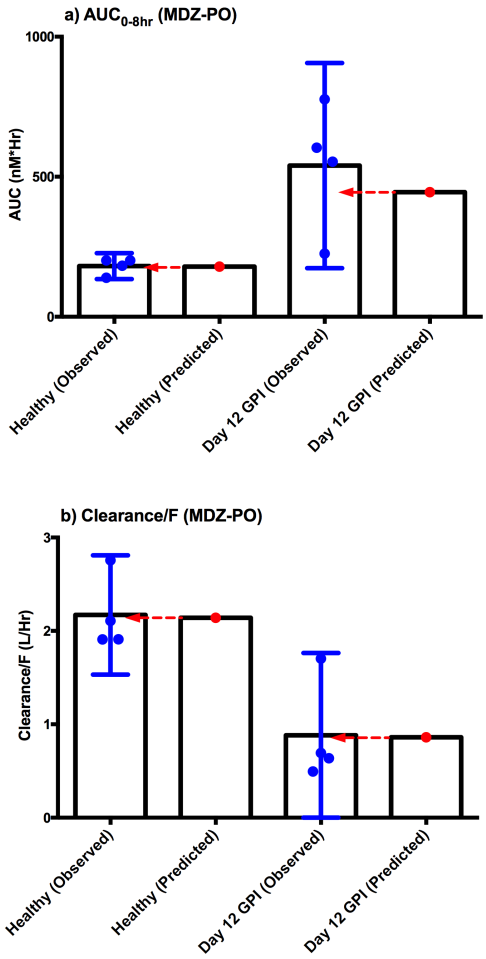

Figure 4.13: Comparison of observed and predicted PK parameters after PO (5 mg/kg) MDZ administration to healthy mice and day 12 after GPI treatment obtained using NCA a) $AUC_{0\text{-}8h}$ and b) Clearance/F.
Observed values represented as mean and 95% confidence interval. Dashed arrows indicate that the PK parameter predicted by the semi-PBPK model was within the 95% confidence interval of the observed data.

4.3.4 Sensitivity analysis

The C_{max} was sensitive to both $V_{max\text{-}1\text{-}OH\text{-}MDZ\text{-}Liver}$ and $K_{m\text{-}1\text{-}OH\text{-}MDZ\text{-}Liver}$ after PO MDZ administration as demonstrated in the Figure 4.2. C_{max} decreased with increasing $V_{max\text{-}1\text{-}OH\text{-}MDZ\text{-}Liver}$, while increased with increasing $K_{m\text{-}1\text{-}OH\text{-}MDZ\text{-}Liver}$. In addition, altered values of $V_{max\text{-}1\text{-}OH\text{-}MDZ\text{-}gw}$,

$V_{max\text{-}NonCYP3A\text{-}MDZ\text{-}gw}$, $K_{m\text{-}NonCYP3A\text{-}MDZ\text{-}gw}$, F_g and $F_{u,b}$ lead to changes in C_{max} and overall PK profile of MDZ after PO dosing as shown in the Figure 4.3.

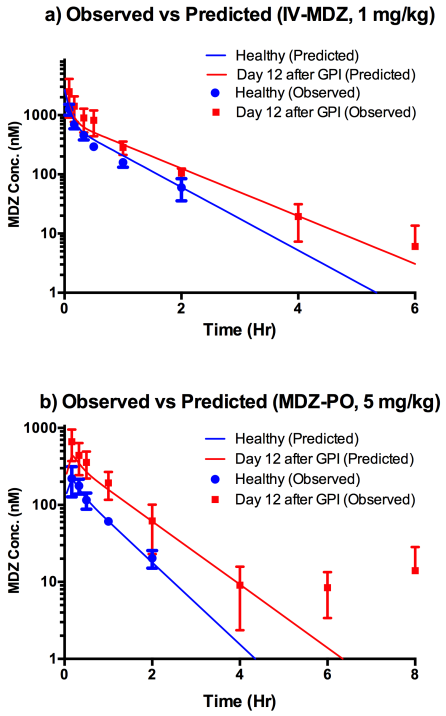

Figure 4.14: Observed and the model predicted PK profiles for a) IV (1 mg/kg) and b) PO (5 mg/kg) The observed values represented as mean and standard deviation.

Table 4.4: MDZ related and mouse physiological parameters used in the semi-PBPK model

Parameter	Values	Source/reference
V_c (Volume of the central compartment)	0.028 L	Estimated*
V_{per} (Volume of the peripheral compartment)	0.0411 L	Estimated*
k_{12} (Rate constant for MDZ transfer from the central to peripheral compartment)	6.3944 1/h	Estimated*
k_{21} (Rate constant for MDZ transfer from the peripheral to central compartment)	4.3540 1/h	Estimated*
k_a (Rate of absorption from the gut lumen to the gut wall)	6.2241 1/h	Estimated[#]
F_a (Fraction of the dose absorbed from the gut lumen)	1	Kuze et al-2009 (21)
F_g (Fraction escaped from the gut wall metabolism)	0.091	Kuze et al-2009 (21)
$f_{u,mic}$ (Fraction unbound in the mouse liver microsomes)[a]	0.613	Experimental data

B/P ratio	0.813	Cleton et al (34)
$f_{u,b}$	0.1008	Calculated using $f_{u,p}$ and B/P ratio
$f_{u,p}$ *(Healthy mice)*	0.082	Experimental data
$f_{u,p}$ *(Day 12 after GPI treatment in mice)*	0.083	Experimental data
Q_{ha} *(Hepatic artery blood flow)*	0.786 mL/min	Davies and Morris (23), Brown et al (24)
Q_{ht} *(Total hepatic blood flow)*	3.15 mL/min	Davies and Morris (23), Brown et al (24)
Q_{pv} *(Portal vein blood flow)*	2.36 mL/min	Davies and Morris (23), Brown et al (24)
Q_{gw} *(Gut wall blood flow)*	1.5 mL/min	Davies and Morris (23)

**Estimated by fitting the experimental IV healthy animal PK data to the 2-compartment PK model. The PK data after 2 h was not included as it was below the limit of quantitation.*
[#]Estimated by fitting the experimental PO healthy animal PK data to the 2-compartment PK model. The PK data after 4 h was not included as it was below the limit of quantitation.
[a]$f_{u,mic}$ was used to correct the K_m obtained from in vitro experiment ($K_{m\text{-}Cor}=K_m \times f_{u,mic}$)
$f_{u,b}$: Fraction unbound in blood, B/P ratio: Blood to Plasma ratio, $f_{u,p}$: Fraction unbound in plasma

Table 4.5: Model parameters for hepatic and intestinal metabolism of MDZ obtained from the in vitro experiments, literature or estimated using the semi-PBPK model

Parameter (units)	**Values**		**Source/reference**
	Healthy*	Day 12*	
$V_{max\text{-}1\text{-}OH\text{-}MDZ\text{-}Liver}$ *(nmol/h/total liver)*	7545	4216	Experimental *in vitro* data scaled for mouse liver[a]
$K_{m\text{-}1\text{-}OH\text{-}MDZ\text{-}Liver\text{-}Cor}$ *(nmol/L)*[b]	3432	3739	Experimental *in vitro* data
$V_{max\text{-}4\text{-}OH\text{-}MDZ\text{-}Liver}$ *(nmol/h/total liver)*	8137	2855	Experimental *in vitro* data scaled for mouse liver
$K_{m\text{-}4\text{-}OH\text{-}MDZ\text{-}Liver\text{-}Cor}$ *(nmol/L)*[b]	51001	25991	Experimental *in vitro* data
$\frac{V_{max}\ (Day\ 12)}{V_{max}\ (Healthy)}$	0.55		Calculated using $V_{max\text{-}1\text{-}OH\text{-}MDZ\text{-}Liver}$
$V_{max\text{-}1\text{-}OH\text{-}MDZ\text{-}gw}$ *(nmol/h/total intestine)*[a,c]	877	482[d]	Kuze et al-2013 (27)
$K_{m\text{-}1\text{-}OH\text{-}MDZ\text{-}gw\text{-}Cor}$ *(nmol/L)*[e]	735.6	735.6	Kuze et al-2013 (27)
$V_{max\text{-}4\text{-}OH\text{-}MDZ\text{-}gw}$ *(nmol/h/total intestine)*[a,c]	168	92.4[d]	Kuze et al-2013 (27)
$K_{m\text{-}4\text{-}OH\text{-}MDZ\text{-}gw\text{-}Cor}$ *(nmol/L)*[e]	7846	7846	Kuze et al-2013 (27)
$V_{max\text{-}nonCYP3A\text{-}MDZ\text{-}gw}$ *(nmol/h/total intestine)*	5931	3262[d]	Estimated[f]
$K_{m\text{-}nonCYP3A\text{-}MDZ\text{-}gw}$ *(nmol/L)*	51571	51571	Estimated[f]

**Values are for the healthy mice or day 12 after GPI treatment to mice*
[a]Scaling of the in vitro kinetics data was done as reported by Barter et al (28)
[b] $K_{m\text{-}1/4\text{-}OH\text{-}MDZ\text{-}gw\text{-}Cor}$ was calculated using formula $K_{m\text{-}1/4\text{-}OH\text{-}MDZ\text{-}gw\text{-}Cor}=K_m \times f_{u,mic}$ (35)
[c]23.6 milligrams of intestinal microsomal protein per gram of intestine (29)
[d]The ratio of 0.55 was used to calculate $V_{max\text{-}1OH\text{-}MDZ\text{-}gw}$ for day 12 after GPI treatment
[e]Assumed unchanged for the healthy mice and day 12 after GPI treatment. Corrected using $f_{u,mic}$

V_{max}: Maximum rate of metabolic conversion of MDZ to either 1-OH-MDZ or 4-OH-MDZ in liver or intestine
K_m: Michaelis-Menten constant representing concentration of MDZ when the rate of metabolism is half the maximum value
[f]Estimated using the semi-PBPK model for the healthy mice.

Table 4.6: Mouse physiological and MDZ related parameters

Parameter	Value	Reference
V_{gl} (Volume of the gut lumen)	1.13 mL	Kirman et al (25)
V_{gw} (Volume of the gut wall)	1.1 mL	Kirman et al (25)
V_{pv} (Volume of the portal vein) (Assumed to be same as that of rat)	0.55 mL	Masyuk et al (26)
V_{liv} (Volume of liver)	1.37 mL	Brown et al (24)
F (Oral bioavailability as a fraction)	0.06206	Calculated

4.3.5 Effect of GPI-mediated inflammation on serum cytokine levels

The cytokine levels peaked on day 12 according to previous experiments (data not shown). In this study, the healthy mice had lower cytokine levels as compared to the day 12 GPI treated mice (Figure 4.15). Since inflammation in this model remits over time (data not shown), the cytokine levels returned to the normal range by day 21, but did not full return to the pre-study levels. Serum levels of various other cytokines (IL-2, IL-1β, IL-10, IFN-γ) were not significantly elevated on day 12 after GPI treatment (data not shown). IL-6 levels in the GPI-treated mice on day 12 were approximately 100-fold higher than that in the healthy mice ($P \leq 0.0001$). In addition, day 12 IL-6 levels were 5.4-fold higher than that on day 21 ($P \leq 0.0001$). However, healthy animal and day 21 IL-6 levels were not significantly different. Serum TNF-α levels were 2.6-fold higher in diseased animals on day 12 as compared to levels in the healthy mice ($P \leq 0.0001$). Day 12 TNF-α levels were also higher (1.3-fold) than levels on day 21 ($P \leq 0.01$). In the case of TNF-α, day 21 levels were 1.9-fold higher than healthy ($P \leq 0.0001$).

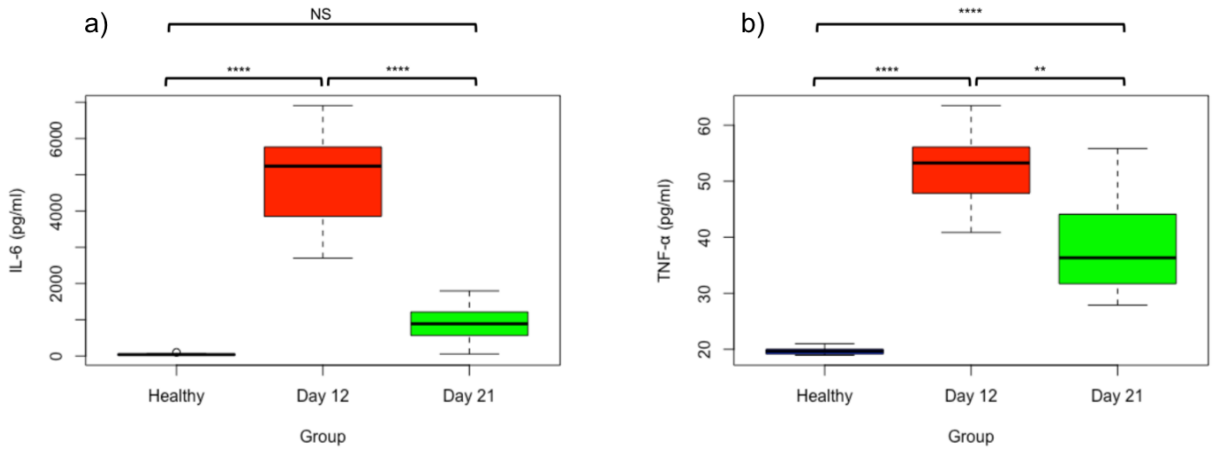

Figure 4.15: Box-plot representation of the serum cytokine levels and statistical comparison for the healthy mice, day 12 and day 21 after GPI treatment to mice. a) IL-6 and b) TNF-α.
Box-plot showing first and third quartiles, mean and range. NS: Not significant, ****: P≤0.0001, **: P≤0.01 (ANOVA and Tukey's test).

4.3.6 Effect of GPI-mediated inflammation on liver cyp3a11, cyp2c29 and cyp2d26 mRNA

The mRNA levels of cyp3a11, cyp2c29, and cyp2d26 were normalized to the house-keeping gene PPIB (Figure 4.16). Cyp2c66 mRNA was not found in this study, while cyp2c29 had the highest basal levels of mRNA expression followed by cyp3a11 and cyp2d26. The responses of cyp3a11 and cyp2c29 to GPI-mediated inflammation were similar. The mRNA levels were highest on day 1 after GPI treatment, followed by a reduction in levels on day 5, and 12 as compared to the baseline levels. However, in the case of cyp3a11 and cyp2c29, day 8 showed surprisingly increased mRNA levels. On day 15, mRNA levels appeared to increase but did not return to the baseline levels. The reduction of mRNA levels was notably highest on day 5. Cyp3a11 mRNA on day 12 was suppressed by around 89% after the GPI treatment. On day 12, cyp2c29 and cyp2d26 mRNA were suppressed by around 85% and 51%, respectively as compared to the day 1 levels.

4.4 Discussion

In this study, the *in vitro* metabolism and PK of MDZ was studied to demonstrate suppression of the CYP activity in the GPI-treated animals, and a minimal PBPK model was

generated using *in vitro* data from both the healthy and diseased animals. It was assumed that the 2-compartment IV parameters of the healthy and diseased mice were same. Therefore, the IV-PK data from the healthy mice were used to generate the 2-compartmental parameters for both of the groups. The 2-comparment model parameters for the disease-animal IV data were also available and used for the model prediction (data not shown). However, this did not change the results significantly.

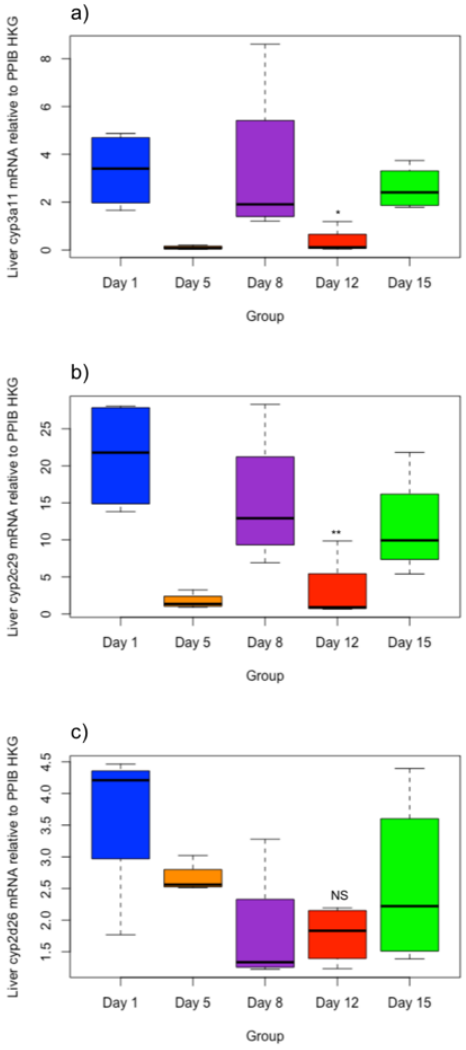

Figure 4.16: Box-plot representation of a) cyp3a11, b) cyp2c29 and c) cyp2d26 mRNA levels in mouse livers on day 1, 5, 8, 12, and 15 after GPI treatment. Box-plot showing first and third quartiles, mean and range. NS: Not significant, *: P≤0.05, **: P≤0.01 (Unpaired T-test was used to compare mRNA levels on day 1 and day 12).

The GPI mouse model is frequently used to induce arthritis and study the anti-inflammatory activity of NCEs in the drug discovery process (9). In this study, the GPI-mediated inflammation increased serum proinflammatory cytokine levels in the DBA/1 mice. This result was in agreement with the previously published report (8). Several published *in vitro* and *in vivo* models of inflammation showed that increased cytokines can lead to reduced CYP expression (10, 11, 36).

The GPI model showed highest degree of inflammation approximately on the day 12 and the

inflammation decreased afterwards (data not shown). Therefore, the day 8-CYP mRNA levels should be lower as compared to the day 1-levels based on the disease state. Current study shows that the mean cyp3a11 and cyp2c29 mRNA levels on day 8 were surprisingly higher as compared to the day 5 and 12 (Figure 4.16). However, the day 8-cyp3a11 mRNA levels were not significantly different when compared to the day 5 ($p=0.1$) and day 12 ($p=0.13$). In the case of cyp2c29 mRNA, day 8 and day 12 levels were not significantly different ($p=0.054$), however, the day 8 mRNA levels were significantly higher ($p=0.026$) than the day 5 (Unpaired T-test). Although the day 8 mRNA levels could not be completely explained, day 12 data were more important for the comparison. Because, CYP mRNA and cytokine levels, *in vitro* metabolism and PK for day 12 after GPI treatment were available for day 12 after GPI treatment. Therefore, the conclusions were based on the day 12 data.

The IL-6 and TNF-α proinflammatory cytokine levels increased on day 12 after GPI treatment. Cyp3a11 levels decreased on day 5 and 12 after GPI treatment. The reduction in $V_{max\text{-}1OH\text{-}MDZ\text{-}Liver}$ ($P \leq 0.0001$) indicated that the CYP activity was suppressed. In this report, the GPI-mediated inflammation was studied based on increased cytokines, decreased CYP mRNAs, decreased *in vitro* metabolism, and decreased clearance of MDZ. The experimental data may be useful for future experiments with GPI-mediated mouse model of inflammation. Another *in vitro* study using human hepatocytes showed that IL-6 was responsible for suppression of various CYP-mRNA, including CYP3A4. In addition, activities of CYP3A4 and CYP1A2 were also suppressed (37). This suppression of CYPs may lead to alteration of PK of its substrates. Machavaram et al used the *in vitro* data of IL-6-mediated CYP suppression in the PBPK model for prediction of disease-drug interactions involving elevated cytokine levels. As mentioned previously, serum cytokine levels are increased in the inflammatory diseases. Although this elevation of cytokines in

the patient population is highly variable and dependent on the disease stage, age, and sleep deprivation; it can still impact expression of CYPs (38). In addition, cytokine levels are altered due to administration of various therapeutic proteins. For example, blinatumomab, a bispecific antibody against CD19, increased cytokines (particularly IL-6 and IL-10) to maximum levels, about six hours after administration (6). However, adalimumab, an anti-TNF-α antibody, resulted in reduced levels of pro-inflammatory cytokines (TNF-α and IL-6) (39). Since elevated or reduced cytokine levels can alter the expression of different CYPs, these biologics have the potential to change the PK of the small molecule drugs that are metabolized by the CYPs, resulting in therapeutic protein-drug interactions (40).

Effect of alteration of the model parameters (V_{max}, K_m, F_g, $F_{u,b}$) on the PK profile was studied (Figure 4.2 and Figure 4.3). C_{max} and AUC (data not shown) were the major PK parameter sensitive to the change in various model parameters. This indicates that the tested model parameters defined metabolism of MDZ in the liver and intestine and alteration of the values from the original parameter value may impact PK prediction of MDZ.

Plasma protein binding of MDZ is around 95%. Furthermore, the fraction unbound of MDZ was constant even with changing plasma drug concentration as reported earlier (41). Alteration of plasma proteins may have a significant impact on MDZ clearance assuming that the only unbound fraction of MDZ can be metabolized by CYP450 enzymes. A protein binding study with human serum albumin and α-1-acid glycoprotein solutions showed that MDZ was extensively bound to both (42). Glycosylation of α-1-acid glycoprotein was changed in patients with rheumatoid arthritis (43). These structural changes in the protein may lead to altered binding with drugs. In another report, plasma albumin levels decreased in patients with the inflammatory disease (arthritis). In addition, α-1-acid glycoprotein level increased in the arthritis patients as compared

to the healthy control group. The authors also reported changes in the plasma protein binding of propranolol and chlorpromazine in the arthritis patients to establish correlation between changes in plasma protein levels and protein binding of the drugs (44). Therefore, it was pertinent to investigate MDZ protein binding in healthy and GPI-treated mice with inflammation. However, MDZ plasma protein binding was same for the healthy and diseased animals (Table 4.4). This eliminated the possibility of altered plasma protein levels contributing to differences in clearance for the healthy and diseased mice.

The 'Well-Stirred' model (equation 3) of gut (31) was used to calculate $f_{u,g}$ using literature values of Q_{gw}, $V_{max\text{-}1\text{-}OH\text{-}MDZ\text{-}gw}$, $K_{m\text{-}1\text{-}OH\text{-}MDZ\text{-}gw}$ and F_g (Table 4.4 and Table 4.5). After PO administration, MDZ is well absorbed (F_a=1) (21). Therefore, low bioavailability (F=0.062) of MDZ after PO administration may be attributed to the intestinal metabolism. As mentioned in the previous section, *in vitro* data were not available to define metabolism in the intestines, and hence literature values were used instead (27). In addition, non-CYP3A metabolism of MDZ was defined by the parameters ($V_{max\text{-}nonCYP3A\text{-}MDZ\text{-}gw}$ and $K_{m\text{-}nonCYP3A\text{-}MDZ\text{-}gw}$) estimated using the minimal PBPK model and healthy-animal PK data.

The 1-OH-MDZ and 4-OH-MDZ are important metabolites of MDZ (13, 15). In a mass balance study in humans using radioactive MDZ, 60-70% of administered dose was eliminated via renal route as 1-OH-MDZ-glucuronide, while 4-OH-MDZ and 1,4-diOH-MDZ were ~3 and ~1%, respectively. Urinary excretion of unchanged MDZ was negligible (45). Another study used rats to show that 81% of the administered dose was recovered in the feces, while 10% was recovered in the urine (46). In addition, urinary excretion of MDZ had <1% contribution according to a clinical study (47). Therefore, in this study, renal clearance of MDZ was excluded from the model. The model substrate MDZ, is mainly cleared via hepatic metabolism. For other drugs with

minimum or no hepatic metabolism where renal elimination is a major route of clearance, the minimal PBPK model may not be appropriate or may need modifications to account for non-hepatic metabolism and renal elimination. In addition, the model would require PK data generated in the healthy animals and hepatic *in vitro* microsomal metabolism data obtained using both the healthy and diseased mice.

Overall, the model successfully predicted MDZ PK in the disease condition. The model may be useful to predict PK of other CYP substrates in the mice with GPI-mediated inflammation. In the drug discovery process, dose selection for the preclinical disease models is usually done using PK data in the healthy animals. The healthy animal PK data may not accurately predict the impact of inflammation or other diseases on the PK of NCEs. The minimal PBPK model may be useful to predict doses for achieving targeted exposure during GPI-mediated inflammation. The model and *in vitro* data were used to demonstrate this approach of PK prediction. However, the proposed framework of the minimal PBPK model may also be extended to other inflammation models and disease conditions, provided availability of minimal healthy animal PK and *in vitro* metabolism data that assumes clearance via CYPs.

4.5 Conclusion

The *in vitro* hepatic metabolism, and PK of MDZ were studied during the GPI-mediated inflammation in mice. In addition, serum cytokine levels and hepatic CYP mRNA during GPI-mediated inflammation were examined. The minimal PBPK model predicted PK of MDZ in the diseased state. The model may be used to select doses for mice with GPI-mediated inflammation in order to achieve targeted exposure by correcting for suppression of metabolism due to

inflammation. This model may also be used for PK prediction of other drugs after GPI-mediated inflammation.

4.6 Supplementary Information

Model equations

$$\left(\frac{dA_{gl}}{dt}\right) = -(F_a \times k_a \times A_{gl}) \quad (1)$$

$$V_{gw}\left(\frac{dC_{gw}}{dt}\right) = \left(F_a \times k_a \times A_{gl}\right) - (Q_{gw} \times C_{gw}) - (C_{gw} \times f_{u,g} \times (\left(\frac{V_{\max-1-\mathrm{OH}-\mathrm{MDZ}-\mathrm{gw}}}{K_{m-1-OH-MDZ-gw} + \left(f_{u,g} \times C_{gw}\right)}\right) + \left(\frac{V_{\max-4-\mathrm{OH}-\mathrm{MDZ}-\mathrm{gw}}}{K_{m-4-OH-MDZ-gw} + \left(f_{u,g} \times C_{gw}\right)}\right) + \left(\frac{V_{\max-\mathrm{nonCYP3A}-\mathrm{MDZ}-\mathrm{gw}}}{K_{m-nonCYP3A-MDZ-gw} + \left(f_{u,g} \times C_{gw}\right)}\right)) \quad (2)$$

$$F_g = \left(\frac{Q_{gw}}{Q_{gw} + \left(f_{u,g} \times (\frac{V_{\max-1-\mathrm{OH}-\mathrm{MDZ}-\mathrm{gw}}}{K_{m-1-OH-MDZ-gw} + C_{gw}})\right)}\right) \quad (3)$$

$$V_{pv}\left(\frac{dC_{pv}}{dt}\right) = (Q_{gw} \times C_{gw}) - \left(Q_{pv} \times C_{pv}\right) + (Q_{pv} \times C_{cen}) \quad (4)$$

$$V_{liv}\left(\frac{dC_{liv}}{dt}\right) = \left(Q_{pv} \times C_{pv}\right) - \left(Q_{ht} \times C_{liv}\right) + \left(Q_{ha} \times C_{cen}\right) - \left(C_{liv} \times f_{u,b}\right) \times \left(\left(\frac{V_{\max-1-\mathrm{OH}-\mathrm{MDZ}-\mathrm{Liver}}}{K_{m-1-OH-MDZ-Liver} + \left(C_{liv} \times f_{u,b}\right)}\right) + \left(\frac{V_{\max-4-\mathrm{OH}-\mathrm{MDZ}-\mathrm{Liver}}}{K_{m-4-OH-MDZ-Liver} + \left(C_{liv} \times f_{u,b}\right)}\right)\right) \quad (5)$$

$$V_{cen}\left(\frac{dC_{cen}}{dt}\right) = -\left(Q_{pv} \times C_{cen}\right) + \left(Q_{ht} \times C_{liv}\right) - \left(Q_{ha} \times C_{cen}\right) - \left(k_{12} \times C_{cen}\right) + \left(k_{21} \times C_{per}\right) \quad (6)$$

Glossary

Parameter	Definition
A_{gl}	*Amount of MDZ in the gut lumen compartment*
F_a	*Fraction of the dose absorbed from the gut lumen*
k_a	*Rate of absorption from the gut lumen to the gut wall*
V_{gw}	*Volume of the gut wall*
V_{pv}	*Volume of the portal vein*
V_{liv}	*Volume of liver*
V_{cen}	*Volume of the central compartment*
C_{gw}	*Concentration of MDZ in gut wall*
C_{pv}	*Concentration of MDZ in portal vein*
C_{cen}	*Concentration of MDZ in central compartment*
C_{liv}	*Concentration of MDZ in liver*
C_{per}	*Concentration of MDZ in peripheral compartment*
Q_{gw}	*Gut wall blood flow*
Q_{pv}	*Portal vein blood flow*
Q_{ht}	*Total hepatic blood flow*
Q_{ha}	*Hepatic artery blood flow*
k_{12}	*Rate constant for MDZ transfer from the central to peripheral compartment*
k_{21}	*Rate constant for MDZ transfer from the peripheral to central compartment*
F_g	*Fraction escaped from the gut wall metabolism*
$f_{u,g}$	*Fraction unbound in gut*
$f_{u,b}$	*Fraction unbound in blood*

$V_{max-1-OH-MDZ-gw}$	*Maximum rate of metabolic conversion of MDZ to 1-OH-MDZ in gut wall*
$K_{m-1-OH-MDZ-gw}$	*Michaelis-Menten constant representing concentration of MDZ when the rate of 1-OH-MDZ formation is half the maximum value in gut wall*
$V_{max-4-OH-MDZ-gw}$	*Maximum rate of metabolic conversion of MDZ to 4-OH-MDZ in gut wall*
$K_{m-4-OH-MDZ-gw}$	*Michaelis-Menten constant representing concentration of MDZ when the rate of 4-OH-MDZ formation is half the maximum value in gut wall*
$V_{max-nonCYP3A-MDZ-gw}$	*Maximum rate of metabolic conversion of MDZ for additional nonCYP3A metabolism*
$K_{m-nonCYP3A-MDZ-gw}$	*Michaelis-Menten constant representing concentration of MDZ when the rate of nonCYP3A metabolism is half the maximum value in gut wall*
$V_{max-1-OH-MDZ-Liver}$	*Maximum rate of metabolic conversion of MDZ to 1-OH-MDZ in liver*
$K_{m-1-OH-MDZ-Liver}$	*Michaelis-Menten constant representing concentration of MDZ when the rate of 1-OH-MDZ formation is half the maximum value in liver*
$V_{max-4-OH-MDZ-Liver}$	*Maximum rate of metabolic conversion of MDZ to 4-OH-MDZ in liver*
$K_{m-4-OH-MDZ-Liver}$	*Michaelis-Menten constant representing concentration of MDZ when the rate of 4-OH-MDZ formation is half the maximum value in liver*

4.7 References

1. Morgan E. Impact of infectious and inflammatory disease on cytochrome P450–mediated drug metabolism and pharmacokinetics. Clin Pharmacol Ther. 2009;85(4):434-438
2. Frye RF, Schneider VM, Frye CS, Feldman AM. Plasma levels of TNF-α and IL-6 are inversely related to cytochrome P450-dependent drug metabolism in patients with congestive heart failure. J Card Fail. 2002;8(5):315-319
3. Coutant D, Kulanthaivel P, Turner P, Bell R, Baldwin J, Wijayawardana S, Pitou C, Hall S. Understanding Disease–Drug Interactions in Cancer Patients: Implications for Dosing Within the Therapeutic Window. Clin Pharmacol Ther. 2015;98(1):76-86
4. Robertson G, Liddle C, Clarke S. Inflammation and Altered Drug Clearance in Cancer: Transcriptional Repression of a Human CYP3A4 Transgene in Tumor-bearing Mice. Clin Pharmacol Ther. 2008;83(6):894-897
5. Aitken AE, Morgan ET. Gene-specific effects of inflammatory cytokines on cytochrome P450 2C, 2B6 and 3A4 mRNA levels in human hepatocytes. Drug Metab Disposition. 2007;35(9):1687-1693
6. Xu Y, Hijazi Y, Wolf A, Wu B, Sun YN, Zhu M. Physiologically Based Pharmacokinetic Model to Assess the Influence of Blinatumomab-Mediated Cytokine Elevations on Cytochrome P450 Enzyme Activity. CPT Pharmacometrics Syst Pharmacol. 2015;4(9):507-515

7. Martignoni M, Groothuis GM, de Kanter R. Species differences between mouse, rat, dog, monkey and human CYP-mediated drug metabolism, inhibition and induction. Expert Opin Drug Metab Toxicol. 2006;2(6):875-894
8. Matsumoto I, Zhang H, Yasukochi T, Iwanami K, Tanaka Y, Inoue A, Goto D, Ito S, Tsutsumi A, Sumida T. Therapeutic effects of antibodies to tumor necrosis factor-alpha, interleukin-6 and cytotoxic T-lymphocyte antigen 4 immunoglobulin in mice with glucose-6-phosphate isomerase induced arthritis. Arthritis Res Ther. 2008;10(3):R66
9. Palmqvist N, Siller M, Klint C, Sjödin A. A human and animal model-based approach to investigating the anti-inflammatory profile and potential of the 5-HT 2B receptor antagonist AM1030. J Inflamm. 2016;13(1):20
10. Gandhi A, Guo T, Shah P, Moorthy B, Chow DL, Hu M, Ghose R. CYP3A-dependent drug metabolism is reduced in bacterial inflammation in mice. Br J Pharmacol. 2012;166(7):2176-2187
11. Kato R, Yamashita S, Moriguchi J, Nakagawa M, Tsukura Y, Uchida K, Amano F, Hirotani Y, Ijiri Y, Tanaka K. Changes of midazolam pharmacokinetics in Wistar rats treated with lipopolysaccharide: relationship between total CYP and CYP3A2. Innate Immun. 2008;14(5):291-297
12. Kajikawa N, Doi M, Kusaba J-i, Aiba T. Effect of carrageenan-induced acute peripheral inflammation on the pharmacokinetics and hepatic metabolism of midazolam in rats. Drug Metab Pharmacokinet. 2014;29(5):400-406
13. Perloff MD, von Moltke LL, Cotreau MM, Greenblatt DJ. Unchanged cytochrome P450 3A (CYP3A) expression and metabolism of midazolam, triazolam, and dexamethasone in mdr (−/−) mouse liver microsomes. Biochem Pharmacol. 1999;57(11):1227-1232
14. Samuelsson K, Pickup K, Sarda S, Swales JG, Morikawa Y, Schulz-Utermoehl T, Hutchison M, Wilson ID. Pharmacokinetics and metabolism of midazolam in chimeric mice with humanised livers. Xenobiotica. 2012;42(11):1128-1137
15. Patki KC, von Moltke LL, Greenblatt DJ. In vitro metabolism of midazolam, triazolam, nifedipine, and testosterone by human liver microsomes and recombinant cytochromes p450: role of cyp3a4 and cyp3a5. Drug Metab Disposition. 2003;31(7):938-944
16. Bockermann R, Schubert D, Kamradt T, Holmdahl R. Induction of a B-cell-dependent chronic arthritis with glucose-6-phosphate isomerase. Arthrit Res Ther. 2005;7(6):R1316-R1324
17. Kamath S, Kummerow F, Narayan KA. A simple procedure for the isolation of rat liver microsomes. FEBS Lett. 1971;17(1):90-92
18. Elovaara E, Mikkola J, Luukkanen L, Antonio L, Fournel-Gigleux S, Burchell B, Magdalou J, Taskinen J. Assessment of catechol induction and glucuronidation in rat liver microsomes. Drug Metab Disposition. 2004;32(12):1426-1433
19. Smith PK, Krohn RI, Hermanson G, Mallia A, Gartner F, Provenzano M, Fujimoto E, Goeke N, Olson B, Klenk D. Measurement of protein using bicinchoninic acid. Anal Biochem. 1985;150(1):76-85
20. Granvil CP, Yu A-M, Elizondo G, Akiyama TE, Cheung C, Feigenbaum L, Krausz KW, Gonzalez FJ. Expression of the human CYP3A4 gene in the small intestine of transgenic mice: in vitro metabolism and pharmacokinetics of midazolam. Drug Metab Disposition. 2003;31(5):548-558
21. Kuze J, Mutoh T, Takenaka T, Morisaki K, Nakura H, Hanioka N, Narimatsu S. Separate evaluation of intestinal and hepatic metabolism of three benzodiazepines in rats with

cannulated portal and jugular veins: comparison with the profile in non-cannulated mice. Xenobiotica. 2009;39(11):871-880
22. Zhang W, Han F, Guo P, Zhao H, Lin ZJ, Huang M-Q, Bertelsen K, Weng N. Simultaneous determination of tolbutamide, omeprazole, midazolam and dextromethorphan in human plasma by LC–MS/MS—A high throughput approach to evaluate drug–drug interactions. J Chromatogr B. 2010;878(15):1169-1177
23. Davies B, Morris T. Physiological parameters in laboratory animals and humans. Pharm Res. 1993;10(7):1093-1095
24. Brown RP, Delp MD, Lindstedt SL, Rhomberg LR, Beliles RP. Physiological parameter values for physiologically based pharmacokinetic models. Toxicol Ind Health. 1997;13(4):407-484
25. Kirman C, Hays S, Aylward L, Suh M, Harris M, Thompson C, Haws L, Proctor D. Physiologically based pharmacokinetic model for rats and mice orally exposed to chromium. Chem-Biol Interact. 2012;200(1):45-64
26. Masyuk TV, Ritman EL, LaRusso NF. Hepatic artery and portal vein remodeling in rat liver: vascular response to selective cholangiocyte proliferation. Am J Pathol. 2003;162(4):1175-1182
27. Kuze J, Mutoh T, Takenaka T, Oda N, Hanioka N, Narimatsu S. Evaluation of animal models for intestinal first-pass metabolism of drug candidates to be metabolized by CYP3A enzymes via in vivo and in vitro oxidation of midazolam and triazolam. Xenobiotica. 2013;43(7):598-606
28. Barter ZE, Bayliss MK, Beaune PH, Boobis AR, Carlile DJ, Edwards RJ, Brian Houston J, Lake BG, Lipscomb JC, Pelkonen OR. Scaling factors for the extrapolation of in vivo metabolic drug clearance from in vitro data: reaching a consensus on values of human micro-somal protein and hepatocellularity per gram of liver. Curr Drug Metab. 2007;8(1):33-45
29. Cubitt HE, Houston JB, Galetin A. Prediction of human drug clearance by multiple metabolic pathways: integration of hepatic and intestinal microsomal and cytosolic data. Drug Metab Disposition. 2011;39(5):864-873
30. Zhang X, Quinney SK, Gorski JC, Jones DR, Hall SD. Semiphysiologically based pharmacokinetic models for the inhibition of midazolam clearance by diltiazem and its major metabolite. Drug Metab Disposition. 2009;37(8):1587-1597
31. Yang J, Jamei M, Yeo KR, Tucker GT, Rostami-Hodjegan A. Prediction of intestinal first-pass drug metabolism. Curr Drug Metab. 2007;8(7):676-684
32. Chowdhury F, Williams A, Johnson P. Validation and comparison of two multiplex technologies, Luminex® and Mesoscale Discovery, for human cytokine profiling. J Immunol Methods. 2009;340(1):55-64
33. Lu J, Goldsmith M-R, Grulke CM, Chang DT, Brooks RD, Leonard JA, Phillips MB, Hypes ED, Fair MJ, Tornero-Velez R. Developing a Physiologically-Based Pharmacokinetic Model Knowledgebase in Support of Provisional Model Construction. PLoS Comput Biol. 2016;12(2):e1004495
34. Cleton A, Mazee D, Voskuyl R, Danhof M. Rate of change of blood concentrations is a major determinant of the pharmacodynamics of midazolam in rats. Br J Pharmacol. 1999;127(1):227-235
35. Wang J, Xia S, Xue W, Wang D, Sai Y, Liu L, Liu X. A semi-physiologically-based pharmacokinetic model characterizing mechanism-based auto-inhibition to predict

stereoselective pharmacokinetics of verapamil and its metabolite norverapamil in human. Eur J Pharm Sci. 2013;50(3):290-302
36. Czerwiński M, Kazmi F, Parkinson A, Buckley DB. Anti-CD28 monoclonal antibody-stimulated cytokines released from blood suppress CYP1A2, CYP2B6 and CYP3A4 in human hepatocytes in vitro. Drug Metab Disposition. 2015;43(1):42-52
37. Dickmann LJ, Patel SK, Rock DA, Wienkers LC, Slatter JG. Effects of interleukin-6 (IL-6) and an anti-IL-6 monoclonal antibody on drug-metabolizing enzymes in human hepatocyte culture. Drug Metab Disposition. 2011;39(8):1415-1422
38. Machavaram K, Almond L, Rostami-Hodjegan A, Gardner I, Jamei M, Tay S, Wong S, Joshi A, Kenny J. A Physiologically Based Pharmacokinetic Modeling Approach to Predict Disease–Drug Interactions: Suppression of CYP3A by IL-6. Clin Pharmacol Ther. 2013;94(2):260-268
39. Charles P, Elliott MJ, Davis D, Potter A, Kalden JR, Antoni C, Breedveld FC, Smolen JS, Eberl G, Feldmann M. Regulation of cytokines, cytokine inhibitors, and acute-phase proteins following anti-TNF-α therapy in rheumatoid arthritis. J Immunol. 1999;163(3):1521-1528
40. Lee J-I, Zhang L, Men AY, Kenna LA, Huang S-M. CYP-mediated therapeutic protein-drug interactions. Clin Pharmacokinet. 2010;49(5):295-310
41. De Vries J, Rudi J, Walter-Sack I, Conradi R. The determination of total and unbound midazolam in human plasma. A comparison of high performance liquid chromatography, gas chromatography and gas chromatography/mass spectrometry. Biomed Chromatogr. 1990;4(1):28-33
42. Reed MD, Myers CM, Blumer JL. Influence of midazolam on the protein binding of ketorolac. Current therapeutic research. 2001;62(8):558-565
43. Higai K, Azuma Y, Aoki Y, Matsumoto K. Altered glycosylation of α 1-acid glycoprotein in patients with inflammation and diabetes mellitus. Clin Chim Acta. 2003;329(1):117-125
44. Piafsky KM, Borgå O, Odar-Cederlöf I, Johansson C, Sjöqvist F. Increased plasma protein binding of propranolol and chlorpromazine mediated by disease-induced elevations of plasma α1 acid glycoprotein. N Engl J Med. 1978;299(26):1435-1439
45. Heizmann P, Ziegler W. Excretion and metabolism of 14C-midazolam in humans following oral dosing. Arzneimittelforschung. 1981;31(12a):2220-2223
46. Woo GK, Williams T, Kolis S, Warinsky D, Sasso G, Schwartz M. Biotransformation of [14C] midazolam in the rat in vitro and in vivo. Xenobiotica. 1981;11(6):373-384
47. Thummel KE, O'shea D, Paine MF, Shen DD, Kunze KL, Perkins JD, Wilkinson GR. Oral first-pass elimination of midazolam involves both gastrointestinal and hepatic CYP3A-mediated metabolism. Clin Pharmacol Ther. 1996;59(5):491-502

Chapter 5 : Future Directions

The lymphatic trunk-LN clearance was estimated using the top-down minimal PBPK model (Chapter 2). The model indicates that the LNs are mainly responsible for proteolysis of mAbs. Therefore, LN cell suspension can be used in the future to measure the rate of mAb clearance. In addition, the *in vitro* methods representing the SC tissue should be developed to understand mechanism of mAb loss leading to their reduced bioavailability. The minimal PBPK model may be used as a platform to include the *in vitro* clearance data for prediction of SC PK.

The SC injection site lymph flow, afferent lymph flow, efferent lymph flow, volumes associated with the SC injection site, thoracic duct lymph flow were important physiological parameters governing the absorption of mAbs. However, further research is needed to understand the transit of mAbs via SC tissue and lymphatic system. For example, in this study, the lymphatic capillary network and lymphatic trunk volumes were approximately measured based on the literature information. However, the clinical data indicating the lymphatic distribution of mAbs after SC administration can help to modify the model volumes. In addition, the physiological parameters are variable across the population and can change due to physical stress. Therefore, detailed investigation about impact of the disease conditions, populations, species and exercise on various lymph flows and volumes is necessary. The top-down approach should also be used for other types of mAbs (e.g. IgG2, IgG4) and TPs (e.g. peptides, growth hormone, insulin). The model estimated lymphatic trunk-LN clearance increased with increase in the *pI* of the mAbs. Furthermore, the relationship of the estimated clearance and *pI* should be verified using other TPs.

In Chapter 3, effect of IONPs on degree of the oxidation and secondary structure of rGH was evaluated. The IONPs decreased H_2O_2- and AAPH-mediated oxidation. This could indicate that the rGH corona was possibly formed around the IONPs. Hence, rGH was protected against

the induced oxidation. However, this phenomenon should be verified using other combinations of TPs and metal nanoparticles. Furthermore, the α-helical structure of rGH was altered in the presence of IONPs. It should be investigated if the IONPs can change the secondary structure of other proteins having predominant β sheets, β turns or Ω loops.

In Chapter 4, the minimal PBPK model predicted PK of MDZ (a standard CYP substrate) during the GPI-mediated inflammation. However, the PK and *in vitro* metabolism of standard substrates of other CYPs must be evaluated. This would potentially help to predict PK in the disease state for NCEs metabolized by various CYPs. Furthermore, the cytokine measurements at various stages of the GPI-mediated inflammation may be correlated mathematically with the suppression of CYP mRNA and functional impact on the *in vitro* metabolism and PK. It is possible to predict the PK of NCEs (metabolized by the CYPs), based on the known suppression of the CYP mRNA, and elevation of serum cytokines during the disease.